Advanced Approaches to High Intensity Laser-Driven Ion Acceleration

Andreas Henig

München 2010

Advanced Approaches to High Intensity Laser-Driven Ion Acceleration

Andreas Henig

Dissertation
an der Fakultät für Physik
der Ludwig–Maximilians–Universität
München

vorgelegt von
Andreas Henig
aus Würzburg

München, den 18. März 2010

Erstgutachter: Prof. Dr. Dietrich Habs

Zweitgutachter: Prof. Dr. Toshiki Tajima

Tag der mündlichen Prüfung: 26. April 2010

Contents

List of Figures

Abstract

Since the pioneering work that was carried out 10 years ago [1–4], the generation of highly energetic ion beams from laser-plasma interactions has been investigated in much detail in the regime of target normal sheath acceleration (TNSA). Creation of ion beams with small longitudinal and transverse emittance and energies extending up to tens of MeV fueled visions of compact, laser-driven ion sources for applications such as ion beam therapy of tumors or fast ignition inertial confinement fusion. However, new pathways are of crucial importance to push the current limits of laser-generated ion beams further towards parameters necessary for those applications.

The presented PhD work was intended to develop and explore advanced approaches to high intensity laser-driven ion acceleration that reach beyond TNSA. In this spirit, ion acceleration from two novel target systems was investigated, namely mass-limited microspheres and nm-thin, free-standing diamond-like carbon (DLC) foils. Using such ultrathin foils, a new regime of ion acceleration was found where the laser transfers energy to all electrons located within the focal volume. While for TNSA the accelerating electric field is stationary and ion acceleration is spatially separated from laser absorption into electrons, now a localized longitudinal field enhancement is present that co-propagates with the ions as the accompanying laser pulse pushes the electrons forward. Unprecedented maximum ion energies were obtained, reaching beyond 0.5 GeV for carbon C^{6+} and thus exceeding previous TNSA results by about one order of magnitude. When changing the laser polarization to circular, electron heating and expansion were shown to be efficiently suppressed, resulting for the first time in a phase-stable acceleration that is dominated by the laser radiation pressure which led to the observation of a peaked C^{6+} spectrum. Compared to quasi-monoenergetic ion beam generation within the TNSA regime [5], a more than 40 times increase in conversion efficiency was achieved. The possibility to manipulate the shape of the ion acceleration front was successfully demonstrated by use of a spherically curved target surface. Finally, the last part of the presented work is devoted to accomplishments in laser development.

Zusammenfassung

Seit der vor zehn Jahren geleisteten Pionierarbeit [1–4] wurde die Beschleunigung hochenergetischer Ionenstrahlen in lasergetriebenen Plasmen intensiv im Target Normal Sheath Acceleration (TNSA) Regime untersucht. Die Erzeugung von Ionenstrahlen kleiner longitudinaler und transversaler Emittanz und Energien von bis zu einigen zehn MeV weckte die Vision einer kompakten, lasergetriebenen Ionenquelle für Anwendungen wie Ionenstahl-Krebstherapie oder die schnelle Zündung von Trägheitseinschluss-Fusion. Um lasergetriebene Ionenbeschleunigung für derartige Anwendungen nutzbar machen zu können sind allerdings neue Methoden von essentieller Bedeutung.

Die vorliegende Doktorarbeit hatte das Ziel solch fortgeschrittene Beschleunigungsprozesse zu entwickeln, welche über TNSA hinausgehen. Aus dieser Motivation heraus wurde Ionenbeschleunigung mittels neuartiger Targetsysteme untersucht. Bei Verwendung nm- statt μm-dünner Folien wurde ein neuer Beschleunigungsmechanismus beobachtet, in dem der Laser Energie auf alle Elektronen innerhalb des Fokusvolumens überträgt. Während im Fall von TNSA ein stationäres elektrisches Beschleunigungsfeld vorherrscht und die Ionenbeschleunigung räumlich getrennt von der Energieabgabe des Lasers an Elektronen stattfindet, bildet sich nun ein lokales Feldmaximum aus das sich mit den Ionen mitbewegt. Bisher unerreichte Ionenenergien von mehr als 0.5 GeV C^{6+} wurden so erzielt, was vorige TNSA Werte um eine Größenordung übertrifft. Es wurde gezeigt, dass das Aufheizen und die Expansion von Elektronen durch die Verwendung zirkularer statt linearer Laserpolarisation unterdrückt wird. Dadurch konnte erstmals eine lichtdruckdominierte, phasenstabile Beschleunigung experimentell nachgewiesen werden. Verglichen mit der Erzeugung quasi-monoenergetischer Strahlen innerhalb des TNSA-Regimes [5] wurde eine mehr als vierzigfach verbesserte Konversionseffizienz erreicht. Mittels der gekrümmten Oberfläche eines Mikrokugel-Targets wurde die Möglichkeit einer Formveränderung der Ionenbeschleunigungsfront demonstriert. Im letzten Teil der Arbeit werden schließlich in der Laserentwicklung erzielte Ergebnisse vorgestellt.

Chapter 1

Introduction

1.1 History and Previous Achievements

Starting with the first realization of the laser in 1960 [6], investigation of light-matter interactions has been a vivid field of research. Since then, major advances in laser technology allowed for studies at ever increasing intensities [7, 8]. With the technique of Q-switching [9], shortly followed by the development of mode-locking [10, 11], continuous wave (cw) operation was superseded by the possibility to store the laser energy in short pulses, ranging in duration from nanoseconds down to tens of femtoseconds with present-day large bandwidth gain materials. In terms of focussed laser intensity, an upper limit seemed to be reached in the 1970s at values around $10^{15}\,\mathrm{W/cm^2}$, imposed by the damage threshold of optics and gain material in the amplification stages, leading to enormously large systems with huge beam diameters of up to 50 cm that were restricted to National Lab facilities. This quandary was finally overcome in 1985 with the invention of chirped pulse amplification (CPA) by Strickland and Mourou [12]. By stretching the pulse temporally instead of spatially prior to amplification, the construction of compact Terawatt to Petawatt class laser systems became possible, allowing for studies of laser-matter interactions at extreme intensities of up to $10^{22}\,\mathrm{W/cm^2}$ at present [13].

Among the prime interests in this field ranks the acceleration of particles from plasmas driven by highly intense laser pulses. While the design of conventional accelerators is limited by the breakdown voltage of the accelerating structure ($\sim 100\,\mathrm{MVm^{-1}}$), plasmas do not suffer from this constraint. In 1979, Tajima and Dawson first proposed to use relativistic plasma waves formed in the wake of a laser to accelerate electrons to high energies [14]. Based on this approach, quasi-monoenergetic electron bunches of energy as high as $\sim 1\,\mathrm{GeV}$ have been demonstrated experimen-

tally [15], being accelerated over a distance as short as 3.3 cm.

Whereas electrons are directly driven to relativistic oscillations in the laser field already at intensities beyond $10^{18}\,\mathrm{W/cm^2}$ for common wavelengths of around 1 μm, the corresponding intensity for directly driven relativistic proton dynamics amounts to $5 \times 10^{24}\,\mathrm{W/cm^2}$, by far exceeding the achievable peak intensity of presently available laser facilities. Thus, electromagnetic field energy is not directly transfered to ions but electrons act as a mediator instead, absorbing energy from the laser and setting up charge separation fields which in turn accelerate ions.

Over the course of the past 10-15 years, the most intensively investigated experimental concept for high intensity laser-driven ion acceleration has been target normal sheath acceleration (TNSA) [1–4, 16]. In the vast majority of such previous studies, solid density foil targets ranging in thickness from a few to several tens of microns have been irradiated by linearly polarized, intense ($10^{18} - 10^{21}\,\mathrm{W/cm^2}$) laser pulses. Here, the laser generates hot electrons in a blow-off plasma at the target front. Those energetic electrons traverse the opaque foil to set up a quasi-static field of order TV/m at the non-irradiated side of the target. Atoms located in the substrate and in surface layers, which are formed by contaminations of hydrocarbons and H_2O, become ionized and subsequently accelerated. It is evident, that particles with high charge-to-mass (q/m) ratio, i.e. protons, will favorably gain energy from the sheath field, which results in a considerable reduction in acceleration for other ion species. An actual image of the laser-plasma interaction captured during a typical ion acceleration experiment is depicted in figure 1.1.

By virtue of the TNSA mechanism, proton beams exhibiting a continuous, exponentially decaying spectrum of energies up to 58 MeV have been obtained employing a picosecond petawatt laser at intensities of $\sim 3 \times 10^{20}\,\mathrm{W/cm^2}$ [3]. To demonstrate the high quality of the beam, the transverse and longitudinal emittance of laser-accelerated protons above 10 MeV was characterized to < 0.004 mm mrad and $< 10^{-4}$ eV s respectively, hence being superior to conventional accelerators by around two order of magnitude [17]. In order to efficiently accelerate heavier ions by employing TNSA, hydrogen contaminants need to be removed from the target [5, 18, 19]. It has been shown, that this is most effectively done by resistive heating, yielding medium-mass ion cut-off energies of ~ 3.5 MeV/u for carbon C^{5+} [5] and 5 MeV/u for fluorine F^{7+} [18]. In addition, the transition from a continuous to a quasi-monochromatic ion energy distribution has been demonstrated within the TNSA-regime by restricting the ion source to a small volume where the sheath field is homogenous [5, 20, 21].

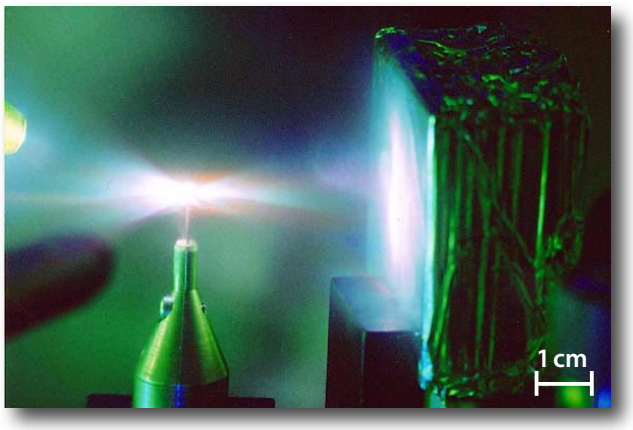

Fig. 1.1. *Time-integrated CCD camera image of the laser-plasma interaction, captured during a typical experiment aiming for laser-driven acceleration of ions. In this case, the TRIDENT laser was focussed from the left onto a micrometer-thick copper foil. The forward accelerated proton beam was detected by a stack of radiochromic film (RCF) layers wrapped in aluminum, that is visible in the right half of the picture. Green background light originates from second harmonic generation. The image gives an impression of the compactness of the ion acceleration setup.*

1.2 Envisioned Applications

Laser-accelerated ion beams are considered for a wide range of applications. A prominent implementation that is exploiting the unique properties of a laser-generated source is proton radiography, where the beam is used as a diagnostic tool for electromagnetic fields. Owing to the small effective source size of only a few microns and the short bunch duration which is comparable to the laser pulse width ($\leq 1\,\mathrm{ps}$), a very high spatial and temporal resolution can be achieved [22–24]. The process also takes advantage of the "chirped" nature of the broad spectral distribution of proton energies as the fastest protons that move ahead of the bunch capture an image at an earlier time than the lower energetic, trailing protons. Thus, a time-resolved series of images can be obtained. Various ultrafast phenomena in laser plasma interactions have been investigated, such as the sheath fields responsible for ion acceleration within the TNSA regime [25] or the evolution of plasma channels in the wake of a highly intense laser pulse [26].

Another application that is currently attracting high interest is related to health care, namely ion beam therapy (IBT) of tumors. At the moment, radiation therapy still almost exclusively relies on electron beams or X-rays which are unfavorable for deeply situated tumors surrounded by healthy tissue due to the broad depth-dose distribution. Owing to the fact that ions deposit the vast majority of their energy shortly before being stopped in which is referred to as the Bragg peak, the necessary

dose for killing cancer cells can be applied much more localized. Motivated by those superior treatment prospects, conventional ion accelerators based on synchrotrons have been implemented into hospitals recently. However, given the huge size of those machines, only a handful of clinics can afford the enormous costs. To state an example, the just completed Heidelberg Ion Therapy Facility (HIT) [27, 28] that is capable of producing up to 221 MeV protons and 430 MeV/u carbon ions was worth 119 Million Euro, featuring a three stories high, 600 tons, rotating gantry for beam steering around the patient. Hence, in order to make ion beam therapy available to the broad public, the size and costs of the accelerator including beam transport has to be reduced significantly. A promising candidate to achieve this goal are laser-driven ion sources [29], owing to the drastically increased accelerating fields in plasmas and therefore much reduced acceleration distances of only micrometers. Figure 1.1 gives an impression of the compactness of the setup. Nevertheless, parameters such as ion energy, spectral distribution, repetition rate and reliability need to be significantly improved on to be able to compete with conventional accelerators in the field of IBT.

Finally, a third application that should be mentioned here is the potential use of a laser-generated ion bunch as fast ignitor in inertial confinement fusion (ICF). For fusion reactions to occur, the fuel needs to be heated to high temperatures, in case of a mixture of deuterium and tritium (DT) to values around 10 keV. Furthermore, the hot fuel has to be contained for a long enough time to attain a sizable number of fusion reactions. To meet these conditions, two different approaches are being followed. In magnetic confinement fusion (MCF) a comparably low density plasma ($n_e \sim 10^{15}\,\mathrm{cm}^{-3}$) is confined by magnetic fields, e. g. in a tokamak such as ITER [30], for a rather long time ($t \sim 1\,s$). In ICF, the necessary confinement time is reduced to a few nanoseconds by compressing the fuel to high densities ($n_e \sim 10^{26}\,\mathrm{cm}^{-3}$). Compression is achieved either by focussing a multitude of laser pulses simultaneously onto the surface of a spherical DT pellet or indirectly via generation of soft X-rays in a hohlraum to drive the implosion. Based on this approach, the worlds largest and highest-energy laser, the National Ignition Facility (NIF) [31] located at Lawrence Livermore Laboratory in the US incorporating 192 synchronized beams of a total energy of 1.8 MJ in the ultraviolet, aims to start ICF experiments this summer. The generated ablation pressure has to be highly symmetric to avoid hydrodynamic instabilities and ensure a sufficient temperature and density in the central hotspot for ignition of the compressed fuel.

To ease this demanding requirement, Tabak *et al.* [32] proposed to separate the phases of compression and heating by compressing the fuel at low temperature

and employing a particle beam to heat and ignite the fuel at the moment of maximum compression. So far, electron beams were mostly considered to be used for fast ignition, being guided to the plasma core by a cone added to the fuel capsule [33]. However, owing to their favorable depth-dose distribution as discussed above, ions are advantageous when compared to electrons in order to locally deposit large amounts of energy. Thus, laser-accelerated, dense ion beams are attracting increasing attention as a highly promising fast ignitor candidate [34–37]. For use in ICF, one aspires a laser-acceleration scheme to produce a quasi-monoenergetic ion bunch ($\Delta E/E$ below $\sim$ 10%) at moderate energies ($E \sim 450\,\mathrm{MeV}$ for carbon ions) but very high laser-to-ion conversion efficiencies ($\sim$ 10%) to achieve the required power density ($\sim 10\,\mathrm{kJ}/10\,\mathrm{ps}$ in a $20\,\mu\mathrm{m}$ diameter spot) to ignite the compressed DT fuel. Hence, previously employed schemes for the generation of quasi-monoenergetic ion beams within the TNSA regime [5, 20] are clearly inadequate for this purpose due to the naturally very limited conversion efficiency attainable.

1.3 Thesis Outline

The presented PhD work was intended to develop and explore advanced approaches to high intensity laser-driven ion acceleration that reach beyond the previously studied regime of TNSA. Clearly, such new pathways are of crucial importance to push the current limits of laser-generated ion beams further towards parameters necessary for potential applications. In this spirit, ion acceleration from two novel target systems was investigated, namely mass-limited microspheres and nm-thin, free-standing diamond-like carbon (DLC) foils. The described studies were carried out during a series of experimental campaigns at a variety of different high intensity laser systems worldwide, from ATLAS (MPQ) over MBI Berlin and VULCAN (RAL, UK) to TRIDENT (LANL, USA), allowing to scan a broad range of laser parameters. In addition to advancing the process of ion acceleration itself, evolution of high intensity laser technology is essential to eventually enable the construction of a laser-driven accelerator facility. Thus, a part of the presented work is devoted to accomplishments in laser development.

The thesis is structured as follows:

Chapter 2 introduces the theoretical foundations of high intensity laser interaction with matter, from ionization over relativistic single electron dynamics and laser propagation and absorption in plasmas to the main concepts of laser-driven ion acceleration.

Chapter 3 describes the fundamentals of ultrashort high intensity pulse generation in general and gives details on the different laser systems utilized to investigate the acceleration of ions.

Chapter 4 presents targets and ion beam diagnostics. In particular, the methods utilized to fabricate and characterize the indispensable novel microsphere and DLC targets employed for ion acceleration studies are illustrated. Additionally, ion detectors and measuring instruments that were used to characterize the accelerated ion beams are specified.

Chapter 5 reports on the first-time experimental observation of strongly directed proton beams emitted from spherical mass-limited targets of diameter 15 μm. The experiments were carried out at the ATLAS 20-TW Ti:Sapphire laser system located at MPQ. When irradiated with an 45 fs short, highly intense (1×10^{20} W/cm^2) laser pulse, a converging shock front forms at the front side of the target. Protons accelerated in this shock reach energies well in excess of the values observed in the TNSA regime under identical laser conditions, showing a plateau-shaped spectrum as predicted by Silva *et al.* [38]. Three-dimensional particle-in-cell (PIC) simulations with over-dense proton plasmas were conducted, supporting the experimental observations. The hole-boring radiation pressure model for ion acceleration [39] was extended to a radially dependent intensity profile and successfully implemented to reproduce the shape of the shock front obtained from PIC simulations. Obtained results are published in [Henig *et al.*, Phys. Rev. Lett **102**, 095002 (2009)] [40].

Chapter 6 reports on the first and second experimental campaign investigating ion acceleration from ultra-thin DLC foils. In the leadoff study, targets of thickness 50, 30 and 10 nm were irradiated by 700 fs long, ultra-high contrast laser pulses at intensities of $\sim 7 \times 10^{19}$ W/cm^2 employing the TRIDENT laser facility located at Los Alamos National Laboratory, USA. An unprecedented maximum energy of 185 MeV (15 MeV/u) for fully ionized carbon atoms was observed at the optimum thickness of 30 nm. In contrast to TNSA where the target remains opaque throughout the interaction, the enhanced acceleration is attributed to self-induced transparency when the instantaneous laser intensity is at maximum. At that moment strong volumetric energy transfer to the classically overdense electron population in the bulk of the target takes place, giving rise to a large longitudinal field that is localized and co-propagates with the ions. It is demonstrated for the first time experimentally that a distinct optimum foil thickness exists even for a high-contrast laser pulse, where the lower limit is imposed by premature burn-through of the target already on the rising edge of the pulse. The experimental results are supported by PIC simulations. In addition, a simple analytical model was developed to predict the optimum

thickness for given laser parameters, demonstrating the direct connection between the instantaneous laser intensity at the time when the target becomes relativistically transparent and the resulting maximum ion energies. Obtained findings are published in [Henig *et al.*, Phys. Rev. Lett **103**, 045002 (2009)] [41]. In a follow-up campaign, the TRIDENT peak intensity was increased to $2 \times 10^{20}\,\mathrm{W/cm^2}$, resulting in a shift of the optimum foil thickness to larger values as expected by the model. For a target thickness of 58 nm, carbon C^{6+} ions of energy beyond 0.5 GeV were observed, representing the current world record obtained from a laser-driven accelerator.

Chapter 7 reports on experimental studies on ion acceleration from ultra-thin DLC foils irradiated by much shorter ultra-high contrast laser pulses of only 45 fs FWHM duration at lower energies of only 0.7 J that were focussed to comparable peak intensities of $5 \times 10^{19}\,\mathrm{W/cm^2}$. The experiments were carried out at the 30-TW Ti:Sapphire laser system located at MBI, Berlin. Owing to the decreased pulse duration, target expansion and heating on the rising edge of the pulse is strongly reduced, yielding an optimum foil thickness as low as 5.3 nm. When changing the laser polarization from linear to circular a strong decrease in the number of hot electrons is observed, resulting in a pronounced peak centered at 30 MeV in the carbon C^{6+} ion spectrum at the optimum foil thickness. Compared to quasi-monoenergetic ion beam generation within the TNSA regime [5], a more than 40 times increase in conversion efficiency is demonstrated when considering an identical energy spread around the apex. 2D PIC simulations have been carried out, giving clear evidence that those ions are for the first time dominantly accelerated in a phase-stable way by the laser radiation pressure at values up to $\sim 10^{21}\,\mathrm{m/s^2}$. While linear polarization gives rise to the generation of a large number of highly energetic electrons, causing the target plasma to expand rapidly, in case of circular polarization electrons and ions co-propagate as a dense, quasi-neutral plasma bunch over the whole duration of the laser pulse. The acceleration of ions is thus no longer dominated by the sheath field of an expanding electron cloud. An illustration of the laser field pushing the ultra-thin plasma layer like a light sail in forward direction is depicted in figure 1.2. Being recently widely studied in theory, these comparative measurements provide the first experimental proof of the feasibility of radiation pressure acceleration to become the dominant mechanism for ion acceleration when circular polarization is used. Obtained results are published in [Henig *et al.*, Phys. Rev. Lett **103**, 245003 (2009)] [42].

Chapter 8 presents advances on short pulse pumped ultrabroadband non-collinear optical parametric chirped-pulse amplification (SPP-OPCPA) that have been ac-

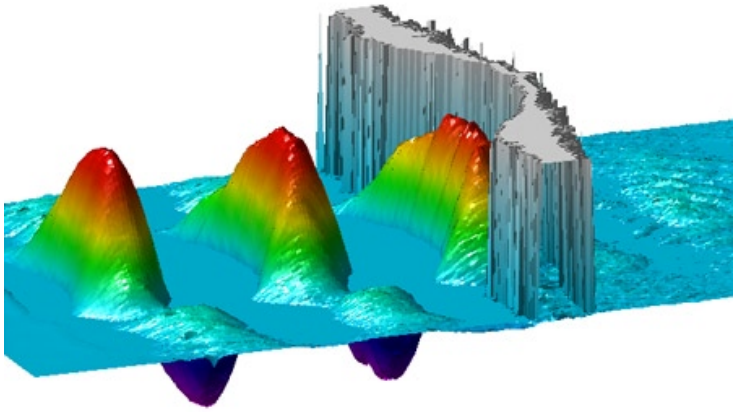

Fig. 1.2. *Illustration of radiation pressure acceleration. Shown is the transverse electric field component E_y of a circularly polarized laser pulse incident onto an initially 5 nm thin, solid density plasma layer marked in grey color. Like a light sail, the overdense plasma layer is pushed in forward direction by the radiation pressure of the intense laser pulse. The image is based on data extracted from 2D PIC simulations that were carried out by X. Q. Yan, refer to chapter 7 for further details.*

complished as part of my PhD work [43]. Those findings represent an important step towards future next generation laser systems like the Petawatt Field Synthesizer (PFS) project that is currently being pursued by our group at MPQ [44], aiming for an energy of 5 J stored in pulses as short as 5 fs.

Chapter 9 summarizes the obtained findings and draws conclusions. An outlook towards future experimental prospects is given, building onto the results of this thesis.

Chapter 2

Theoretical Background

This chapter is intended to give a brief introduction to some of the fundamentals of high intensity short pulse laser interactions with matter and present basic concepts of laser-driven ion acceleration. More details on these topics can be found in the existing literature, e.g. in the books written by W. L. Kruer [45] and P. Gibbon [46].

2.1 Ionization

The physics behind laser-driven ion acceleration primarily deals with the behavior of ionized material, i.e., plasma, under intense irradiation, whereas the question regarding how the target material transforms into this state is typically of minor concern. Nevertheless, in order to give a feel for the dominant ionization processes taking place in the early stages of the interaction, a short description of this subject-matter will be given in the following.

First insight can be gained by comparison with quantities related to the hydrogen atom. From the Bohr model, the electron's Bohr radius amounts to

$$a_B = \frac{4\pi\epsilon_0\hbar^2}{m_e e^2} \simeq 5.3 \times 10^{-11}\,\mathrm{m}, \tag{2.1}$$

with reduced Planck's constant $\hbar$, permittivity of free space ϵ_0, and m_e and e being the electron mass and charge, respectively. Accordingly, the electric field strength in the coulombic potential is given by

$$E_a = \frac{e}{4\pi\epsilon_0 a_B^2} \simeq 5.1 \times 10^{9}\,\mathrm{Vm}^{-1}, \tag{2.2}$$

The corresponding intensity at which the laser field equals the binding strength of

the electron to the nucleus is referred to as the *atomic intensity* and is calculated to

$$I_a = \frac{\epsilon_0 c E_a^2}{2} \simeq 3.51 \times 10^{16}\,\mathrm{Wcm}^{-2} \tag{2.3}$$

Clearly, the laser field at intensities of $I_L = 10^{19}\,\mathrm{W/cm}^2$ and above as used in the particle acceleration experiments described within the framework of this thesis exceeds the interatomic fields by many orders of magnitude, thus easily guaranteeing ionization of any target material. However, even intensities well below this threshold are sufficient for ionization to occur e.g. via multiphoton effects.

Multiphoton Ionization

In case the energy of a single photon is smaller than the ionization potential of the bound state, an electron can still gain enough energy to overcome the potential barrier of the nucleus by absorbing several lower frequency photons on a short timescale in a process named *multiphoton ionization*. The probability of this mechanism can be found by expanding the theory of one photon dipole transitions to higher orders according to perturbation theory, with the n-photon ionization rate given by

$$W_n = \sigma_n I_L^n\,. \tag{2.4}$$

The cross-section σ_n decreases with n and the process strongly depends on the photon density of the laser field, setting in at intensities around $> 10^{10}\,\mathrm{W/cm}^2$.

Above-threshold ionization is an extension of multiphoton-ionization, where an electron is excited by more photons than strictly necessary to free it from the atom. Owing to the excess energy absorbed, the released electron will have higher kinetic energy, manifesting in distinct peaks separated by the photon energy $\hbar\omega$ in the electron spectrum.

Tunneling Ionization

When the intensity is further increased, the laser field is strong enough to significantly distort the atomic potential. A perturbation treatment as in the case of multiphoton ionization is therefore not valid anymore. Figure 2.1(b) illustrates how the large external field of a laser polarized in x-direction manipulates the former purely coulombic potential of figure 2.1(a).

At a certain distance on the right hand side of the atom, the Coulomb barrier is lowered beneath the binding energy of the electron. Thus, quantum mechani-

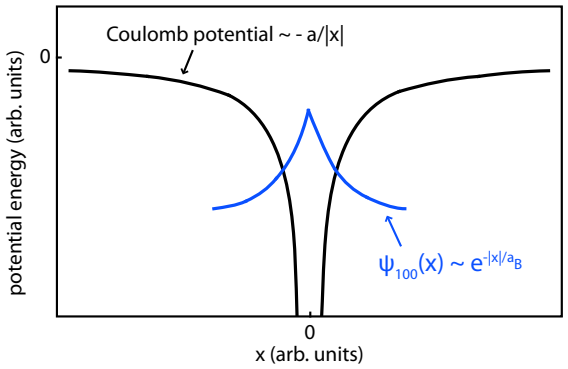

(a) Bound electron state (marked blue) in absence of an external field

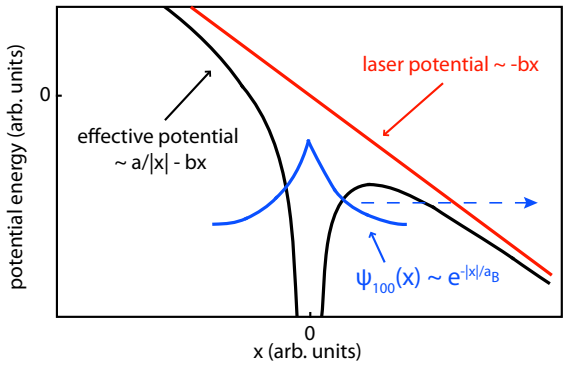

(b) Distortion of the atomic potential by a strong laser field (highlighted red), enabling tunnel ionization

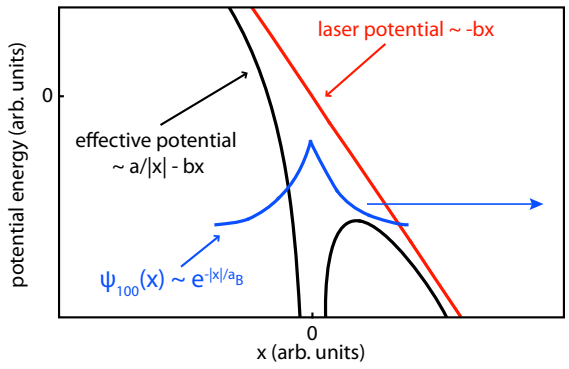

(c) Complete barrier suppression in an even higher field is greatly increasing the ionization rate

Fig. 2.1. *Shown is the distortion of the atomic potential of hydrogen subject to a strong laser field polarized in x-direction (a and b represent constants). Without the presence of an external field the potential is purely coulombic and the electron, allegorized by its ground state eigenfunction ψ_{100} with Bohr radius a_B, is bound. A strong field is lowering the potential barrier on one side so that the electron is enabled to tunnel through. At even higher fields the barrier gets suppressed below the ionization potential, allowing the electron to easily escape from the nucleus.*

cally the previously bound state is enabled to tunnel through this barrier with some finite probability, a scenario which is referred to as *tunneling ionization*. The corresponding ionization rate for hydrogen-like ions was derived by Keldysh [47], while Ammosov, Delone and Kraĭnov deduced the so-called ADK-rate for tunneling ionization in complex many-electron atoms or ions [48]. Recently, tunneling ionization was also observed experimentally in real time [49].

The Keldysh Parameter

In order to determine the dominant ionization mechanism prevailing for certain experimental conditions, the *Keldysh parameter* γ_K was introduced, separating the multiphoton and tunneling regimes

$$\gamma_K = \sqrt{\frac{V_{ion}}{2U_p}} \tag{2.5}$$

with V_{ion} being the ionization potential of the electronic state and U_p the *ponderomotive potential* of the laser, i.e., the cycle-averaged kinetic energy of a free electron oscillating in a linearly polarized electromagnetic field, given by

$$U_p = \frac{e^2 E_L^2}{4 m_e \omega_L^2} \propto I_L \lambda_L^2 \tag{2.6}$$

The ponderomotive potential is proportional to the product of the laser intensity I_L and the square of its wavelength λ_L. For more details on the motion of a single free electron subject to an intense laser field, refer to section 2.2.

From above equations it follows as a rule of thumb that tunneling becomes significant for high intensities and long wavelength, i.e., for $\gamma_K < 1$, while for $\gamma_K > 1$ multiphoton ionization is the relevant scenario. In case of hydrogen with $V_{ion,H} = 13.6\,\mathrm{eV}$ and a laser wavelength λ_L of one micron, the corresponding laser intensity at the transition point $\gamma_K = 1$ calculates to $I_{L,\gamma_K=1} \simeq 7.3 \times 10^{13}\,\mathrm{W/cm^2}$.

Barrier Suppression Ionization

At even higher intensities, the potential barrier is eventually suppressed below the ionization potential of the electronic state. The electron can hence easily escape from the nucleus, naturally resulting in a sizable increase in the ionization rate. This situation is known as over-the-barrier or *barrier suppression ionization* and is schematically depicted in figure 2.1(c).

For a more quantitative understanding, the appearance intensity of barrier suppression ionization can be obtained starting from the effective potential of an atom with atomic number Z situated in a linearly (in x-direction) polarized external field E_{ext}

$$V(x) = -\frac{Ze^2}{4\pi\epsilon_0|x|} - eE_{ext}x \tag{2.7}$$

By solving dV(x)/dx = 0 a local maximum of $V(x)$ is found, corresponding to a position x_{max} of

$$x_{max} = \sqrt{\frac{Ze}{4\pi\epsilon_0 E_{ext}}} \tag{2.8}$$

Equating the effective potential at $x = x_{max}$ with the ionization potential V_{ion} yields the electric field E_{BS} required to enable barrier suppression ionization

$$E_{BS} = \frac{V_{ion}^2 \pi\epsilon_0}{Ze^3} \tag{2.9}$$

The associated laser intensity amounts to

$$\begin{aligned} I_{BS} &= \frac{c\epsilon_0}{2}|E_{BS}|^2 \\ &= \frac{c\pi^2\epsilon_0^3 V_{ion}^4}{2Z^2e^6} \end{aligned} \tag{2.10}$$

Note that V_{ion} refers to the ionization potential of the atom or ion with charge $(Z-1)$.

To again give a numerical example, for hydrogen the minimum laser intensity necessary for barrier suppression ionization calculates to $I_{BS,H} \simeq 1.4 \times 10^{14}\,\mathrm{W/cm^2}$. Clearly, strong ionization sets in even at electric field values well below the previously deduced binding strength of the electron to the nucleus and the corresponding atomic intensity of $I_a \simeq 3.51 \times 10^{16}\,\mathrm{W/cm^2}$. In consequence, in the presented experimental studies the irradiated target material is transformed into plasma already on the very early rising edge of the pulse, long before the peak intensity of $> 10^{19}\,\mathrm{W/cm^2}$ is reached.

Collisional Ionization

While in above scenarios ionization of a single atom subject to a strong laser field is examined, additional mechanisms come into play when considering ionization of

solid density targets as employed for ion acceleration experiments. Once a sufficient number of free electrons is produced via field ionization, *collisional ionization* processes gain significance. In case of a local thermal equilibrium where the radiative and absorptive events are balanced, the ionization state can be determined by statistical means and the relative ion populations are related by the Saha-Boltzmann equation (see e.g. [50]). However, for short pulse laser-generated plasmas a more realistic view involves large density and temperature gradients as well as radiation that can escape the plasma completely. Here, the assumption of local thermal equilibrium is not valid anymore and time-dependent atomic rate equations typically need to be solved in order to determine the charge distribution [51].

2.2 Relativistic Single Electron Dynamics

Subsequent to ionization, an electron will undergo relativistic dynamics in the intense laser field. In the simplest case, a single electron subject to a plane electromagnetic wave is considered, that can be described in terms of its vector potential

$$\mathbf{A}(\mathbf{r},t) = \mathrm{Re}\left\{\mathbf{A_0}\mathrm{e}^{\mathrm{i}\psi}\right\}, \tag{2.11}$$

where $\mathbf{r}$ and t represent space and time coordinate, $\psi = \mathbf{k_L}\cdot\mathbf{r} - \omega_L t$ denotes the phase, $\mathbf{k_L}$ stands for the wavenumber $k_L = 2\pi/\lambda_L$ and ω_L for the laser frequency. With z being the propagation direction, the laser amplitude $\mathbf{A_0}$ is given by $\mathbf{A_0} = A_0\hat{e}_x$ for linear polarization (LP) and $\mathbf{A_0} = A_0(\hat{e}_x \pm i\hat{e}_y)$ for circular polarization (CP).

The electric and magnetic field is then obtained from

$$\mathbf{E} = -\frac{\partial \mathbf{A}}{\partial t} \tag{2.12}$$

$$\mathbf{B} = \nabla \times \mathbf{A} \tag{2.13}$$

It is often convenient to use the dimensionless laser vector potential, which is defined as follows

$$a = \frac{eA}{m_e c} \tag{2.14}$$

With the intensity of the laser being given by the magnitude of the Pointing vector $I = |\mathbf{S}| = \mu_0^{-1}|\mathbf{E}\times\mathbf{B}|$, the peak intensity I_0 can be written in terms of the peak

dimensionless laser amplitude a_0

$$I_0\,\lambda^2 = \zeta\left[1.37\times10^{18}\frac{\mathrm{W}}{\mathrm{cm}^2}\,\mu\mathrm{m}^2\right]\,a_0^2, \tag{2.15}$$

where $\zeta = 1$ for linear and $\zeta = 2$ for circular polarization.

The equation of motion for a single electron can now be derived starting from the Lorentz force

$$\frac{d\mathbf{p}}{dt} = -e\,(\mathbf{E} + \mathbf{v}\times\mathbf{B}) \tag{2.16}$$

with $\mathbf{v}$ and $\mathbf{p} = \gamma m_e\mathbf{v}$ being the electron velocity and momentum, respectively, and relativistic Lorentz factor $\gamma = 1/\sqrt{1-v^2/c^2} = \sqrt{1+p^2/m_e^2c^2}$, leading to the momentum relations [52]

$$\frac{p_x}{m_ec} = \frac{\gamma}{c}\frac{dx}{dt} = a_x \tag{2.17}$$

$$\frac{p_y}{m_ec} = \frac{\gamma}{c}\frac{dy}{dt} = a_y \tag{2.18}$$

$$\frac{p_z}{m_ec} = \frac{\gamma}{c}\frac{dz}{dt} = \frac{a^2}{2} \tag{2.19}$$

with $\gamma = 1 + a^2/2$. Integration of above equations for a given laser pulse $\mathbf{a}(t - z/c)$ is straightforward when rewritten in the variable $\tau = t - z(t)/c$, for which

$$\gamma\frac{d}{dt} = \gamma\frac{d\tau}{dt}\frac{d}{d\tau} = \gamma\left(1-\frac{1}{c}\frac{dz}{dt}\right)\frac{d}{d\tau} = \left(1+\frac{a^2}{2}-\frac{a^2}{2}\right)\frac{d}{d\tau} = \frac{d}{d\tau} \tag{2.20}$$

resulting in

$$\frac{dx}{d\tau} = ca_x \tag{2.21}$$

$$\frac{dy}{d\tau} = ca_y \tag{2.22}$$

$$\frac{dz}{d\tau} = \frac{ca^2}{2} \tag{2.23}$$

2.2.1 Relativistic Electron Trajectory in a Linearly Polarized Plane Wave

Considering a linearly polarized plane wave of infinite duration with $\mathbf{a} = a_0\cos(\omega_L\tau)\hat{e_x}$ acting on an electron initially at rest and located at $x = y = z = 0$, its trajectory is

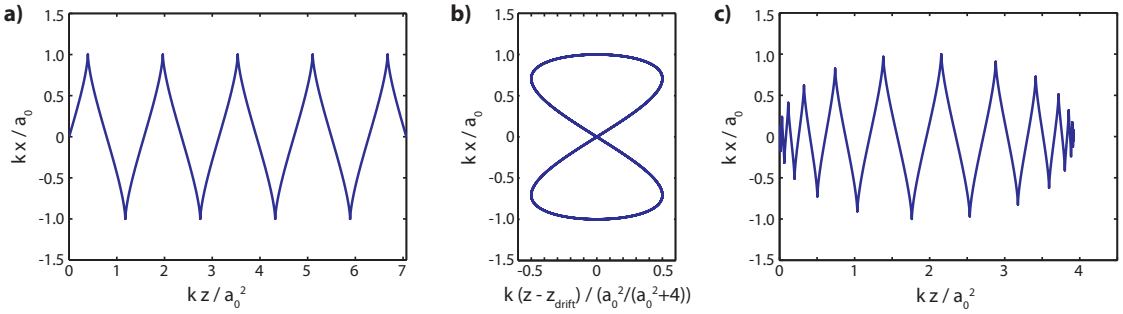

Fig. 2.2. *Trajectory of a single relativistic electron in a linearly polarized plane electromagnetic wave propagating in z-direction. Given that the laser amplitude a_0 is time-independent, the motion is shown in the laboratory frame (a) and in the average drift frame (b), while (c) illustrates the trajectory for a non-constant envelope in time ($a_0(\tau) = a_0 \exp(-(\tau/\tau_0)^2)$ with $\omega_L \tau_0 = 25$). Clearly, no net energy is transfered to the electron as it comes back to rest as soon as a_0 falls back to zero and is hence only shifted along the z-axis.*

described by

$$x(\tau) = ca_0 \int_0^\tau \cos(\omega_L \tilde{\tau}) d\tilde{\tau} = \frac{ca_0}{\omega_L} \sin(\omega_L \tau) \tag{2.24}$$

$$z(\tau) = \frac{ca_0^2}{2} \int_0^\tau \cos^2(\omega_L \tilde{\tau}) d\tilde{\tau} = \frac{ca_0^2}{4} \left(\tau + \frac{1}{2\omega_L} \sin(2\omega_L \tau) \right) \tag{2.25}$$

The corresponding self-similar electron trajectory is illustrated in figure 2.2a. Apparently, the particle is oscillating transversely at the laser frequency ω with amplitude proportional to the laser amplitude a_0, while the longitudinal oscillation occurs at twice the fundamental frequency and scales with a_0^2. In the highly relativistic case of $a_0 \gg 1$ the electron motion will therefore be predominantly along the longitudinal direction, owing to the strong magnetic $\mathbf{v} \times \mathbf{B}$ force turning the electron orbit.

Besides the oscillatory components, the electron undergoes an overall drift in forward direction with average drift velocity

$$\left\langle \frac{dz}{dt} \right\rangle = \left\langle \frac{a^2 c}{2\gamma} \right\rangle = \left\langle \frac{a^2 c}{a^2 + 2} \right\rangle = \frac{a_0^2 c}{a_0^2 + 4} \tag{2.26}$$

In the average rest frame, the electron trajectory shows the well known figure-8 shape as depicted in figure 2.2b.

Figure 2.2c again displays the case of a linearly polarized plane wave, but with Gaussian pulse envelope in time instead of infinite duration as before. Clearly, the electron comes back to rest after the laser pulse is over as it cannot gain net energy in a plane light wave. In order to transfer net energy, breaking of planar symmetry

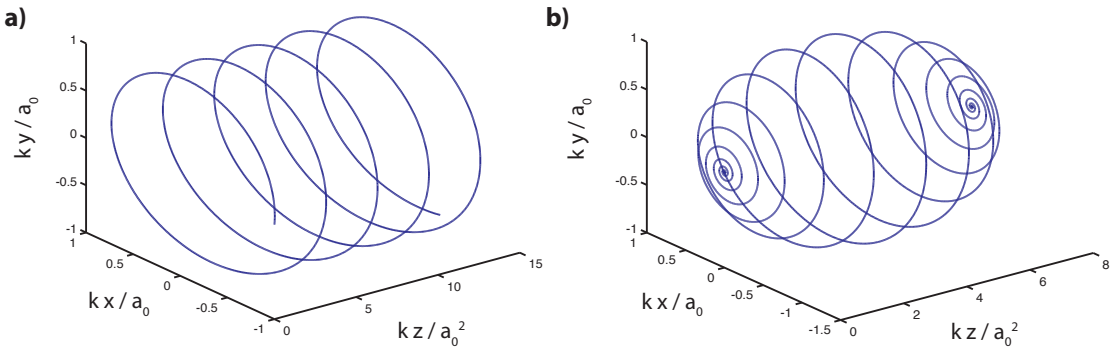

Fig. 2.3. *Trajectory of a single relativistic electron in a circularly polarized plane electromagnetic wave propagating in z-direction. Given that the laser amplitude a_0 is time-independent, the resulting helical orbit is shown in (a). As opposed to the case of linearly polarized irradiation, for circular polarization the longitudinal motion does not exhibit an oscillatory component. The trajectory for a non-constant but time-varying pulse envelope ($a_0(\tau) = a_0 \exp(-(\tau/\tau_0)^2)$ with $\omega_L \tau_0 = 25$) is illustrated in (b), the electron comes back to rest again after the finite pulse has passed.*

is needed, e.g. due to a finite beam radius such as in a tight laser focus.

2.2.2 Relativistic Electron Trajectory in a Circularly Polarized Plane Wave

For a circularly polarized plane wave of infinite duration, the trajectory is derived particularly easy as $a^2 = a_x^2 + a_y^2 = a_0^2$ and $\gamma = 1 + a_0^2/2$ are not time-dependent and one immediately obtains

$$x(\tau) = \frac{ca_0}{\omega_L} \sin(\omega_L \tau) \tag{2.27}$$

$$y(\tau) = \mp \frac{ca_0}{\omega_L} \cos(\omega_L \tau) \tag{2.28}$$

$$z(\tau) = \frac{ca_0^2}{2} \tau \tag{2.29}$$

with $\tau = t/\gamma$. Most significantly for the discussion in the following chapters is the fact that the longitudinal motion $z(\tau)$ does not exhibit an oscillatory component in case of circular polarization. The trajectory as it appears in the laboratory frame is of helical shape (see figure 2.3a).

Given a circularly polarized plane wave of finite, Gaussian pulse duration, the electron will be back at rest as soon as the laser amplitude a drops to zero and will again (as in the case of linear polarization) only be shifted in forward direction, with the corresponding trajectory shown in figure 2.3b.

2.2.3 Electron Ejection from a Focussed Laser Beam

In case not a plane wave is considered, but the laser amplitude is spatially varying as in a focussed laser beam, the electron is enabled to gain net energy from the electromagnetic field. While the electron motion for a general laser intensity profile can only be solved numerically, an analytical expression relating its final longitudinal p_z and transverse $p_\perp$ momentum after being ejected from the laser focus can be found [52], which also holds approximately for finite beam diameters

$$p_z = \frac{p_\perp^2}{2m_e c} \tag{2.30}$$

with $p_z = m_e c\,(\gamma - 1)$. Thus, the electron ejection angle θ is determined to be only dependent on its final relativistic Lorentz factor γ

$$\tan^2\theta = \left(\frac{p_\perp}{p_z}\right)^2 = \frac{2}{\gamma - 1} \tag{2.31}$$

Above equation has been verified experimentally [53].

2.3 Laser Propagation in a Plasma

So far, only the interaction of the laser field with a single electron was considered. Switching now to the situation of a laser beam propagating in a cold, collisionless plasma, the following dispersion relation for electromagnetic waves can be found [45]

$$\omega_L^2 = \omega_p^2 + c^2 k^2 \tag{2.32}$$

with the *electron plasma frequency* or *Langmuir frequency* ω_p being defined as

$$\omega_p = \sqrt{\frac{n_e e^2}{\epsilon_0 \gamma m_e}} \tag{2.33}$$

Here, n_e denotes the plasma electron density and the cycle-averaged relativistic Lorentz factor γ is given by [39]

$$\gamma = \sqrt{1 + a_0^2/2} \tag{2.34}$$

From equation 2.32 it is immediately clear that the electromagnetic wave is unable to propagate in case the plasma frequency ω_p exceeds the laser frequency ω_L.

The electron density at which this transition from transparent to opaque occurs, i.e., where $\omega_p = \omega_L$, is referred to as the *critical density* n_c,

$$n_c = \frac{\epsilon_0 \gamma m_e \omega_L^2}{e^2} \simeq 1.1 \times 10^{21}\, \gamma \left(\frac{\lambda_L}{\mu\mathrm{m}}\right)^{-2} \mathrm{cm}^{-3} \tag{2.35}$$

A plasma of density $n_e < n_c$ is accordingly identified as *underdense plasma*, while when of density above the critical density, $n_e > n_c$, as *overdense plasma*.

Given the scenario of an intense laser beam propagating in an underdense plasma, the corresponding refractive index is obtained from the dispersion relation 2.32:

$$\eta \equiv \frac{ck_L}{\omega_L} = \sqrt{1 - \frac{\omega_p^2}{\omega_L^2}} = \sqrt{1 - \frac{n_e e^2}{\epsilon_0 \gamma m_e \omega_L^2}} = \sqrt{1 - \frac{n_e e^2}{\epsilon_0 m_e \omega_L^2 \sqrt{1 + a_0^2/2}}} \tag{2.36}$$

At intensities above $\sim 10^{18}\,\mathrm{W/cm^2}$, i.e. $a_0 > 1$, relativistic effects will become significant. In a real experiment, the laser amplitude will typically be radially varying with $a_0(r)$ having its maximum on axis. Thus, γ and therefore also the refractive index η will be highest in the center as well. The plasma acts as a positive lens, hence focussing the beam. This phenomenon is known as *relativistic self-focussing*.

A similar effect which is referred to as *ponderomotive self-focussing* originates from electrons being expelled out of the peak intensity regions, leading to an electron density gradient where n_e exhibits a local minimum on axis. According to equation 2.36, the refractive index will again be maximized in the center, giving rise to beam focussing.

Self-focussing can result in the formation of relativistic channels in underdense plasmas, guiding the laser beam over many times its Rayleigh range. Such channels were first observed experimentally by Borghesi *et al.* [54].

In case of the laser pulse being incident on an overdense plasma, the electromagnetic wave will be unable to propagate through the plasma. However, an evanescent component will penetrate into the overdense region up to a characteristic length where the laser electric field has dropped by a factor of $1/e$. For a step-like plasma boundary and when neglecting collisions, this *collisionless skin depth* l_s is given by

$$l_s = \frac{c}{\omega_p} \tag{2.37}$$

It shall be noted here, that the situation can change when the interaction of a highly intense pulse with an ultrathin overdense foil instead of a semi-infinte plasma is considered. Novel features might become significant when both the laser wavelength

and the collisionless skin depth are comparable to or exceed the foil target thickness [55].

2.4 Laser Absorption in Overdense Plasmas

In laser-driven ion acceleration regimes accessible this far, the electromagnetic field energy is not directly transfered to the ions. Instead, electrons absorb energy from the laser pulse, setting up charge separation fields which in turn accelerate ions. This can be understood intuitively when replacing the electron mass in equation 2.14 by the proton mass, making equation 2.15 transform to

$$I_0 \lambda^2 = \zeta \left[4.62 \times 10^{24} \frac{\mathrm{W}}{\mathrm{cm}^2} \mu\mathrm{m}^2 \right] a_0^2, \tag{2.38}$$

Hence, currently available laser intensities ($I_0 \sim 10^{18} - 10^{22}\,\mathrm{W/cm^2}$) are still around three orders of magnitude below the threshold intensity for relativistic proton dynamics driven directly by the laser field. For a detailed understanding of mechanisms of ion acceleration from overdense targets, it is therefore instructive to start off by looking into processes of laser absorption into the electron population of such targets.

2.4.1 Collisional Absorption

At moderate laser intensities ($I\lambda_L^2 \leq 10^{15}\,\mathrm{Wcm^{-2}}\mu\mathrm{m}^2$), *collisional absorption* or *inverse bremsstrahlung heating* is the dominant absorption mechanism. Here, the electron motion is damped by collisions with ions and thus energy is transfered from the laser to the plasma. The electron-ion collision frequency ν_{ei} is given by [45]

$$\nu_{ei} \propto \frac{Z n_e}{T_e^{3/2}} \tag{2.39}$$

where Z stands for the number of free electrons per atom and T_e denotes the electron temperature. It can be seen that collisional heating is maximized for the highest density at which the laser is still able to propagate and therefore primarily takes place around the critical density n_c on a plasma density gradient.

As the electron temperature increases, the collision rate drops off and other absorption mechanisms gain significance.

2.4.2 Collisionless Absorption

Resonance Absorption

When a light wave is obliquely incident at an angle θ onto a plasma gradient, it will be specularly reflected at a density lower than the critical density $n_e = n_c \cos^2 \theta$. In case the electromagnetic wave is p-polarized, the laser field tunnels from the point of reflection to the critical density surface where it drives electrons to oscillate along the plasma density gradient. Fluctuations in the charge density arise, which can be resonantly enhanced and energy is transfered from the laser to an electron plasma wave. This phenomenon is referred to as *resonance absorption* [45].

Vacuum Heating

For steep plasma density gradients, resonance absorption eventually breaks down when the electron oscillation amplitude along the density gradient exceeds the plasma density scale length. However, given the identical situation of a p-polarized laser pulse that is obliquely incident onto the plasma boundary, electrons near the edge of the plasma-vacuum interface are directly exposed to the laser field. Those electrons are pulled out into vacuum by the electric field component orientated normal to the plasma boundary. As the field changes its direction, the electrons are sent back into the plasma. Since the plasma is overdense and the light field can therefore only penetrate up to a skin depth $l_s = c/\omega_p$, the accelerated electrons are beyond reach for the laser and will traverse the plasma until being finally absorbed by collisions. This "not-so-resonant, resonant absorption" was first described by Brunel [56, 57] and is thus known as *Brunel heating* or *vacuum heating*.

Relativistic j × B Heating

Another absorption mechanism where electrons on a step-like density profile gain energy directly from the laser field is *relativistic $j \times B$ heating*, introduced by Kruer and Estabrook [58]. For sufficiently large intensities ($a_0 \geq 1$), electrons are dominantly driven by the magnetic component of the Lorentz force. In case of linear polarization, the electrons will then undergo longitudinal oscillations at twice the laser frequency as derived in section 2.2.1. Whereas Brunel heating necessitates p-polarized light and oblique incidence to send electron bunches into the overdense plasma at frequency ω_L, relativistic $j \times B$ heating accelerates electron bunches into the target at frequency $2\,\omega_L$ and is most efficient for normal incidence. For normal incidence and circular polarization however, relativistic $j \times B$ heating is suppressed

due to the absence of an oscillatory component in the longitudinal electron motion (refer to section 2.2.2 for details). The same applies of course to vacuum heating and resonance absorption in this case. The fact that electron heating is drastically reduced for a circularly polarized pulse being normally incident onto a steep overdense plasma boundary turns out to be highly useful for a specific ion acceleration mechanism described in section 2.5.3 and chapter 7.

2.5 Ion Acceleration

As discussed above, present laser intensities prove insufficient to drive ions to relativistic quiver velocities in the laser field, making direct ion acceleration inaccessible. Nevertheless, ions can be accelerated to high energies by strong fields originating from charge separation of the less inertial electrons with respect to the ions. Since the pioneering experimental work carried out about 15 years ago [16, 59] this field of research has aroused increasing interest and different regimes for ion acceleration have been discussed theoretically and studied experimentally. Those include for instance Coulomb explosion of strongly ionized clusters [60, 61] or transverse explosion of a self-focussing channel [62] and induced electric fields in underdense plasmas [63–65].

In the following, the most significant ion acceleration mechanisms in the interaction with an initially solid density target will be presented, laying the theoretical foundations for the experimental studies of chapters 5, 6 and 7.

2.5.1 Target Normal Sheath Acceleration (TNSA)

Considering the scenario of an intense laser pulse ($a_0 \geq 1$) incident onto an initially solid density target, typically a foil in the micrometer thickness range, atoms on the front surface are rapidly ionized already on the rising edge of the pulse (refer to section 2.1 for details). The resulting front surface plasma is strongly heated by the absorption processes as explained in the previous section. To maximize absorption and to prevent potentially harmful back reflections from the target surface to the laser chain, p-polarization at oblique incidence is mostly chosen.

Energetic electrons are accelerated into the target and exit the foil on the back side. The underlying mechanism of electron transport as they traverse the foil is not fully understood yet, but is currently being investigated e.g. by means of optical transition radiation (OTR) [66]. Whereas energetic electrons are able to pass the overdense region of the target, in the classical TNSA regime the foil remains opaque

to the laser throughout the interaction. The transmitted hot electrons give rise to field ionization of atoms located in the back surface layers. Consequently, a quasi-static charge separation field builds up at the target rear side, reaching values on the order of TV/m. This field is maintained by an equilibrium of electrons being pulled back into the target and new electrons arriving from the front surface plasma. The extension of the field is determined by the hot electron Debye length λ_D

$$\lambda_D = \sqrt{\frac{\epsilon_0 k_B T_e}{e^2 n_e}} \tag{2.40}$$

where n_e denotes the mean hot electron density at the target back. Ions are accelerated in the quasi-static sheath field which is orientated normal to the surface, giving the process its name *target normal sheath acceleration* (TNSA). Ion acceleration via the TNSA mechanism is not restricted to the back surface. The front surface plasma also generates a sheath field, accelerating ions from the target front in the opposite direction. In figure 2.4, the main mechanisms for ion acceleration from an overdense, opaque target are illustrated.

The TNSA theory was introduced in 2001 by Wilks *et al.* [67] to explain experimental results obtained shortly before [1–4]. It is based on earlier work on hot electron driven plasma expansion into vacuum [68–72]. Later, Mora *et al.* [73] presented a detailed 1D model of free isothermal expansion of a collisionless plasma initially occupying half space. An exponentially decreasing spectrum is predicted, with a sharp cutoff energy $\mathcal{E}_{max}^{PEM}$ arising from the well defined ion front

$$\mathcal{E}_{max}^{PEM} = 2Zk_BT_e\left[\ln\left(\tau + \sqrt{\tau^2+1}\right)\right]^2 \tag{2.41}$$

Here, $\tau = 0.43\,\omega_{pi}t$ with acceleration time t and ion plasma frequency

$$\omega_{pi} = \sqrt{Zn_{e0}e^2/\epsilon_0 m_i}, \tag{2.42}$$

where m_i stands for the ion mass and Zn_{e0} denotes the initial ion density prior to expansion. The acceleration can be sustained as long as the electron temperature is kept high, i.e., as long as the laser heats electrons at the target front. Therefore, a good estimate is made by setting the acceleration time t equal to the laser pulse duration τ_L. A rather crude approximation for the electron temperature can simply be obtained from the electron quiver energy $k_BT_e = (\gamma-1)m_ec^2$ with $\gamma = \sqrt{1+a_0^2/2}$ according to equation 2.34.

For a thin foil target instead of a plasma occupying half space, the picture changes

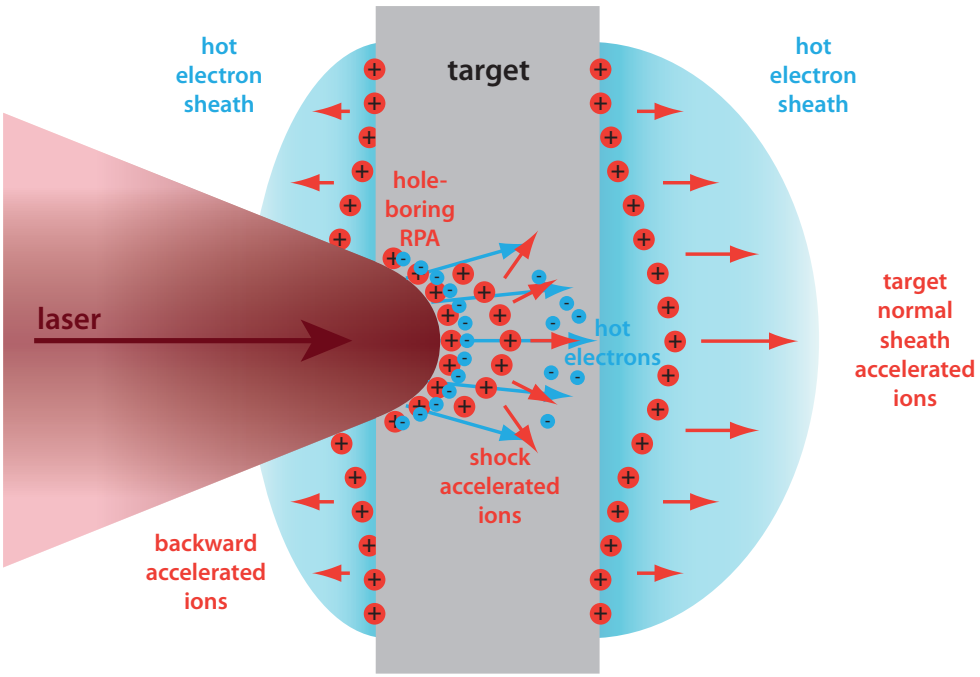

Fig. 2.4. *Illustrated are the main mechanisms for ion acceleration from an overdense, opaque target. The highly intense laser pulse incident from the left gives rise to rapid ionization and the generation of hot electrons which are able to traverse the foil. A sheath field of transverse dimension much larger than the focal spot size is set up at both surfaces, accelerating ions along target normal (TNSA). Additionally, the laser beam piles up a layer of electrons at its front while it bores a hole into the target plasma, thus pulling ions into the substrate (hole-boring radiation pressure acceleration (RPA)). This flow of ions can launch a shock wave which reflects ions to twice the shock speed while crossing the target. In case of a radially varying intensity distribution irradiating a planar surface, the shock front will not be planar and the shock accelerated ion component will exhibit a large angle of divergence.*

to an adiabatic instead of isothermal description [74]. The two regimes can be distinguished by the time $t_e = 2d/c$ it takes for hot electrons to completely fill the target of thickness d. While the isothermal approach is valid for $\tau_L \ll t_e$, the adiabatic model applies for $\tau \simeq t_e$ and in case of $\tau_L \gg t_e$ also the latter breaks down. To give a numerical example, for a pulse duration of 45 fs the condition $\tau \simeq t_e$ corresponds to a foil thickness of $\sim 7\,\mu$m. As the diamond-like carbon targets used in the presented experiments are about 2-3 orders of magnitude thinner, clearly a different theoretical model is needed to account for the experimental results of chapters 6 and 7.

Another analytical TNSA model has been proposed by Schreiber *et al.* [75] to predict the achievable maximum ion energy $\mathcal{E}_{max}$. Here, no detailed description of the plasma and its electron temperature T_e is needed and $\mathcal{E}_{max}$ only depends on the

laser pulse power and duration, the conversion efficiency into hot electrons η and a parameter B which stands for the radius of the electron exit area on the target rear side. When varying the foil thickness while assuming η to remain unchanged, the variation in $\mathcal{E}_{max}$ will thus only depend on B, given by $B = r_L + d\tan\theta$ with focal spot radius r_L and electron propagation half-angle θ when traversing the target.

Following the early measurements published in the year 2000 [1–4] and Wilks' theory, the TNSA regime has been widely studied experimentally in laser interactions with foil targets in the micrometer thickness range [5, 17–20, 24, 76–83]. It was found that a hydrocarbon contamination layer is typically present on the foil surfaces, originating from imperfect vacuum conditions. Owing to their high charge-to-mass (q/m) ratio, protons located in these surface layers are preferentially accelerated in the quasi-static TNSA field to energies up to 60 MeV at present [82]. Characterization of the obtained proton beam revealed excellent properties such as ultralow emittance and a small source size of $\sim 100\,\mu$m [17, 24, 80].

In order to efficiently transfer energy to heavier ions within the TNSA regime, proton contaminants need to be removed from the surface as they get accelerated quickly, thus shielding the quasi-static field for ions of lower q/m. Methods such as resistive heating, heating by a cw laser or ion gun etching have been successfully applied to generate a proton-free target surface, yielding ion cut-off energies of $\sim$ 3.5 MeV/u for carbon C^{5+} [5], 5 MeV/u for fluorine F^{7+} [18] and $>$ 10 MeV/u for iron ^{65}Fe [84].

Although the ion source size of $\sim 100\,\mu$m is small compared to conventional accelerators, it is still much larger than the focal spot size which is typically only around $5 - 10\,\mu$m in diameter. This discrepancy can be attributed to transverse spreading of the hot electrons as they are deflected in the field or while they recirculate through the target [76]. Consequently, the quasi-static field is spatially inhomogeneous, decaying both transversely as well as longitudinally due to shielding of inner ions. This naturally results in a field reduction in the center where the highest energetic ions are produced as well as a continuous instead of monoenergetic spectrum of the TNSA generated ion beam.

By restricting the ion source to a small volume where the sheath field is homogenous, the possibility to accelerate quasi-monoenergetic ion bunches has been demonstrated within the TNSA regime [5, 20]. However, this method suffers from a very low conversion efficiency as a similar result could be obtained by keeping the extended source size and instead cutting out a small portion of the continuous spectrum via a suitable energy filter placed downstream.

2.5.2 Shock Acceleration

So far, ion acceleration *away from the target* in the quasi-static ambipolar fields arising from a hot electron sheath at the front and rear surface of the foil was discussed (TNSA, refer to the previous section for details). In addition, as illustrated in figure 2.4 there is another ion population observed which originates from the target front side and is accelerated *into the bulk*.

Considering a relativistically strong laser field incident normally onto a solid density foil target, the longitudinal component of the Lorentz force (also referred to as Ponderomotive force) pushes electrons forward. Similar to a snow plow, the laser piles up a layer of electrons at the pulse front while gradually boring a hole into the target plasma. This very dense electron bunch pulls ions with it, thus generating a flow of ions moving into the target. The resulting ion velocity can be estimated by a balance of the dynamic pressure of ions with the laser light pressure [39]

$$n_i m_i v_i^2 = (1+R) I_L / c, \tag{2.43}$$

where n_i, m_i and v_i denote the ion number density, mass and velocity and R stands for the laser reflection efficiency. According to section 2.2 and 2.3, the laser intensity can be rewritten as

$$I_L = \zeta \frac{\epsilon_0 m_e^2 \omega_L^2 c^3}{2e^2} a_L^2 = \zeta \frac{n_c m_e c^3}{2} a_L^2 \tag{2.44}$$

Hence, the ion velocity is given by

$$\frac{v_i}{c} = \sqrt{\frac{(1+R) I_L}{m_i n_i c^3}} = a_L \sqrt{\frac{(1+R)\zeta}{2} \frac{m_e}{m_i} \frac{n_c}{n_i}} \tag{2.45}$$

This radiation pressure accelerated ion piston can launch an electrostatic collisionless laminar shock of velocity $v_s \simeq v_i$ propagating into the overdense plasma that maintains its velocity after the formation stage [85–87]. As the shock traverses the target, it picks up ions and reflects them to a maximum velocity of $v_{max} \simeq 2v_s$. The Mach number M of the shock is defined as

$$M = \frac{v_s}{c_s} \tag{2.46}$$

with the ion sound speed c_s being given by

$$c_s = \sqrt{\frac{5}{3}\frac{Zk_BT_e}{m_i}} \tag{2.47}$$

Silva *et al.* [38] carried out theoretical studies of high intensity laser interactions with overdense plasmas, giving evidence of the formation of high Mach number (2-3) electrostatic shocks and shock-accelerated ion beams that can exceed the energy of the TNSA-generated population. The shock-accelerated component manifests itself in a characteristic plateau structure in the ion spectrum.

However, when an initially planar target (such as a foil) is irradiated by a Gaussian or Airy-shaped focal spot as typically present experimentally, the shape of the shock front will not be planar but rather form a concave surface thus defocussing the shock-accelerated ion beam. In the scope of this PhD work, an experimental study was carried out demonstrating the possibility to compensate for this effect of hole-boring by means of a pre-curved target surface. A simple analytical model was developed to predict the evolution of the shock front, where the 1D model of Wilks *et al.* [39] was advanced to 2D to account for the scenario of a laser focus of spatially varying amplitude $a_L(r)$ incident onto a curved surface, showing excellent agreement with simulations ([40], refer to chapter 5 for details).

2.5.3 Radiation Pressure Acceleration / Light Sail / Laser Piston

Shortly after the first laser was experimentally demonstrated by Maiman in 1960 [6], the possibility to propel a rocket by a terrestrial laser beam was considered. The concept is simple as the conventional engine is replaced by a mirror forming a light sail and the rocket is accelerated by the radiation pressure of the reflected laser light. In 1966, Marx found that the efficiency of energy transfer from the laser to the accelerated object approaches unity as the object approaches a velocity close to the speed of light [88].

With the advent of ultra-high intensity laser systems, the idea of a light sail driven by the laser radiation pressure can be transfered to an ultra-thin foil target being accelerated as a whole in form of a high density plasma bunch reflecting the laser light. In a theoretical study, Esirkepov *et al.* showed that at intensities in excess of $10^{23}\,\mathrm{W/cm^2}$ radiation pressure acceleration (RPA) is indeed dominant over hot electron sheath acceleration (TNSA) and target ions reach relativistic velocities within a single laser cycle [89]. As the ions become relativistic that rapidly in this

so-called *laser-piston regime*, they are able to stay with the electron layer that is strongly pushed in forward direction and the foil can be regarded as a relativistic plasma mirror co-propagating with the laser pulse. Thus, ion acceleration becomes highly efficient and a monochromatic instead of continuous energy distribution is expected. However, currently available intensities are limited to values up to $10^{21} - 10^{22}\,\mathrm{W/cm^2}$, therefore making the laser-piston regime inaccessible at present.

Macchi *et al.* realized that a radiation pressure dominated regime can nevertheless be achieved at much lower intensities by changing the laser polarization from linear to circular [90]. In case of circularly polarized light incident normally onto a solid density plasma, all processes of electron heating as discussed in section 2.4.2 are suppressed due to the lack of oscillating components in the Lorentz force. Consequently, sheath acceleration of ions is inhibited as this mechanism necessitates the generation of highly energetic, hot electrons. The motion of electrons at the interaction surface is instead adiabatic and the laser ponderomotive force piles up a dense electron layer such that the radiation pressure is balanced by the charge separation field as in the initial stage of ion shock acceleration. For circular polarization however, the *absence* of a strong thermal pressure caused by hot electrons leads to a much more pronounced single density spike of compressed ions [91] as can be seen in further detail in the following. For simplicity, the analytical estimates below (based on the discussion found e.g. in [90–94]) are valid only in the limit of non-relativistic ions, in accordance with the non-relativistic ion energies obtained in the experimental studies of this PhD work.

In the first stage of the interaction, the target ions are immobile whereas the electrons are quickly piled up to an equilibrium position. Here, the generated charge separation field strength E_{z0} at the interface of the electron depletion and compression layer is given by the balance condition with the laser radiation pressure

$$\frac{\epsilon_0 E_{z0}^2}{2} = \frac{1+R}{c} I_L \tag{2.48}$$

This situation is illustrated schematically in figure 2.5a. For simplicity, a linear profile of E_z is assumed both within the depletion layer ($E_z = E_{z0} z l_d$ for $0 < z < l_d$) of thickness l_d and the compression layer ($E_z = E_{z0}[1-(z-l_d)/l_c]$ for $l_d < z < l_d + l_c$) of thickness l_c. From the Poisson equation one obtains

$$E_{z0} = e n_{e0} l_d / \epsilon_0 \tag{2.49}$$

with n_{e0} representing the initial free electron density of the target. By combining

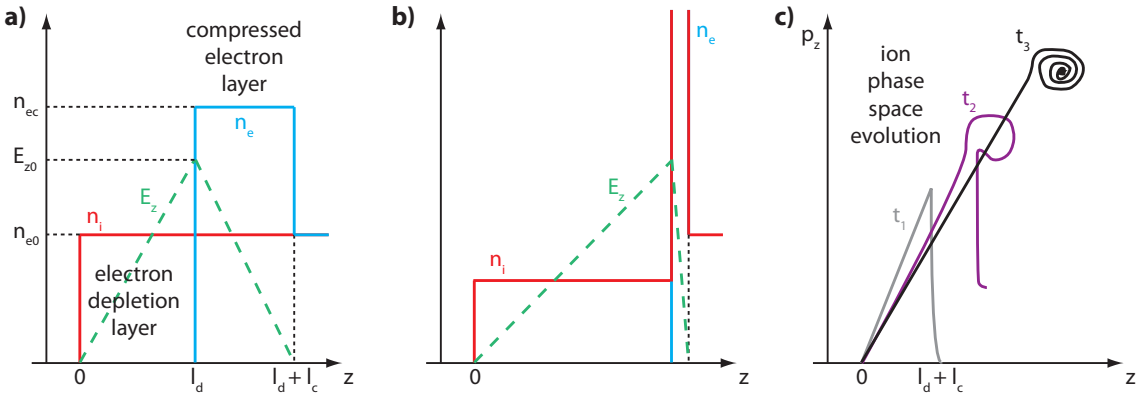

Fig. 2.5. *(a) Ion density n_i (red color), electron density n_e (blue color) and resulting electrostatic field distribution E_z (green color) at the equilibrium position where the laser radiation pressure is balanced by the charge separation field and the ions are still immobile, i.e., the initial stage of radiation pressure acceleration. Here, n_{e0} represents the initial free electron density, n_{ec} the compressed electron density and E_{z0} the maximum value of the charge separation field at the interface of electron depletion and compression layer. For ions located within the compression layer, E_z is constant over their respective trajectories and all ions reach the position $z = l_d + l_c$ at the same time (b). Thus, the ion and electron density ideally assumes an infinite value before hydrodynamic breaking occurs and ions are injected into the unperturbed plasma region. The corresponding ion phase space at the breaking time is sketched in grey color in (c). Owing to the continuing front surface acceleration and the ballistic evolution of the ion bunch, the phase space evolves into a series of loops at later times (marked in purple and black color). During this period of phase-stable acceleration, the relative velocity spread $\Delta v_i/v_i$ of ions originating from the compression region is narrowed down. (figure adapted from [90, 91])*

above two equations, an expression for the thickness of the depletion layer is found

$$l_d = \sqrt{\frac{2(1+R)I_L\epsilon_0}{cn_{e0}^2e^2}} \tag{2.50}$$

that can be transformed using equation 2.44, yielding

$$\frac{l_d}{\lambda_L}\frac{n_{e0}}{n_c} = \sqrt{\frac{(1+R)\zeta}{4\pi^2}}\,a_L \tag{2.51}$$

To give a numerical example, for a solid density target of $n_{e0} = 500n_c$, a laser pulse of amplitude $a_L = 5$ and wavelength $\lambda_L = 1\,\mu$m, circular polarization ($\zeta = 2$) and a reflectivity of $R = 1$ the thickness of the depletion layer calculates to $l_d \simeq 3\,$nm. Clearly, the foil thickness d should exceed l_d so that a balance between the laser ponderomotive force and the restoring force arising from the charge separation field E_z can be achieved and ions are efficiently accelerated. For foils thinner than l_d, the compressed electron layer will be permanently separated from the foil, leaving the ions behind. This regime however holds great promise for the generation of ultrathin,

highly dense electron bunches that could potentially be employed as a relativistic mirror for coherent X-ray generation via Thomson backscattering [95–97].

In a second step, ions start to respond to the electrostatic field E_z. Within the electron depletion layer, E_z is a constant over the ion trajectories and increases with z. Hence, those ions never catch up with ions in the compression region and form a shelf of decreasing density, consequently being of no interest for the further acceleration process. Assuming quasi-equilibrium electron dynamics and a constant radiation pressure of $(1 + R)I_L/c$, ions originating from the compression layer will in contrast all reach the longitudinal position $z = l_d + l_c$ at the same time and the ion density ideally assumes an infinite value. This second stage of the interaction is depicted in figure 2.5b and the corresponding ion phase space is sketched in grey color in figure 2.5c. The average ion velocity v_i at that moment is given by equation 2.45, which is the velocity of the laser reflection front at the breaking time.

As the ions subsequently enter the unperturbed plasma region, the compressed electron cloud self-consistently adjusts its position and density. Assuming constant radiation pressure, more and more ions will be accelerated to the same average velocity v_i until the compressed electron layer reaches the rear surface of the foil. At this stage, the whole focal volume of the target is set in motion. Owing to the cold electron population that is accompanying the highly dense ion bunch, space charge effects that might lead to Coulomb explosion are neutralized. Instead, the ions propagate ballistically in a quasi-neutral plasma that is continuously accelerated by the laser radiation pressure just as the light sail intended for space travel mentioned earlier. Thus, this final stage of the interaction is often referred to as *light sail acceleration*. The resulting final velocity v_f can be estimated by equating the final momentum of the target per unit area, $n_{i0}m_i v_f d$, with the radiation pressure exerted onto the target times the laser pulse duration, $(1 + R)I_L\tau_L/c$, yielding

$$\frac{v_f}{c} = \frac{(1 + R)I_L\tau_L}{c^2 n_{i0} m_i d} \tag{2.52}$$

The achievable ion energy is thus proportional to the square of the laser energy fluence, $(I_L\tau_L)^2$, and inverse proportional to the initial ion areal density squared, $(n_{i0}d)^2$, where a lower limit for the normalized areal density $\sigma = (d/\lambda_L)(n_{e0}/n_c)$ is given by equation 2.51 with $d \geq l_d$.

While the ions are accelerated, their relative velocity spread $\Delta v_i/v_i$ is narrowed down since the slowest, trailing ions experience the strongest field E_{z0}. This continuing process is comparable to phase-stable acceleration (PSA) in a conventional radio frequency (RF) linac, where a proper phase is chosen to synchronously accel-

erate and bunch the ion beam [98]. To explain the associated features of PSA in the context of the discussed laser-driven ion acceleration scenario in more detail, a reference ion is introduced which is situated at a position $z_r = l_d + l_c/2$ at the center of the compression region, moving synchronously with the compressed electron layer. Assuming a linear electric field distribution as described above, a test ion at a position z_i inside the compression region is subject to a force $F_i = q_i E_{z0}[1-(z_i - l_d)/l_c]$, leading to the equation of motion

$$\frac{\mathrm{d}^2 z_i}{\mathrm{d}t^2} = E_{z_0}\frac{q_i}{m_i}\left(1 - \frac{z_i - l_d}{l_c}\right) \tag{2.53}$$

where

$$\frac{\mathrm{d}^2 z_r}{\mathrm{d}t^2} = \frac{E_{z_0}}{2}\frac{q_i}{m_i} \tag{2.54}$$

defines the trajectory of the reference particle for which $E_{z_r} = E_{z0}/2$ is constant over the whole duration of phase stable acceleration. Introducing the distance $\xi = (z_i - z_r)$ between test ion and reference ion with $-l_c/2 \leq \xi \leq l_c/2$, above equations can be rewritten as

$$\frac{\mathrm{d}^2 \xi}{\mathrm{d}t^2} = -E_{z_0}\frac{q_i}{m_i}\frac{\xi}{l_c} \tag{2.55}$$

or

$$\ddot{\xi} = -\Omega^2 \xi, \qquad \Omega^2 = \frac{q_i E_{z0}}{m_i l_c} \tag{2.56}$$

Thus, assuming E_{z0} to be slowly varying in time, ions within the compression layer perform harmonic oscillations around the position of the reference particle at a frequency $\Omega/(2\pi)$, with the longitudinal phase motion (ξ, t) being given by

$$\xi = \xi_0 \sin(\Omega t) \tag{2.57}$$

$$\dot{\xi} = -\xi_0 \Omega \cos(\Omega t) \tag{2.58}$$

The velocity spread Δv_i of the ion bunch can accordingly be estimated from equation 2.58, where the maximum particle displacement is determined by the condition

$\xi_{max} \leq l_c/2$, and transformed using equations 2.49 and 2.50, yielding

$$\begin{aligned}\Delta v_i \simeq 2\xi_0\Omega \simeq l_c\Omega &= l_c\sqrt{\frac{q_i E_{z0}}{m_i l_c}} \\ &= \sqrt{\frac{l_c q_i e n_{e0} l_d}{m_i \epsilon_0}} \\ &= \left[\frac{(1+R)\zeta}{4\pi^2}\right]^{1/4}\sqrt{\frac{l_c q_i e \lambda_L n_c a_L}{m_i \epsilon_0}} \\ &= [(1+R)\zeta]^{1/4}\sqrt{l_c Z\frac{m_e}{m_i} c\omega_L a_L}\end{aligned} \tag{2.59}$$

where $q_i = Ze$. A good approximation for the thickness of the compression layer is provided by the laser skin depth, i.e., $l_c \simeq l_s = c/\omega_p$, leading to

$$\Delta v_i \simeq [(1+R)\zeta]^{1/4}\left(\frac{n_e}{n_c}\right)^{-1/4} c\sqrt{Z\frac{m_e}{m_i}a_L} \tag{2.60}$$

Above described internal bunch dynamics manifest themselves in a characteristic loop structure in the ion phase space that is sketched in figure 2.5c. A quasi-monoenergetic ion spectrum with conversion efficiency much in excess of the previously realized TNSA based experiments with reduced ion source size is expected to be obtained.

Owing to its enormous potential for the generation of dense, monochromatic ion bunches at conversion efficiencies approaching unity, the described mechanism has just recently been studied in much detail in theory, creating a huge number of theoretical publications that call for experimental validation [91–94, 98–109]. Within this PhD work, the first experimental proof of RPA driven by circularly polarized light was achieved [42]. An in-depth description of the measurement is given in chapter 7.

Chapter 3

Experimental Methods I - High Intensity Laser Systems

In this chapter, a compressed introduction to the laser systems utilized to conduct the presented experiments will be given. That section will be preceded by a description of the basic concepts and key technologies required for synthesizing ultrashort and highly intense light bursts.

3.1 Fundamentals of Ultrashort High Intensity Pulse Generation

3.1.1 The Concept of Mode-Locking

To obtain pulsed lasers of ultra high intensity, a technique is needed to store the laser energy in single, ultrashort pulses rather than in continuous-wave (cw) beams. A breakthrough in this field happened in the 1960s when the concept of mode-locking was developed [10, 11], which will be explained briefly.

For simplicity, the laser spectrum is assumed to be constant over frequency. The electric field at a fixed position $z = 0$ inside the cavity can therefore be written as a sum over all oscillating axial modes

$$E(t) = \frac{E_0}{2} \sum_{n=-s}^{s} e^{i[(\omega_0 + n\Delta\omega_{ax})t + \phi_n]} + c.c. \tag{3.1}$$

with the frequency spectrum centered at ω_0 and axial mode distance $\Delta\omega_{ax}$. The limits of the sum are given by $s = (N_M - 1)/2$ with N_M being the number of axial modes oscillating above threshold. By introducing a process to *lock* all modes at

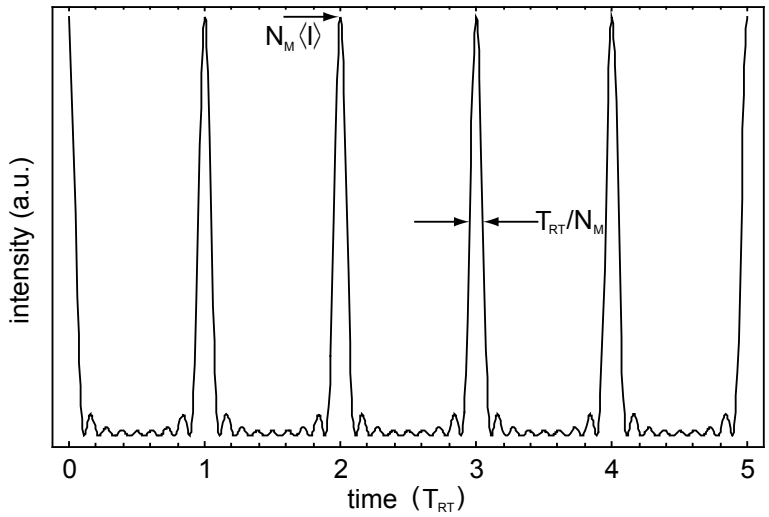

Fig. 3.1. *Intensity pattern resulting from $N_M = 9$ locked modes and a constant frequency spectrum.*

a constant and equal value of phase (for simplicity $\phi_n = 0$ is supposed), the total electric field becomes

$$E(t) = \frac{E_0}{2} e^{i\omega_0 t} \sum_{n=-s}^{s} (e^{i\Delta\omega_{ax} t})^n + c.c. \tag{3.2}$$

$$= \frac{E_0}{2} e^{i\omega_0 t} \frac{\sin(N_M \Delta\omega_{ax} t/2)}{\sin(\Delta\omega_{ax} t/2)} + c.c. \tag{3.3}$$

The intensity $I(t)$ corresponding to this electric field is shown exemplarily for $N_M = 9$ locked modes in figure 3.1. With an increasing number of locked modes N_M, the peak intensity I_{peak} of the main pulses increases with respect to the average intensity $\langle I \rangle$ as $I_{peak} = N_M \langle I \rangle$, while their FWHM pulse duration τ decreases as $\tau \approx T_{RT}/N_M$ with T_{RT} being the round-trip time of one pulse in the cavity [110]. Thus, by locking a large number of modes at constant, equal phase, the peak power can be greatly increased until essentially the whole power is stored in the main pulses with a negligible amount in between.

In figure 3.1, mode locked pulses are shown that result from a uniform frequency spectrum. Besides the primary pulses, $N_M - 2$ much weaker subsidiary side peaks appear per period. For a Gaussian spectrum, mode-locking again yields a train of periodically spaced pulses, but the aforementioned small local maxima vanish. Beyond that, the main pulses now exhibit gaussian shapes in time.

An intuitive time-domain picture of a mode-locked laser corresponds to a single pulse bouncing back and forth inside the cavity. The resulting output is a pulse

train with repetition rate RR

$$RR = \frac{1}{T_{RT}} = \Delta\nu_{ax} \tag{3.4}$$

Kerr-Lens Mode-Locking

There are various approaches to achieve mode-locking in a laser cavity. Generally, all of them can be referred to as either *active* or *passive* techniques.

An example for *active mode-locking* would be inner-cavity loss modulation via a fast shutter, e.g. an acousto-optic modulator (AOM). The AOM can be driven in such a way so that except during a small time around the minimum of the introduced loss the cavity is below threshold. Therefore, pulses are forced to form that lie within these loss minima at distances of T_{RT}. The pulse duration achieved with this technique mainly depends on two characteristics of the AOM:

- Modulation depth Δ_m
- Modulation frequency f_m

A larger modulation depth will result in shorter pulses. In simple words, this can be attributed to the fact that the width of the "low-loss window" decreases for increasing Δ_m, thus shortening the pulse. For acousto-optic modulators, Δ_m is generally proportional to the RF power P_m supplied to it [110]

$$\Delta_m \propto P_m \tag{3.5}$$

and therefore the pulse duration shows a weak dependence on P_m

$$\tau \propto P_m^{-1/4} \tag{3.6}$$

A higher modulation frequency f_m will give shorter pulses as well. That effect can again be explained by the narrowing of the "low-loss window", this time due to the higher RF frequency.

However, in practice both modulation depth and frequency are limited, so that the theoretical boundary for the pulse length (which is given by the bandwidth of the gain medium, see section 3.1.2) does not lie within close reach. Pulse durations achieved by active mode-locking typically range from several 100 picoseconds down to a few picoseconds [111, 112]. Therefore, for laser cavities producing pulses of only a few femtoseconds, different approaches are used. A very popular technique is *Kerr-lens mode-locking* (KLM), which is referred to as a way of *passive mode-locking*.

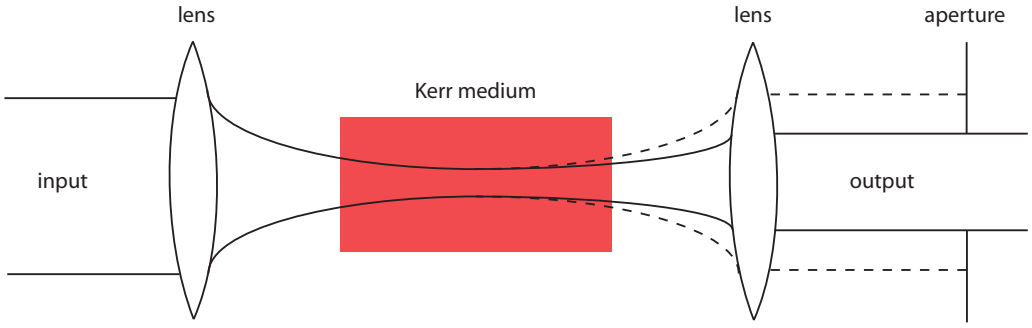

Fig. 3.2. *Schematic illustration of Kerr-lens mode-locking. By introducing an aperture into the cavity, self-focusing in the gain medium results in selective attenuation of the low power beam (dashed curve), while the high power mode (solid line) remains unaffected.*

The KLM mechanism is directly related to the *optical Kerr effect*, which describes a nonlinear change in the refractive index induced by the electric field of an electromagnetic wave. The total refractive index can be written intensity-dependent by means of the equation [110]

$$n = n_0 + n_2 I \tag{3.7}$$

with intensity $I = c\,\epsilon_0\,n_0\langle E^2\rangle$, where $\langle E^2\rangle$ represents the cycle-averaged value of the field squared. Since the spatial profile of a Gaussian (or sech^2) pulse exhibits larger intensities for parts of the beam that are closer to the optical axis, the refractive index will be higher for those parts as well, while the beam is propagating through a nonlinear optical medium. Therefore, a nonlinear optical medium with positive n_2 will act to a Gaussian pulse just as an intensity-dependent convex lens and focus the beam. This effect is called *self-focusing*.

In figure 3.2 it is schematically depicted how Kerr-lens mode-locking takes advantage of that self-focusing effect. An increase in the intensity of the input beam will result in a decreasing beam diameter at the output. By including an intra cavity aperture into the setup, this intensity dependent beam size modulation results in a subsequent modulation in the propagation losses. While the circulating high intensity pulse mode is able to pass the iris ideally unaffected, the low intensity cw mode gets absorbed to a great extent and is kept below threshold for lasing. As figure 3.2 shows, the iris acts as a filter between both modes of operation. This technique is denoted as *hard aperture mode-locking*.

In contrast to the hard aperture that has to be added to the cavity, there is a second discrimination mechanism that is already present in every setup. Due to the spatial profile of the pump beam exciting the gain medium, the gain profile itself

gain medium	HeNe	Nd:YAG	Nd:glass	diode	$Ti^{3+} : Al_2O_3$
$\Delta\nu_{gain}(s^{-1})$	1.5×10^9	1.2×10^{11}	7.5×10^{12}	2.5 to 10×10^{12}	1.0×10^{14}

Tab. 3.1. *Examples of the FWHM gain bandwidth $\Delta\nu_{gain}$ for different materials commonly used (numbers taken from [113]).*

exhibits a spatial modulation as well. This results in the formation of an intrinsic *soft aperture*. Cavity modes that are showing the largest overlap with the excited gain medium are amplified the most on every round trip.

Both the hard as well as the soft aperture contribute to a selective attenuation of low intensity modes, which leads to the buildup of short, high intensity pulses circulating in the passively mode-locked cavity.

3.1.2 Time-Bandwidth Product

For a square gain spectrum and a number of N_M modes locked, the pulse width τ of the primary pulses is close to (see section 3.1.1)

$$\tau \approx \frac{T_{RT}}{N_M} \tag{3.8}$$

This can be rewritten with the axial mode spacing $\Delta\nu_{ax} = 1/T_{RT}$

$$\tau \approx \frac{1}{\Delta\nu_{ax} N_M} \tag{3.9}$$

Assuming that all oscillating modes are locked, the *gain bandwidth* (or *amplification bandwidth*) $\Delta\nu_{gain}$, which is defined as FWHM of the gain spectrum, can be approximated by

$$\Delta\nu_{gain} \approx \Delta\nu_{ax} N_M \tag{3.10}$$

Therefore, the pulse duration of the main pulses becomes

$$\tau \approx \frac{1}{\Delta\nu_{gain}} \tag{3.11}$$

Equation 3.11 denotes the ultimate pulse width that can be obtained from a mode-locked laser with uniform gain spectrum, while

$$\tau\Delta\nu_{gain} \approx 1 \tag{3.12}$$

is referred to as *time-bandwidth product*. Examples for $\Delta\nu_{gain}$ of prevalent amplification media are given in table 3.1.

Given a gaussian gain spectrum, the pulses obtained from a mode-locked cavity will exhibit a gaussian envelope in time as well (see section 3.1.1) having an intensity $I(t)$ as follows:

$$I(t) = I_0 \exp\left(-4\ln 2\frac{t^2}{\tau^2}\right) \tag{3.13}$$

The FWHM of one pulse in the time domain is therefore represented by τ.

Fourier transforming the associated electric field

$$E(t) = E_0 \exp\left(-2\ln 2\frac{t^2}{\tau^2}\right) \tag{3.14}$$

$$\Rightarrow \tilde{E}(\nu) = \tilde{E}_0 \exp\left(-\frac{\pi^2\tau^2\nu^2}{2\ln 2}\right) \tag{3.15}$$

results in an intensity spectrum given by

$$\tilde{I}(\nu) = \tilde{I}_0 \exp\left(-\frac{\pi^2\tau^2\nu^2}{\ln 2}\right) \tag{3.16}$$

Thus, the FWHM spectral range or bandwidth $\Delta\nu$ of the pulse is

$$\Delta\nu = \frac{2\ln 2}{\pi\tau} \tag{3.17}$$

and the time-bandwidth product calculates to

$$(\tau\Delta\nu)_{\text{gaussian}} = \frac{2\ln 2}{\pi} \approx 0.4413 \tag{3.18}$$

Similarly, the time-bandwidth product of a $\sec^2$ pulse can be ascertained to be

$$(\tau\Delta\nu)_{\sec^2} = \frac{4 \times \operatorname{arccosh}^2\sqrt{2}}{\pi^2} \approx 0.3148 \tag{3.19}$$

For a given spectral width $\Delta\nu$ of a laser pulse, a lower limit of the temporal width τ can be obtained from its respective time-bandwidth product. A pulse at that minimum duration level is often referred to as *transform-limited*.

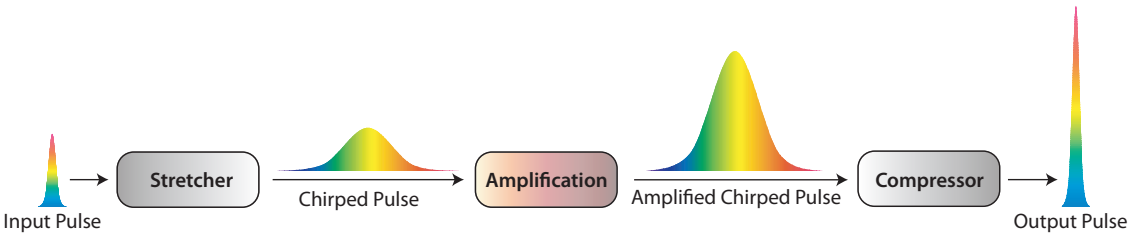

Fig. 3.3. *Schematic illustration of* ***C****hirped* ***P****ulse* ***A****mplification (CPA): The pulse frequencies are separated spatially in the laser propagation direction in order to lower the peak intensity and allow safe amplification. A second dispersive element ideally removes the chirp completely, resulting in an ultrashort pulse with high peak intensity at the output.*

3.1.3 Chirped Pulse Amplification

Up to the mid 1980s, the ambition to build lasers with focused intensities in excess of $10^{15}\,\mathrm{W/cm^2}$ did not seem feasible. The reason for this threshold was given by the fact that the unfocused intensities in the amplification stages are limited by the damage threshold of the gain material and other optics. At that time, the common concept to deal with this problem was to increase the beam diameter prior to amplification, thus reducing the pulse intensity. This evolution led to laser systems incorporating optics with huge apertures such as SHIVA and NOVA, both located at Lawrence Livermore National Lab (LLNL). With an aperture of 50 cm in the final amplification stage, NOVA was capable of producing around 100 kJ of infrared light at 1064 nm wavelength in a 2-4 ns pulse. Due to the enormous costs of such systems, implementation was restricted to National Lab facilities.

In 1985, this quandary was overcome with the presentation of a new, revolutionary concept by D. Strickland and G. Mourou [12]. Rather than decreasing the intensity of the pulses by spatial stretching, they proposed to introduce a stretch in the time domain. This approach, referred to as **C**hirped **P**ulse **A**mplification (CPA) takes advantage of the pulse bandwidth and is schematically displayed in figure 3.3. By including a dispersive element such as a pair of gratings into the laser chain prior to the first amplification stage, the pulse's instantaneous frequency becomes linearly time-varying, the pulse is *chirped*. This reduction in intensity allows the use of small optics for all amplification stages. In order to regain a short pulse duration, the chirp of the fully amplified pulse can be almost completely compensated by a second set of dispersive optics. Owing to the fact that a small beam diameter is sufficient for the whole laser with the exception of the final compressor, the construction of table-top terrawatt laser systems became possible, allowing for studies of laser-matter interactions at extreme intensities of up to $10^{22}\,\mathrm{W/cm^2}$ at present [13].

3.1.4 Optical Parametric Amplification (OPA)

However, even though conventional laser amplification methods combined with key technologies such as Kerr-lens mode-locking or chirped pulse amplification can provide very high peak power levels, the resulting minimal pulse duration is determined by the gain bandwidth of the active material (refer to section 3.1.2 for details), thus being limited to the tens-of-femtoseconds range so far.

In recent years the technique of optical parametric amplification (OPA), which does not suffer from this constraint, has opened up a new path towards creating few-cycle pulses [114–122]. Amplification takes place within a nonlinear optical crystal, where phase matching in non-collinear geometry allows for enormous bandwidths [114] which can be significantly larger than that of any known conventional laser-amplifier medium. In addition, the gain can be very high even in a short length of material, thus reducing the accumulation of nonlinear phase which arises from passing the high-intensity beam through material, also referred to as B-integral. Moreover, in contrast to laser amplifiers much less energy is converted into heat, thereby eliminating thermal distortions of the beam and enabling high repetition rates.

To obtain the highest possible peak intensities, in high power systems OPA is usually combined with the technique of chirped pulse amplification, which is described in the previous section, to a scheme named optical parametric chirped pulse amplification (OPCPA) that was first proposed by Dubietis *et al.* [123]. Employing such a system, energies as high as 35 J stored in pulses of 84 fs FWHM duration have been achieved [124], while in the few-cycle regime 7.9 fs pulses of energy 130 mJ were demonstrated recently [125].

When using short pump pulses, OPCPA represents a greatly promising route towards the generation of ultra-high intensity pulses at ultra-high contrast, which are a crucial prerequisite for a large number of laser-plasma interaction experiments. Within the framework of this PhD thesis, such a short pulse pumped OPA stage combined with the chirped pulse amplification technique (SPP-OPCPA) was developed to pioneer future few-cycle, ultra-high contrast, ultra-high intensity facilities like the Petawatt Field Synthesizer (PFS) project [44] that is pursued at MPQ (refer to chapter 8 for details). In the following, a brief introduction to OPA will be given.

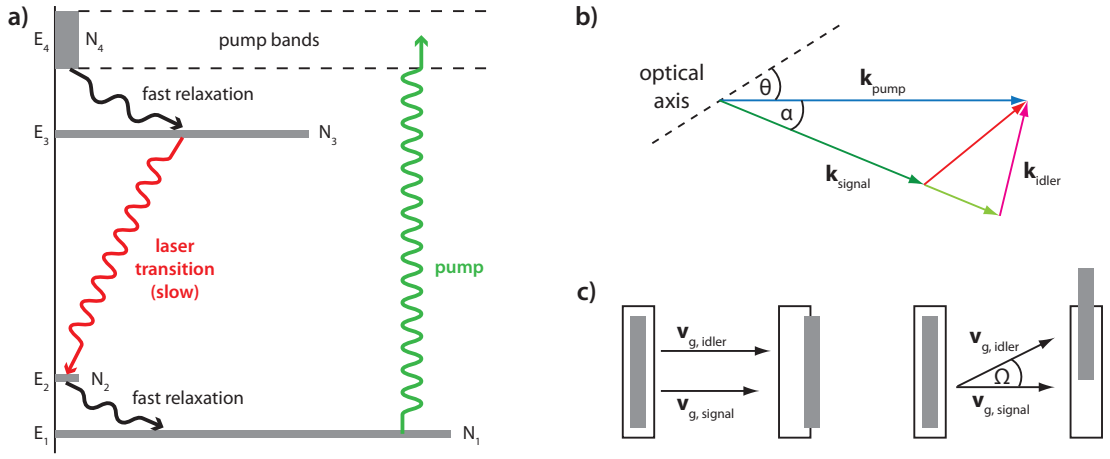

Fig. 3.4. *(a) illustrates an idealized four-level laser system with $3 \rightarrow 2$ being the laser transition. Excited states within the pump bands undergo a rapid relaxation to the upper laser level which is long-lived when compared to the lower level 2. Hence, a population inversion $N_2/N_3 \ll 1$ builds up, resulting in amplification of incident signal photons by stimulated emission. In (b), the basic NOPA geometry with pump-seed angle α and phase matching angle θ is depicted. Broadband phase matching can be achieved in the non-collinear setup by compensating for the group velocity mismatch between signal and idler as displayed schematically in (c). (c adapted from [126])*

Conventional Laser Amplification vs. Non-Collinear Optical Parametric Amplification (NOPA)

In OPA, the underlying mechanism of energy transfer from pump photons to signal photons is fundamentally different from conventional laser amplification. As a reminder, figure 3.4a illustrates an idealized four-level laser scheme which provides a simple but surprisingly accurate model for a multitude of real laser systems such as Nd:YAG or Nd:glass. Here, level 4 represents the combination of all levels lying above the upper laser level in the real atomic system. It is desirable that many of these levels be in fact broad absorption bands, thus enabling optical pumping by a broadband pump lamp to be efficient. The upper laser level is formed by level 3, while level 2 stands for the the lower laser level and level 1 for the lowest or ground level.

In a well designed laser system the $4 \rightarrow 3$ relaxation will be very fast, whereas the upper laser level is typically long-lived by comparison. Given the condition that the lower laser level is of much shorter lifetime than the upper one, a sizable population inversion $N_2/N_3 \ll 1$ will be obtained. Gain is achieved by stimulated emission in the presence of signal photons. In other words, the laser active medium serves as an energy reservoir, generally being pumped on much longer timescales than the signal pulse duration. Alongside with the process of stimulated emission,

this energy reservoir is also being depleted by spontaneous emission of photons which becomes particularly significant in high-gain amplifiers, giving rise to an amplified spontaneous emission (ASE) background of much longer duration compared to the signal pulse.

Above described scenario stands in strong contrast to OPA, where energy is directly transfered from a high frequency and high intensity pump beam at ω_p to a lower frequency, lower intensity signal beam at ω_s within a suitable nonlinear crystal such as β-barium borate (BBO) or lithium triborate (LBO). A third beam, the idler, is simultaneously generated at frequency ω_i so that conservation of energy is satisfied

$$\hbar\,\omega_p = \hbar\,\omega_s + \hbar\,\omega_i\,. \tag{3.20}$$

In addition, the condition of momentum conservation (i.e., the *phase matching condition*) must be fulfilled

$$\hbar\,\vec{k}_p = \hbar\,\vec{k}_s + \hbar\,\vec{k}_i \tag{3.21}$$

with $\vec{k}_p$, $\vec{k}_s$ and $\vec{k}_i$ being the wave vectors of pump, signal and idler, respectively. Here, the special case where signal and idler beam are of equal frequency $\omega_p/2$ is referred to as *degeneracy condition*.

Given a collinear three wave interaction and type I phase matching in a negative uniaxial crystal ($n_e < n_o$), above condition can simply be recast as

$$n_{ep}(\theta)\,\omega_p = n_{os}\omega_s + n_{oi}\omega_i\,. \tag{3.22}$$

In this case the pump beam propagates as an extraordinary ray with index of refraction n_{ep} varying with the *phase matching angle* θ between the pump wave vector and the optical axis of the crystal, whereas n_{os} and n_{oi} of the ordinary signal and idler beams are θ-independent. Generally, θ shows a less pronounced wavelength dependence for type I geometry when compared to type II phase matching (where either the signal or the idler beam are also extraordinary rays). As a consequence, type I phase matching is typically used to achieve the shortest pulses in broadband optical parametric amplifiers, while type II offers relatively narrow bandwidths over broad tuning ranges thus being suitable for a number of spectroscopic applications (further detail on this subject can be found e.g. in [126]).

Considering the interaction of three (non-monochromatic) pulses propagating in the nonlinear crystal at different group velocities $v_g = d\omega/dk$, the group velocity

mismatch (GVM) between pump and signal/idler pulses limits the length over which amplification takes place. Additionally, the phase matching bandwidth is narrowed by GVM between the signal and idler beam. To overcome this constraint, an extra degree of freedom is introduced by the pump-signal angle α in non-collinear optical parametric amplification (NOPA). The basic interaction geometry is illustrated in figure 3.4b. Broadband phase matching can be achieved when adjusting α such that the signal group velocity equals the projection of the idler group velocity along the signal direction, i.e.,

$$v_{gs} = v_{gi} \cos \Omega \tag{3.23}$$

where Ω stands for the angle between signal and idler. This effect is schematically depicted in figure 3.4c. While in collinear geometry signal and idler propagating at different group velocities get quickly separated, giving rise to pulse lengthening and bandwidth reduction, in the NOPA case the two pulses remain overlapped for longer even though some lateral walk-off takes place.

Alongside with broadband signal amplification, NOPA also results in the generation of a broadband idler pulse which is therefore potentially compressible to very short pulse durations as well. However, as shown pictorially in figure 3.4b, the idler exhibits an angular spectral dispersion as the emission angle Ω is wavelength dependent. Consequently, in practice that concomitant phenomenon has to be compensated for especially in ultra-broadband NOPA systems, e.g. by use of a suitable grating-cylindrical mirror combination [127, 128]. An example for a setup where the obtained idler beam is subsequently used for further amplification is the non-collinear SPOPA cleaning stage as implemented in the TRIDENT frontend type 1 and 2 (refer to section 3.2.3 for details). Here, the effect of angular spectral dispersion is much less pronounced though when compared to a setup aiming at few-cycle pulses, owing to the small bandwidth of the system.

Analogous to amplified spontaneous emission (ASE) in conventional laser amplifiers, in OPA *parametric superfluorescence* gives rise to an unwanted pulse background. This parasitic process refers to parametric amplification of vacuum or quantum noise and can also be thought of as two-photon spontaneous emission from a virtual level excited by the pump field. As in the case of ASE, parametric superfluorescence is of major significance when small seed energies and large gain factors are used. Nevertheless, by employing pump pulses of only tens to hundreds of femtoseconds in duration, the generated pedestal can be limited to much shorter timescales than the typically ns-long ASE background occurring in conventional

laser amplifiers.

3.2 Laser Systems Utilized for Ion Acceleration Studies

3.2.1 The ATLAS Laser Facility

The **A**dvanced **T**itanium:sapphire **LAS**er (ATLAS) located at MPQ constitutes a table-top short pulse TW-power CPA laser device based on Ti:sapphire as amplification medium. The system as it was used for the experiments described in chapter 5 represents a 2005 upgraded version [129, 130] of the former ATLAS 10 laser, which originates from 1996 [131].

A schematic overview of the system is given in figure 3.5. Initially, the laser chain is seeded by a train of pulses of energy $\sim 3\,\mathrm{nJ}$, which are generated by a modified version of a commercially available Femtolasers Femtosource Rainbow oscillator at a repetition rate of $\sim 70\,\mathrm{MHz}$. A thin Ti:sapphire crystal serves as gain medium in the Kerr-lens mode-locked cavity (see section 3.1.1), producing a broad spectrum of width $> 300\,\mathrm{nm}$ centered at 800 nm wavelength that allows for the generation of pulses as short as $< 7\,\mathrm{fs}$. The crystal is pumped by a $\sim 3.5\,\mathrm{W}$ Coherent Verdi V6 diode-driven frequency-doubled Nd:YVO_4 solid-state cw laser at a wavelength of 532 nm. Group delay dispersion (GDD) is controlled by use of multi-layer dielectric chirped mirrors and fused silica wedges.

The oscillator output pulses are guided through a Faraday isolator and are spatially filtered before entering a multi-pass amplifier, which is referred to as preamplifier. Amplification prior to the subsequent stretcher and regenerative amplifier is a crucial prerequisite for the generation of high temporal contrast pulses. Seeding the regenerative amplifier directly from the oscillator would result in a great amount of amplified spontaneous emission (ASE) building up in the cavity. In order to restrain the intensity ratio of the ASE pedestal with respect to the main peak to final values around 10^{-8}, an energetic seed has to be provided for the regenerative amplifier. Thus, out of the 70 MHz train, 10 pulses per second are fully amplified over nine passes to an energy of $\sim 2\,\mu\mathrm{J}$. The Ti:sapphire medium is hereby pumped by 25 mJ pulses of several nanoseconds duration originating from a frequency doubled, Q-switched Continuum Minilite Nd:YAG laser at 10 Hz repetition rate.

After traversing the preamplifier, the pulses are elongated to a duration of $\sim 350\,\mathrm{ps}$ by means of a positive dispersion stretcher set up in Martínez-type [132]

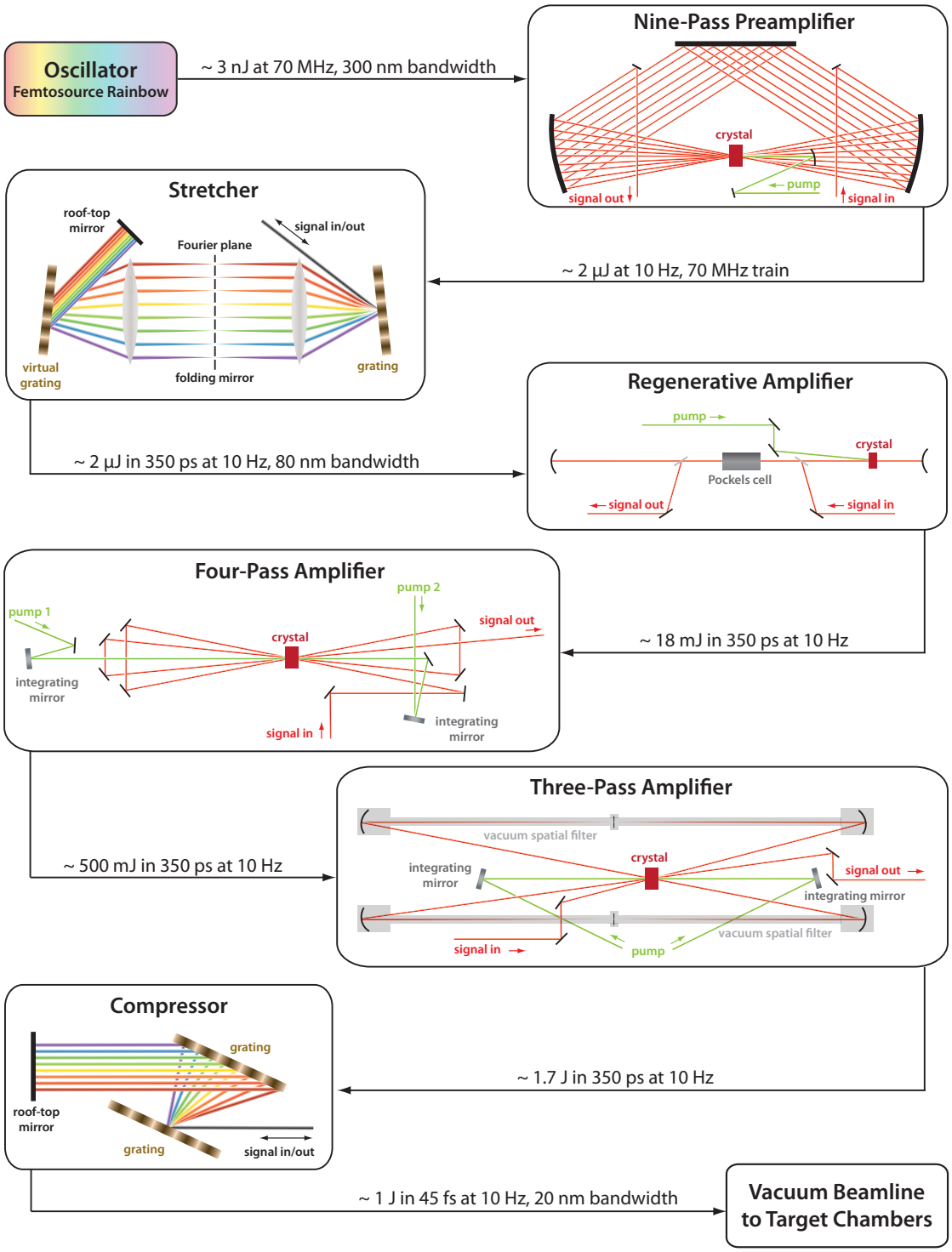

Fig. 3.5. *Flow chart depiction of the ATLAS laser system.*

configuration. According to the concept of CPA (see section 3.1.3), the peak intensity is such sufficiently lowered to allow safe amplification in the following stages. For simplicity, figure 3.5 shows an unfolded stretcher design, whereas in reality only one grating is present, the lens is replaced by a spherical mirror and a folding mirror is situated at the fourier plane. Following a passage through another Faraday isolator to shield the components upstream from potentially hazardous back reflections, a Pockels cell acts as a 10 Hz pulse picker to select those pulses, that have received the highest gain in the preamplifier.

Each pulse is then sent through 12 round-trips in the regenerative amplifier pumped by a 100 mJ, 532 nm Continuum Surelite Nd:YAG laser to be amplified to an energy of $\sim$ 18 mJ. A Pockels cell in combination with two thin film polarizers is used as a switch to couple light in and out of the cavity. Owing to the fact, that only the lowest-order spatial mode of the resonator is efficiently amplified, a clean beam profile exits the cavity. However, the pulses are preceded by a series of prepulses separated by the resonator round-trip time of 11 ns. Those originate from imperfect switching, i.e. leakage of the intra-cavity polarizers. A combination of two Pockels cells with a blocking ratio better than 100:1 each and a respective rise time of 5 ns and 200 ps is implemented after the regenerative amplifier to suppress both the prepulses as well as the ns-timescale ASE background.

Temporal pulse cleaning at later amplification stages becomes much more challenging owing to the increased beam diameter necessary at higher intensity levels. For this reason, the beam passes the final two Ti:sapphire crystals in a multi-pass, i.e. cavity-less, geometry to keep the ASE-pedestal at a minimum. The first, bow-tie-like, amplifier is pumped from both sides by two Continuum Powerlite Nd:YAG lasers at 850 mJ pulse energy each, while in the second multi-pass two beams at 1.7 J each from a Continuum Macholite Nd:YAG laser store energy in the gain medium. To ensure that a smooth beam profile without intensity spikes (often referred to as "hot spots") is maintained, both amplifiers are equipped with segmented integrating mirrors [133] to focus the respective pump beams onto the crystal surfaces and obtain a spatially homogenous pump energy distribution. Additionally, vacuum spatial filters are implemented to clean the beam profile after each passage through the active medium in the second multi-pass. By focussing the beam and placing an aperture in the far field, intensity modulations of high spatial frequencies are thus absorbed. The laser pulse energy is increased to $\sim$ 500 mJ after the first and $\sim$ 1.7 J behind the second and final multi-pass amplifier.

Since an excellent focusability is essential for the highest possible intensities demanded by the experiments presented in this thesis, a nearly flat wavefront needs

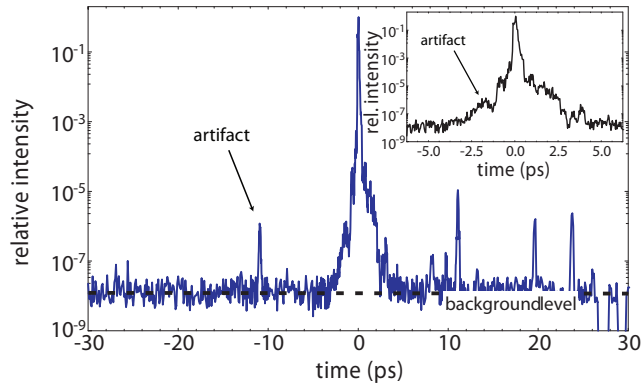

Fig. 3.6. *Third order autocorrelation trace of the ATLAS laser system, where the inset shows a zoomed view of the curve in the region close to the main peak. Both the prepulse at -11 ps and at -2 ps are measurement artifacts and thus of no relevance for the laser pulse contrast. (by courtesy of R. Hörlein, MPQ)*

to be provided. Therefore, the ATLAS system incorporates a Shack-Hartmann sensor to monitor the wavefront of the fully amplified beam. A deformable mirror is connected to the sensor over a feedback loop to significantly lessen wavefront distortions via 33 piezo-actuators [134].

To restore a short pulse duration, the beam is finally guided to a negative dispersion vacuum compressor [135] after being expanded to a diameter of $\sim 70\,\mathrm{mm}$. A set of two parallel orientated 1800 l/mm gold-coated reflection gratings is used to inverse the positive chirp originally introduced by the stretcher, resulting in $\sim 45\,\mathrm{fs}$ pulses of energy $\sim 1\,\mathrm{J}$ exiting the compressor.

Before sending the beam through a vacuum beamline to the target chambers located downstairs, the laser operating parameters are routinely monitored by a set of diagnostics to ensure optimal performance. The pulse duration is characterized by means of a commercial device named GRENOUILLE [136], which is based on the frequency resolved optical gating (FROG) technique [137] to reconstruct the spectral and temporal intensity and phase. To analyze the temporal structure of the pulse in a larger ($> \pm 250\,\mathrm{fs}$) time window, a third order scanning autocorrelator [138] is used. The result of such measurements is shown in figure 3.6, revealing that the intensity level of the ASE-pedestal and short prepulses with respect to the main peak drops below the detection threshold of 10^{-8} already at $-4\,\mathrm{ps}$. Possible deviations of the pulse front from normal to the laser propagation are spotted by an inverted field autocorrelator [139]. Those might arise from imperfect, i.e. non-parallel alignment of the compressor gratings, resulting in an angular chirp of the beam which, amongst other effects, leads to a reduction of the peak intensity in the focus.

2008/2009 ATLAS upgrade

After finishing the MPQ based ion acceleration experiments that are presented in this thesis, the ATLAS laser facility was further upgraded to allow for an even shorter pulse duration and higher energies as well as an increased temporal contrast.

In 2008, a commercially available acousto-optic programmable dispersive filter [140] was added to the system at the stretcher exit. This device named DAZZLER is capable of shaping both spectral phase and amplitude of the laser pulses simultaneously and independently. Thus, e.g. higher orders of dispersion that can not be compensated by the compressor can be corrected for, leading to a decrease in the final pulse duration. By use of the DAZZLER, the ATLAS pulses were successfully shortened to around 35 fs FWHM.

In 2009, a major modification of the laser frontend followed, accompanied by the upscaling of the final multi-pass amplifier. Furthermore, a new and improved 3rd order autocorrelator for day-to-day contrast measurements supplements the set of laser diagnostics. To enhance the contrast of the fully amplified pulse to values around 10^{-12}, a recollimating plasma mirror setup is currently being implemented into the beamline after the vacuum compressor.

3.2.2 The MBI Ti:sapphire System

Owing to the fact that the plasma mirror as well as the aforementioned energy upgrade were not yet available at ATLAS in 2008/early 2009, ion acceleration experiments using nm-scale diamond-like carbon (DLC) foils were not feasible at MPQ at this time. For such targets, an ultrahigh laser pulse contrast is a crucial prerequisite in order to ensure the interaction of the main peak with a near solid density plasma of close to rectangular shape (minimized pre-expansion).

In order to meet such demands, four external experiments of one to seven weeks each were carried out in collaboration with the group of Prof. W. Sandner at Max-Born Institute (MBI) in Berlin. This laboratory hosts a Ti:sapphire laser very similar to the ATLAS system, reaching pulse energies of up to ~ 1.2 J on target at a duration of ~ 45 fs FWHM. A flow chart schematic of the laser's main components is shown in figure 3.7. Pulses of central wavelength 800 nm originating from a Kerr-lens mode-locked commercial Femtolasers Femtosource Scientific s20 oscillator are elongated to ~ 700 fs by an Offner-type stretcher and subsequently amplified in three consecutive multi-pass stages. In contrast to ATLAS, no regenerative amplifier is implemented in the system. Thus, the generation of prepulses due to cavity leakage as described earlier in section 3.2.1 is avoided and the amount of ASE is

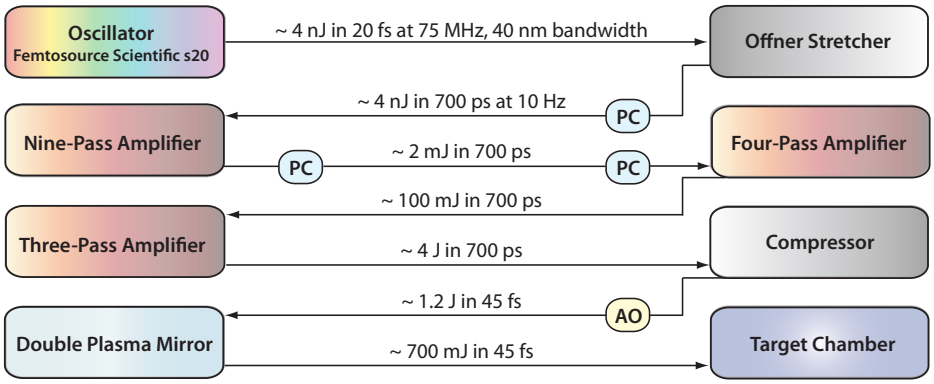

Fig. 3.7. *Schematic flow chart depiction of the high-power Ti:sapphire laser system located at MBI Berlin (PC = Pockels Cell, AO = Adaptive Optic).*

reduced. However, a ns-duration ASE-pedestal is still present. This unwanted pulse background primarily stems from the first amplifier, owing to the high gain of approximately six orders of magnitude. Consequently, following the nine-pass amplifier the beam traverses two Pockels Cells , one with a fast rise time, to shrink the ASE-level. After further amplification to $\sim 4\,\mathrm{J}$, the pulses are compressed and sent to the interaction chamber, resulting in up to $\sim 1.2\,\mathrm{J}$ on target stored in a FWHM duration of $\sim 45\,\mathrm{fs}$. The final contrast was characterized by means of a 3rd order autocorrelator to be smaller than 10^{-7} at times earlier than $-10\,\mathrm{ps}$ prior to the arrival of the main peak (see figure 3.8a), mainly depending on the first amplifier gain and the timing of the subsequent Pockels Cells. In order to correct for wavefront distortions and therefore assure a good focusability of the beam, an adaptive mirror similar to the one at ATLAS is included behind the compressor.

To increase the ps-timescale contrast to an estimated level of $\sim 10^{-11}$, a recollimating double plasma mirror setup is installed in the beamline before entering the target chamber. In general, a plasma mirror operates as an ultra-fast switch, where the low-intensity non-ionizing ASE-pedestal and prepulses are transmitted and the main pulse is largely reflected by the plasma created on its own rising edge [141, 142]. A schematic illustration of the specific system used at MBI [143] is given in figure 3.8b. Here, the beam is focussed by a 10° off-axis parabola of focal length 1.5 m to a spot size of $\sim 50\mu\mathrm{m}$. Two AR-coated rectangular glass blocks are placed at 45° angle of incidence each, the laser beam is s-polarized with the laser focus located in-between the substrates. The relative distances of the plasma mirror surfaces to the focus and respective intensities are $\sim -10\,\mathrm{mm}$ at $\sim 1\times10^{16}\,\mathrm{W/cm^2}$ and $\sim 3\,\mathrm{mm}$ at $\sim 6\times10^{16}\,\mathrm{W/cm^2}$. Both plates are motorized to shift the setup so that the laser can hit an unperturbed area again after an interaction, thus allowing for a series of 25

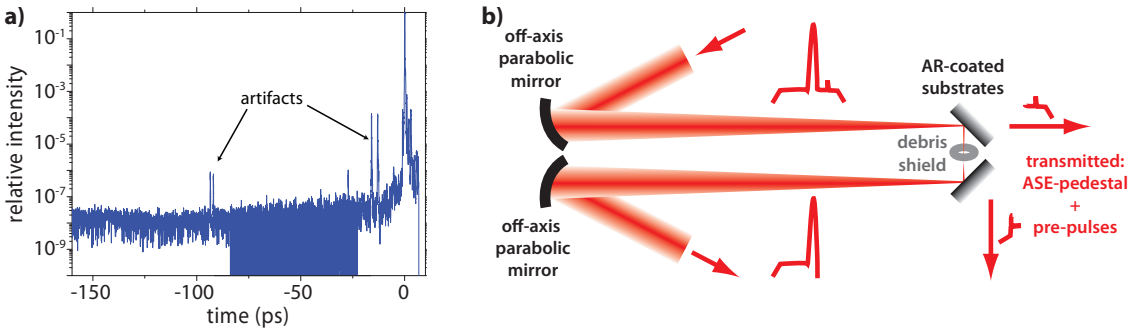

Fig. 3.8. *(a) Third order autocorrelation trace of the MBI Ti:sapphire laser and (b) a schematic of the recollimating double plasma mirror used in combination with the system in order to enhance the pulse contrast on target. (autocorrelation trace by courtesy of T. Sokollik, MBI Berlin)*

consecutive shots before the chamber has to be vented to replace the substrates. A ceramic disk with a central hole is placed between the plates to shield each surface from large-scale debris which originates from the expanding plasma. For alignment purposes employing attenuated, non-ionizing pulses, a small part of each substrate is left uncoated. Finally, the beam is recollimated by a second off-axis parabola of equal focal length and sent to the target chamber. The total energy throughput of the double plasma mirror setup was measured to be 60 %, resulting in ultra-high contrast pulses of energy $\sim 700\,\mathrm{mJ}$ on target.

In case no contrast enhancement is required, the setup can be bypassed using two motorized mirrors located before the first and after the second parabola.

3.2.3 The TRIDENT Laser Facility

To extend the range of laser parameters available for ion acceleration studies to significantly higher pulse energies of up to 100 J, a series of experimental campaigns was carried out at the TRIDENT laser facility located at Los Alamos National Laboratory in the US [144]. TRIDENT is a three-beam system that is based on Nd:glass (see table 3.1) as gain medium for the main amplifiers. Two target chambers are currently operational with a third one of increased size that is specifically designed for short-pulse experiments to become available in 2010. The laser system is capable of producing energetic pulses of central wavelength 1053 nm that can be varied in duration over a huge range of around seven orders of magnitude, spanning from $5\,\mu$s all the way down to about 500 fs. In the south target chamber mostly material dynamics experiments are conducted, such as laser-launched flyer plates and laser-ablation shock loading [145], making use of the long pulse ($>$ 80 ps), high energy (up to 1 kJ) "A", "B" and "C" beams that can be employed simultaneously. However,

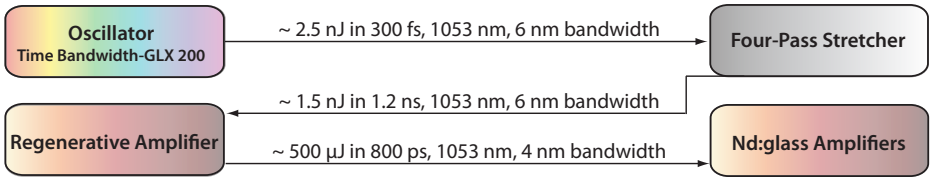

Fig. 3.9. *Basic setup of the type 0 TRIDENT laser front end as used in the first ion acceleration campaign employing plasma mirrors.*

Fig. 3.10. *Flow chart depiction of the revised, type 1 TRIDENT front end. The new approach relies on self-pumped optical parametric amplification (SPOPA) to generate idler pulses that are virtually background free. Those high contrast pulses are further amplified in a series of OPA stages before being sent to the Nd:glass chain.*

the highest power of up to 200 TW is generated in the TRIDENT "C" beam in short pulse mode and guided to the north target chamber which is of spherical shape at a diameter of $\sim$ 2 m. In this configuration, temporally stretched pulses originating from the TRIDENT short pulse front end are further amplified to energies of ~ 5 J in 16×64 mm Nd:glass rods and gain their final energy of up to 200 J after passing a series of 40×100 mm Nd:glass disks. A deformable mirror is placed in the amplification chain to correct for wavefront distortions. Subsequently, such pulses are compressed down to a duration of $700 - 500$ fs in a ~ 20 cm diameter beam by a pair of $40 \times 80\,\mathrm{cm}^2$ dielectric gratings located in vacuum. The compressor output energy amounts to values slightly above 100 J. A focal spot of diameter $10\,\mu$m FWHM is obtained after reflection off a f/3.5 off-axis parabolic mirror, giving rise to peak intensities in excess of $10^{20}\,\mathrm{W/cm}^2$. Owing to the enormous thermal load on the gain material of the main amplifiers and the low heat conductance of Nd:glass, the repetition rate of the laser is however limited to $\sim 1/\mathrm{h}$ for full system shots.

Experiments carried out at TRIDENT within the framework of this thesis were

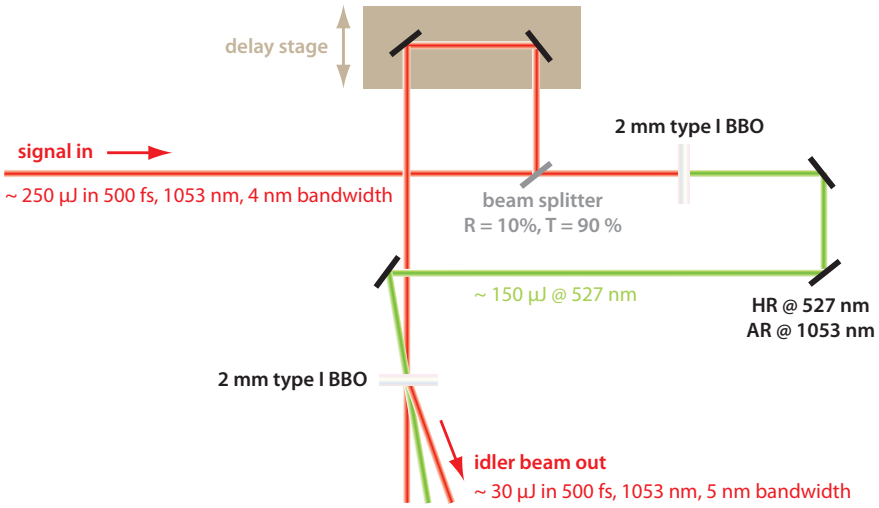

Fig. 3.11. *Self-pumped OPA stage as implemented in type 1 of the TRIDENT front end. In the seed-pump photon-photon interaction, an idler beam of nearly perfect temporal contrast is generated which is used for further amplification.*

primarily aiming for ion beams accelerated from diamond-like carbon (DLC) foils of only a few nanometers in thickness (see chapter 6). To ensure interaction of the main laser pulse with a nearly unperturbed, ideally rectangular shaped plasma slab, the amplified spontaneous emission (ASE)-pedestal as well as pulses preceding the main peak needed to be suppressed to a sufficiently low level. In a first campaign launched in spring 2008, this prerequisite was achieved by introducing a pair of plasma mirrors into the converging beam after the focussing off-axis parabola. A more detailed description of that setup is included in chapter 6. The use of plasma mirrors is nevertheless unfavorable due to losses of about $40-50\%$ of the laser pulse energy on a double reflection. Moreover, the plasma mirror substrates set up in the configuration presented in chapter 6 needed to be replaced after every shot.

To overcome this quandary by improving the intrinsic contrast of the TRIDENT system, the old short pulse front end (type 0, figure 3.9) was upgraded to an approach based on optical parametric amplification (OPA) [146]. For an introduction to the basic principles of OPA refer to section 3.1.4, more details can be found in chapter 8 which is devoted to laser development. The new TRIDENT front end setup is schematically depicted in figure 3.10. It builds upon the previous version, where 300 fs short pulses of energy 2.5 nJ originating from a Time Bandwidth GLX-200 diode pumped glass oscillator are elongated to 1.2 ns in a four-pass grating stretcher and subsequently amplified to 500 μJ by a Positive Light Legend regenerative amplifier based on Ti:sapphire. Those pulses are then again compressed by a pair of

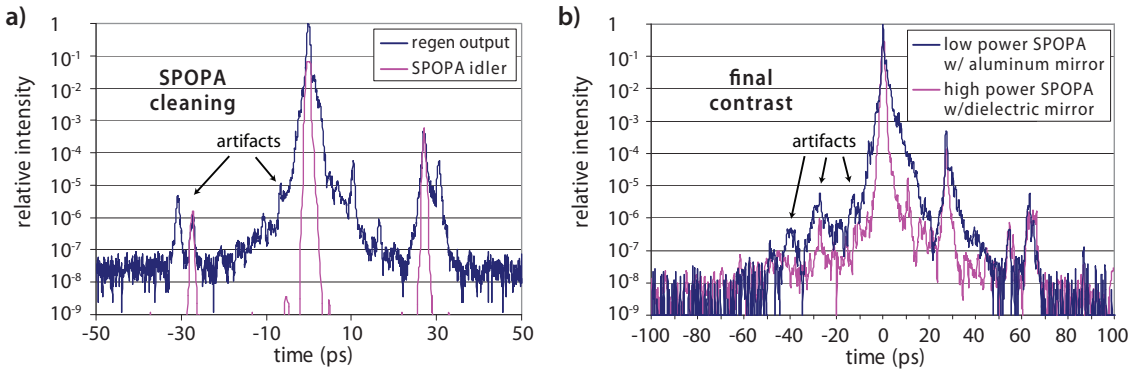

Fig. 3.12. *Third order cross correlator measurements of the TRIDENT laser pulse contrast. Negative values on the abscissa refer to times prior to the arrival of the main peak centered around zero. The apparent subsidiary peaks are all artifacts from the measurement system. In (a), the blue curve corresponds to the output of the regenerative amplifier, i.e., front end type 0, whereas the magenta colored graph gives the contrast of the idler generated in front end type I. The final contrast of this configuration upon further propagation through the laser chain is marked in blue in (b). Here, the magenta line shows improvements when the SPOPA cleaning stage is moved behind the OPA amplifiers and a mirror in the stretcher is replaced. (by courtesy of R. P. Johnson, Los Alamos National Laboratory)*

gratings to a duration of 500 fs and sent to an OPA stage illustrated in figure 3.11. Here, each pulse is split into two replicas by a 90-10 beamsplitter, with the higher energetic one being frequency doubled to yield 150 μJ at 527 nm. The two beams are recombined on a 2 mm thick type I beta barium borate (BBO) crystal at a small non-collinear angle. In the resulting OPA process, an idler pulse is generated which is then used for further amplification in three consecutive BBO based OPA amplifiers pumped by one Continuum Powerlite Nd:YAG laser of $\sim$ 2 J energy at 532 nm wavelength.

The effect of SPOPA cleaning was characterized by means of a commercial (Del Mar) third order cross correlator with the measurement result being illustrated in figure 3.12a. The apparent peaks in the autocorrelation traces are all artifacts of the measurement system. It is immediately striking, that the idler generated by SPOPA (figure 3.12a, magenta colored) is practically background-free and provides a significant improvement over the output of the regenerative amplifier (marked in blue), i.e., TRIDENT front end type 0, which seeds the SPOPA stage. However, it turns out that the contrast changes quite remarkably upon further propagation through the system. Figure 3.12b presents 3rd order autocorrelator measurements carried out after the final parabolic focussing mirror and a re-collimating lens inserted into the target chamber. Here, the blue curve in figure 3.12b corresponds to the SPOPA idler of figure 3.12a or, in other words, illustrates the final contrast of

front end type I. Two contributions could be identified for the apparent decline in the pulse contrast. One arises from the following OPA stages that are seeded at low energies of $\sim 20\mu$J and the other from the mirror placed in the Fourier plane of the focussing element in the Martinez-type stretcher, where the beam is fully dispersed over the mirror surface. Spatial variations in the reflectivity of the mirror will therefore translate to spectral modulations of the beam. By shifting the SPOPA idler generation cleaning stage behind the OPA amplifiers and replacing the aluminum mirror in the stretcher with a dielectric one, an improvement of around one order of magnitude in the final contrast could be achieved (figure 3.12b, magenta curve), though that setup was not yet available for the experiments discussed within the framework of this thesis. Regarding figure 3.12b, it has to be noted that the characterization of the final contrast could not be done on a full system shot at present. Instead, the low power pulses originating from the front end were guided through the non-pumped main Nd:glass amplifiers. Consequently, the question on how the laser pulse contrast looks like on an actual shot is not finally solved as the contrast might be affected when the pulse gets amplified. Here, effects such as spectral gain narrowing and self phase modulation due to intensity dependent changes in the refractive index of optics are of most concern.

In fall 2008, the new, OPA-based type I front end was first-time employed for an experimental campaign (see chapter 6, section 6.5).

3.2.4 The VULCAN Laser Facility

The VULCAN laser is part of the Central Laser Facility (CLF) at the Rutherford Appleton Laboratory (RAL), Oxfordshire, UK. As TRIDENT, it is a large-scale, high energy, low repetition rate Nd:glass system. VULCAN features three different target areas, Target Area East (TAE), Target Area West (TAW) and Target Area Petawatt (TAP). Three experimental campaigns were carried out at VULCAN as a part of my PhD work, one of them at TAW and two at TAP, those will be described briefly in the following.

Target Area West (TAW)

TAW comprises a 100 TW beam line, delivering 100 J of energy stored in pulses of 1 ps FWHM duration. In addition, up to 6 long pulse beams of 200 J in 1 ns each are available. The 100 TW pulses originate from a Ti:sapphire based Kerr lens mode locked TSUNAMI oscillator pumped by an Argon ion laser. 5 nJ in 120 fs are obtained and subsequently elongated to 600 ps in a double pass grating stretcher.

The pulses of central wavelength 1053 nm at a bandwidth of 16 nm are then amplified in a series of flashlamp pumped Nd:glass rods before reaching the final, single pass Nd:glass disk amplifier stage of 150 mm aperture. Recompression to 1 ps is achieved by guiding the beam in a single pass over a pair of gold-coated gratings that are separated by $\sim$ 3.5 m. Peak intensities of $\sim 5 \times 10^{19}\,\mathrm{W/cm^2}$ can be reached after reflection off a parabolic focussing mirror.

Target Area Petawatt (TAP)

The Vulcan Petawatt upgrade became available to users in 2002, being designed to deliver 500 J on target within a duration of 500 fs and peak intensities up to $10^{21}\,\mathrm{W/cm^2}$ [147, 148], a value which represented the world record at that time. Pulses of 5 nJ and 120 fs duration are again formed by a commercial Ti:sapphire oscillator at a central wavelength 1053 nm, being stretched to 2.4 ns. The beam is further amplified in three OPCPA stages employing BBO crystals that are pumped by a single Nd:YAG laser of energy 1 J at a wavelength of 532 nm, a setup very similar to the type 1 TRIDENT front end but without SPOPA cleaning. A chain of neodymium doped phosphate and neodymium doped silicate glass rod amplifiers follows. Using such mixed glasses enables amplification to take place over a broader spectral range. To improve the wavefront quality, a 120 mm diameter large aperture adaptive optic is included in the system, composed of a deformable mirror of 61 actuators in a 2D array [149]. The final three 208 mm disk amplifiers, being set up after a Faraday rotator and a polarizer, are a relict from the decommissioned NOVA laser formerly located at Lawrence Livermore National Laboratory (LLNL). Upon further propagation, the beam of 5 nm bandwidth is expanded to 600 mm diameter via a 19 m long vacuum spatial filter and guided to the compressor. Gold-coated, 1480 l/mm gratings are set up in single pass geometry at a separation of 13 m. Two mirrors steer the beam onto the final 620 mm diameter, 1.8 m focal length, f/3 off-axis parabolic mirror, where beam diagnostics such as spectrum and near field monitor as well as pulse duration via a single-shot autocorrelator [150] collect the transmitted light of the first turning mirror. A focal spot of $\sim 5 - 7\,\mu$m FWHM diameter is obtained, giving an optimum peak intensity close to $10^{21}\,\mathrm{W/cm^2}$.

When compared to TRIDENT, the VULCAN PW system delivers a significantly higher level of ASE background and subsidiary pulses preceding the main peak. The ASE pedestal arrives at $\sim$ 2 ns prior to the main pulse and was characterized to be of relative intensity $\sim 4 \times 10^{-8}$ [151]. However, autocorrelation measurements on a shorter timescale reveal a contrast of only $\sim 10^{-3} - 10^{-4}$ at a time around 20 ps

[152], whereas TRIDENT gives a ratio of $\sim 10^{-6} - 10^{-7}$ in this range (see figure 3.12).

A variety of different phenomena were investigated during the named three experimental campaigns. Those include for instance electron transport and filamentation in solid density targets [66] and radiation-driven acceleration and instabilities of expanding, nm-thin foils [153]. The analysis of the obtained data is however partly ongoing and the obtained results are not included in this thesis.

Chapter 4

Experimental Methods II - Targets and Ion Beam Diagnostics

4.1 Target Fabrication and Characterization

The experiments presented in this thesis focus on ion acceleration from two different, novel target systems, namely synthetic microspheres of diameter $\sim 15\,\mu$m and nm-thin diamond-like carbon (DLC) foils. Within the framework of this dissertation, a target fabrication facility was set up and the techniques were developed to be capable of producing such targets. In the following, the methods utilized for target fabrication and characterization will be presented.

4.1.1 Microspheres

To study ion acceleration from spherical, ideally isolated, mass-limited targets, in a first step a suitable mount needs to be engineered in order to support the microspheres while minimizing contact area and electric conductivity. Those requirements are fulfilled by micropipettes produced from glass tubing. Manufacture of micropipettes was done employing a microprocessor controlled, CO_2 laser-based micropipette puller (P-2000, Sutter Instrument Company). Here, the CO_2 laser beam of tunable output power is guided to the central part of the glass tube and projected onto its back face via a scanning mirror which is mounted on a rotating base driven by a stepper motor. Heat is applied to the glass by an automated, repeated scan of the mirror between the limits of a longitudinal area that is predefined in length (1 mm - 8 mm) by the user. The transmitted portion of the beam is collected by a retro-reflective concave mirror mounted behind the tubing, redirecting the divergent

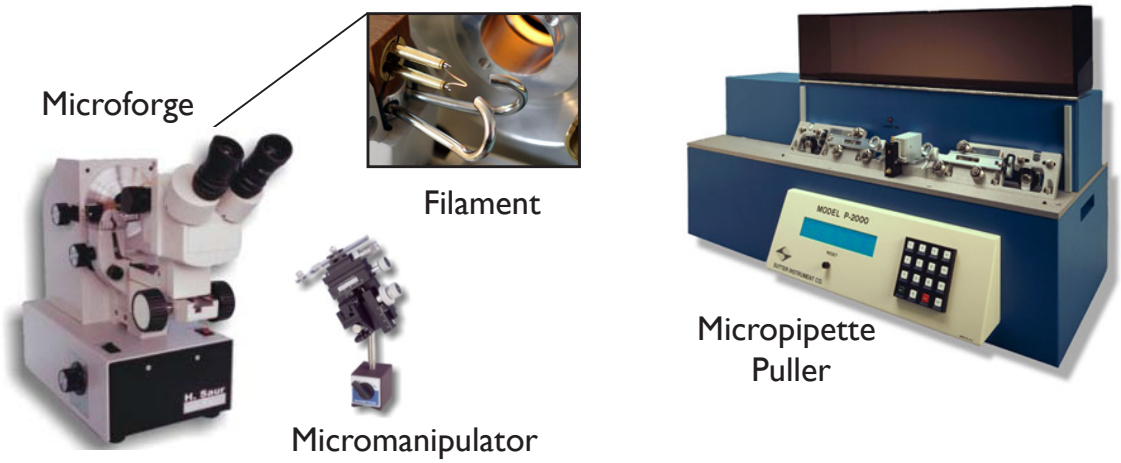

Fig. 4.1. *Illustration of the key equipment employed for the fabrication of microsphere targets. A CO_2 laser based micropipette puller is used to produce glass mounts of sub-micron diameter. The microforge enables the manufacture of microspheres of diameters ranging from a few to several tens of micrometers that are securely attached to the tip of the micropipette.*

laser onto the front side of the glass. Thus, a uniform heating around the circumference of the tube is ensured. The capillary is mounted in a carriage system that begins to pull apart under a constant load as the glass softens until a destined trip point in the increasing velocity is reached. At this moment, the heat delivered by the laser is turned off. Now, the hard pull phase sets in, which finally separates the centrally melted tube in two micropipettes of equal kind. By adjusting the delay of the hard pull activation with respect to the time when the heat is turned off, the length of the resulting taper as well as the tip diameter can be controlled. The higher the delay, the cooler the glass will be, leading to shorter tapers and larger tips. At optimized pulling cycle parameters, tip diameters as low as 30 nm can be achieved. While conventional pullers rely on filaments as a heat source, the primary advantage of employing a CO_2 laser for melting as described is the ability to work with quartz (fused silica) glass. Quartz is stronger and exhibits a significantly higher softening temperature than standard glass capillary tubing (such as borosilicate glass), making it highly suitable for the desired use as target mount.

For further processing including the final step of affixing a microsphere of designated diameter to the tip of the capillary, a microforge (deFonbrune F-1000 series) is employed. The complete target manufacturing setup is illustrated in figure 4.1. The microforge consists of an optical-electrical forge system that is comprised of a horizontal microscope of 40× magnification combined with a fine adjustment, V-shaped, round-wire, platinum-iridium filament and a workpiece holder. Heat of the filament is controlled by adjusting the current to the electrode. Additionally, two

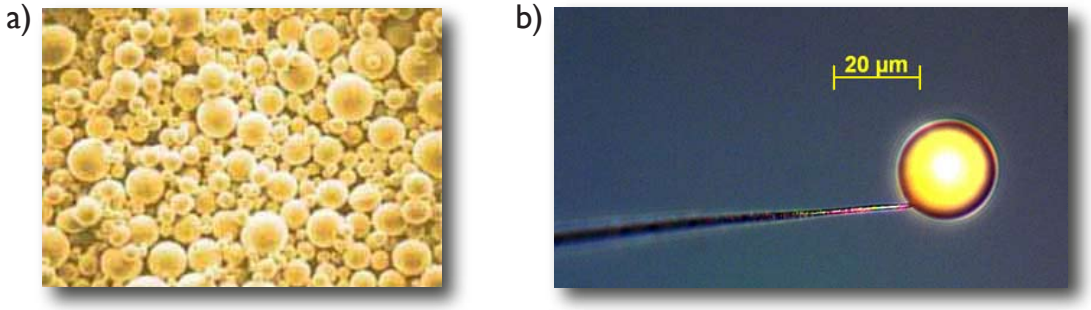

Fig. 4.2. *(a) Spherical gold powder of average diameter* $\sim 6\,\mu m$ *as base material for the manufacture of mounted microsphere targets. In (b), an exemplary image of a mounted gold sphere of diameter* $\sim 23\,\mu m$ *is shown, that has been fabricated by fusing several microparticles together following the procedure described in the text.*

curved air jets converging on the wire heating filament can be used for ventilation, providing "spot" cooling of the heated element. An illumination source is placed in the back of the filament and the vise assembly used to position and maneuver the component to process. To manufacture a mounted microsphere target, a pulled glass micropipette is clamped into the vise. A second, carrier capillary is dipped into the powderous raw material that will form the desired target compound and attached to a micromanipulator stage. The utilized base material is commercially available microspherical powder (either dry or in aqueous suspension). Mostly, poly(methyl methacrylate) (PMMA), gold and copper microparticles of several microns diameter were used (by AlfaAesar, microParticles GmbH). After being immersed in the powder, the carrier capillary is covered by a large number of these microparticles sticking to the glass surface. Employing the micromanipulator and the movement controls of the vise, the tip of the pulled micropipette is used to carefully pick up one or several of the microparticles from the carrier capillary. At this stage, the bond of the microparticle and the micropipette tip is purely formed by adhesion. To ensure a secure and stable join, the micropipette tip is positioned in close vicinity to the heated filament. Given the right adjustment of the filament temperature and the air ventilation, the target compound will melt and minimize its surface tension, ideally forming a perfect sphere of flush facing that is connected to the tip of the micropipette. Here, the use of micropipettes made of fused silica instead of borosilicate glass is highly beneficial to avoid unwanted melting of the capillary tip. Repeating this procedure, the target size can be increased by fusing several microparticles together to a single sphere. An exemplary image of a mounted gold microsphere crafted in the described way is shown in figure 4.2.

4.1.2 Ultra-Thin Diamond-Like Carbon (DLC) Foils

Prior to the work presented in this thesis, only a few experiments have been carried out to investigate ion acceleration from free-standing foil targets of thicknesses significantly below 1 micron. In those previous studies, Aluminum (Al), Silicon Nitride (SiN) or Mylar (boPET) foils were used, being limited in thickness to lowest values of several tens of nanometers [154–156]. Moreover, such targets appear highly fragile, imposing difficulties in day-to-day handling. In order to overcome those issues, a different material being novel to the laser-driven ion acceleration community has been established as ultra-thin film target compound, namely diamond-like carbon (DLC).

Properties of DLC

Carbon in its crystalline form mainly occurs in two different chemical bond configurations. In graphite, sp^2-hybridized carbon atoms form high-strength planes of hexagonally orientated, covalent bonds. Such layers are only loosely connected by Van-der-Waals forces, giving graphite its softness. This is in contrast to the case of diamond, where sp^3-hybridized carbon atoms are bonded covalently in tetrahedral geometry, building a three-dimensional network which gives rise to the outstanding hardness of the material. While graphite appears opaque and is a conductor owing to one delocalized outer electron, the highly thermally conductive diamond is an electric insulator with a large bandgap of 5.45 eV which is widely optically transparent.

DLC is a quasi-amorphous allotrope of carbon, being composed of a combination of graphite and diamond bonds, thus possessing intermediate properties. It is widely used in industry in various applications, mostly as a protective coating. By introducing a significant number of sp^3-bonds in the matrix, diamond-like characteristics can be achieved. Compared to the above mentioned other compounds available for the fabrication of nm-scale foils, the optically highly transparent DLC foils offer an exceptionally high tensile strength, hardness and heat resistance, making DLC a perfectly suitable material for mechanically stable, ultrathin, self-supporting targets.

Fabrication of Ultra-Thin DLC Targets

There are several different approaches for the production of nm-scale, free-standing DLC foils. In the following, the two techniques utilized to produce the targets for the ion acceleration experiments presented in this thesis (see chapters 6 and 7) will

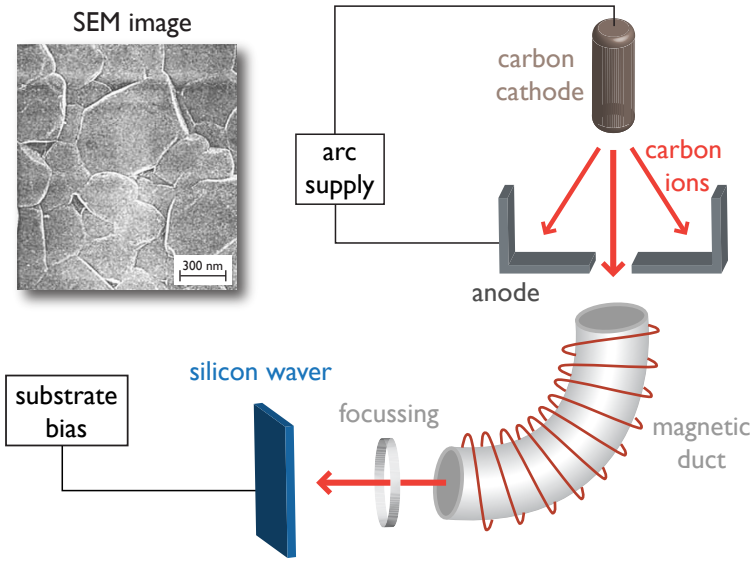

Fig. 4.3. *Simplified illustration of the basic configuration utilized in cathodic arc deposition of ultrathin diamond-like carbon foils. Additionally, an exemplary scanning electron microscope (SEM) image of the resulting DLC-film surface is presented.*

be addressed briefly.

The first set of DLC foils used in the leadoff campaign at Los Alamos National Laboratory (chapter 6) has been produced by Vitaly Liechtenstein and coworkers at the Russian Research Center (RRC), Kurchatov Institute in Moscow. Here, DLC foils were generated by DC glow discharge sputtering of carbon in a low-density krypton plasma [157–162]. The discharge voltage is 4 kV at a current of 4 mA and the energy of deposited particles amounts to about 50 eV. Neutral carbon atoms condense onto glass slides which are placed outside the zone of ion fluxes and cooled to liquid nitrogen temperature. Growth rates of the DLC film are in the range of $0.5 - 0.8$ nm/min, with the final foil thickness being controlled by the time the substrate remains in the discharge. The substrates are coated with a parting agent (such as rock salt, betaine or potassium oleate), so that the DLC film can be released by floating in distilled water. Employing this technique, self-supporting $10 - 50$ nm thick DLC foils of density 2.2 g/cm^3 composed of 50% sp^3, i.e., diamond-like, bonds have been fabricated.

In order to further increase the fraction of diamond-like carbon bonds in the DLC film, a different target production setup was established in our group. This approach relies on cathodic arc deposition [163]. A simplified illustration of the basic scheme is presented in figure 4.3. The cathodic arc is a low-voltage, high current plasma discharge that is used to vaporize material from a cathode target which is in our case

made of carbon. The arc is not homogeneously distributed over the cathode, but is instead concentrated at a small number of discrete sites of estimated size $1 - 10\,\mu$m referred to as cathode spots, moving across the cathode surface. In a similar manner to the blow-off plasma seen when focussing an intense laser onto a solid surface, the generated plasma plumes away from the cathode owing to the high plasma pressure within the cathode spot, initially propagating normal to the cathode surface. For typical arc currents in the several hundred amperes range, the plasma ion current is a constant fraction of $(10 \pm 2)\,\%$ of the arc current. Alongside with the intense plasma flux, macroparticles of diameter $0.1 - 10\,\mu$m are ejected from the cathode, constituting a significant amount of unwanted debris as well as an additional source of cathode mass consumption. Those macroparticles need to be removed from the plasma stream before reaching the substrate. Filtering is achieved by the use of curved magnetic guide fields, in our case a quarter-torus [164]. While the plasma is transported through the 90° duct with an efficiency of up to 25 %, macroparticles are not magnetically guided and are lost. The highly directed carbon ion drift energy amounts to about 30 eV, providing a kind of pseudo-temperature to the growing film. Thus, surface atoms exhibit some mobility which improves the quality of the coating. Control of the ion energy is done by introducing a substrate bias [165]. By means of this straightforward approach both the microhardness as well as the unwanted internal compressive stress leading to limitations in the achievable target thickness can be regulated. Given optimum conditions, hydrogen-free DLC films of up to 85 % sp^3 content are formed.

Employing the cathodic arc deposition technique, our group succeeded in producing DLC foils of $\sim 75\,\%$ sp^3 content and $2.7\,g/cm^3$ density, coming close to the density of pure crystalline diamond of $\sim 3.5\,g/cm^3$. The DLC films of thickness $2.5 - 58\,$nm are coated onto a silicon waver substrate covered with a release agent and are subsequently floated in distilled water as described above. Finally, the targets are mounted on steel frames, revealing a high stability while being free-standing over a diameter of 1 mm.

Characterization

For the purpose of using DLC films as targets in laser-plasma interaction experiments, the following characteristics of the foils are of prime interest:

- Thickness
- Surface structure

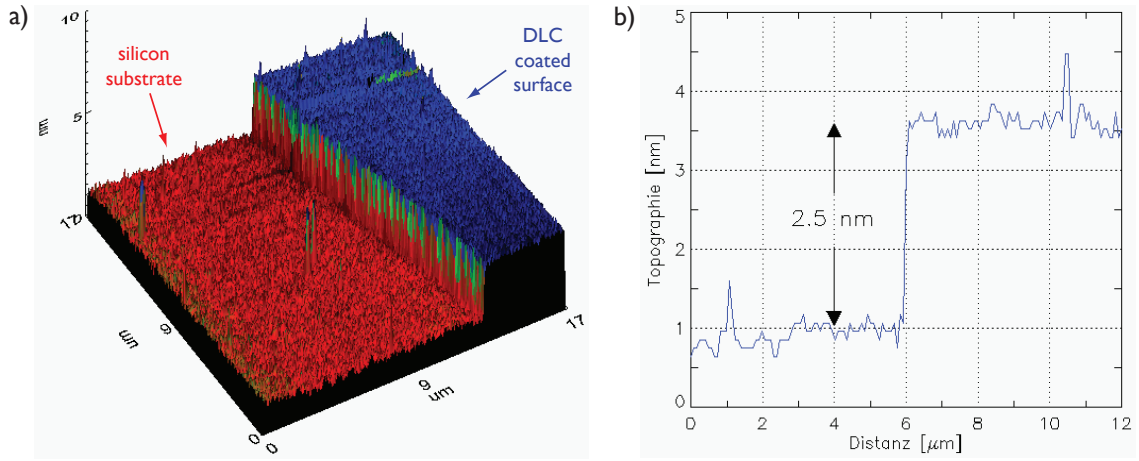

Fig. 4.4. *(a) Zoomed view of the edge separating the DLC film area from the uncoated silicon surface of the reference wafer as obtained by measurements using an atomic force microscope (AFM) in non-contact mode. The corresponding topography line out of this exemplary case is presented in (b), giving a step height of 2.5 nm.*

- Depth-dependend composition

Determination of the foil thickness can be done in a variety of ways, including profilometry, ellipsometry, weighing, etc. For highly precise measurements of the DLC film thickness as well as surface structure analysis, a commercial profilometer equipped with an atomic force microscope (AFM) sensor (MicroProf, FRT Fries Research & Technology) was used in the framework of this thesis. The AFM scans the sample line by line with a very sharp silicon tip of nm-scale radius of curvature situated at the end of a microscale cantilever. Forces between tip and sample lead to a deflection of the cantilever, which is detected by a fiber-based laser interferometer. The modes of operation include a contact mode, where the static tip displacement is recorded and a non-contact mode, where the cantilever is externally driven near its resonance frequency. Here, damping of the cantilever oscillation which depends on the distance to the sample is utilized as a feedback signal. When compared to the contact mode where a small bearing strength might affect the sample surface, this potential influence is excluded in non-contact operation. The FRT AFM provides a lateral range of $40\,\mu\text{m} \times 40\,\mu\text{m}$. Characterization of the DLC film thickness was done by drawing a marker line onto reference silicon wafers before placing them next to the actual substrate in the carbon deposition process. Subsequently, the marker line is erased from the reference wafer by use of acetone, resulting in a clean, uncoated silicon surface separated from the DLC coated area by a sharp step, which defines the thickness of the fabricated DLC film. A typical AFM image of the step

height of the DLC film with respect to the uncoated wafer surface is shown in figure 4.4. Despite the sub-nm precision of the AFM instrument, in some cases much larger uncertainties remain for the actual DLC target thickness of a specific shot in an experiment. This is mainly due to the sizable inhomogeneities in thickness which can occur over distances of several centimeters in the described cathodic arc deposition setup, a problem that will be minimized upon further improvement of the system.

In addition to the AFM, a scanning electron microscope (SEM) was employed for analysis of the DLC film surface structure. An exemplary image obtained from a SEM measurement is presented in figure 4.3. Structural elements of size $\sim 100\,\mathrm{nm}$ are visible, staying significantly below the laser focal spot diameter of several microns.

Precise characterization of the DLC bulk compound as well as determination of the thickness and composition of the contamination layer formed by impure vacuum conditions during deposition was carried out by means of elastic recoil detection analysis (ERDA) [166]. ERDA exhibits similarities to Rutherford backscattering (RBS) with light energetic ions ($0.5 - 3\,\mathrm{MeV/u}$), a method that has been proven highly useful for the analysis of heavy elements in thin films for more than three decades. RBS is based on the energy loss of a primary, backscattered particle after an elastic collision with a target atom. Owing to the precise knowledge of Rutherford scattering cross sections, quantitative data on the depth dependent abundance of sample elements can be extracted. However, the detection of light atoms that are embedded in a matrix of heavier elements is restricted, due to ambiguities arising from the sole measurement of the backscattered particle energy. Moreover, hydrogen can not be detected at all, since backscattering from this element is not possible.

In contrast to RBS, ERDA typically employs an energetic *heavy* ion beam to be directed at the sample. The incident ions interact elastically with the film atoms and are of sufficient energy to kick out, i.e., recoil, atoms they are scattered off (see figure 4.5a for a schematic of the setup). Instead of detecting the energy of a backscattered ion, both the energy and the mass of the recoiled atom are determined in separate measurements. Consequently, the sample element species can be identified directly and a quantitative depth profile without ambiguities is obtained.

Characterization of the DLC films is done at the Munich tandem accelerator providing a high energy heavy ion beam ($0.5 - 1\,\mathrm{MeV/u}$ ^{58}Ni, ^{127}I or ^{197}Au) [167–169]. Recoiled ions are characterized in a solid angle of 5 msr with a total energy resolution as high as 7×10^{-4} using the Munich Q3D magnetic spectrograph [170]. Owing to the large acceptance angle, a measurement with single atomic layer depth

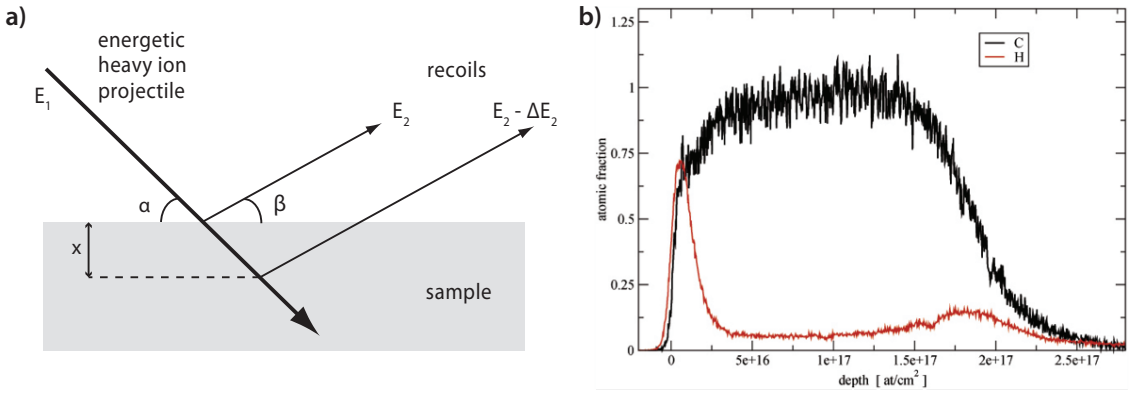

Fig. 4.5. *(a) Schematic of the basic ERDA setup. A high energetic heavy ion beam (in our case* $0.5 - 1\,MeV/u$ ^{58}Ni, ^{127}I *or* ^{197}Au *from the Munich tandem accelerator) is directed at the sample (e.g. a thin DLC film). The depth-dependend energy of recoiled particles together with an additional measurement of their respective mass allows for the determination of a depth profile of the target compound that is exemplarily presented in (b) for a 10 nm DLC film deposited on a silicon wafer substrate. Here, the black curve corresponds to carbon atoms, while the hydrogen abundance is marked in red, showing clear evidence of a hydrocarbon contamination layer of thickness* $\sim 1\,nm$ *on the DLC front surface.*

resolution can be obtained before the depth profile is altered by radiation damage. A resulting depth profile of a 10 nm thin DLC film deposited on a silicon wafer substrate is presented in figure 4.5b. The hydrocarbon contamination layer is clearly visible on the DLC front surface and is identified to be of thickness $\sim 1\,nm$.

4.2 Ion Beam Diagnostics

This section is devoted to the description of experimental techniques used to characterize the accelerated ion beam. In the first part, a brief introduction to different ion detectors will be given, whereas the corresponding measuring instruments will be presented in the second part.

4.2.1 Detectors

CR39

CR39 (i.e., Columbia Resin #39), or polyallyl diglycol carbonate, is a plastic polymer of chemical formula $C_{12}H_{18}O_7$. It is transparent in the visible spectrum and has a density of about $1.30\,g/cm^3$. Since the 1980s, CR39 has been widely used as a solid state nuclear track detector. When compared to other ion detectors commonly employed in laser-driven particle acceleration that will be described in the follow-

ing, CR39 offers a main advantage in its insensitivity to photons and electrons. The films are mostly manufactured as rigid slides of 1 mm thickness, but thinner slices down to $\sim 150\,\mu$m are also available and have been used to characterize ion beams originating from laser-irradiated microspheres (see chapter 5). For the experiments presented in this thesis, a form of CR39 named TASTRAK, produced by Track Analysis Systems Ltd., Bristol, UK was utilized.

Incident ions of energy above a detection threshold of about 100 keV/nucleon are recorded by the latent tracks left in the material that become manifest in the form of broken molecular bonds. There are two mechanisms responsible for the total energy loss dE/dx of a projectile ion. Those are namely the electronic energy loss (EEL) via inelastic collisions with target electrons and the nuclear energy loss (NEL) via elastic collisions with target nuclei. For protons in the several MeV energy range (as obtained in laser-plasma acceleration experiments) incident on CR39, the electron energy loss is predominant over the nuclear energy loss by about three orders of magnitude. The total energy loss of the incident particle or stopping power of the material can be calculated by the Bethe-Bloch formula [171].

After ion beam irradiation, the latent tracks in CR39 are revealed by virtue of etching in a caustic alkaline solution, for the presented experiments typically sodium hydroxide (NaOH) at a concentration of 6 mol per liter of water and a temperature of 80°. To ensure a constant temperature and concentration, the etchant is kept in a covered beaker equipped with a temperature probe and magnetically stirred. CR39 slides were exposed to the NaOH solution for times ranging from minutes up to one and a half hours. During that process, the damaged plastic in a latent track dissolves more quickly than the unaffected surrounding bulk material [172]. Owing to the difference in the etching rate, a conical hole is generated at the respective position of a particle impact. The size of the cone grows with etching time up to a threshold were the etchant reaches the end of the particle range and the structure of the pit becomes progressively lost. Consequently, overetched and/or overexposed CR39 track detectors enter a saturation regime, where single ion impacts can not be identified anymore, potentially leading to the appearance of artificial ring-like structures when measuring ion beam profiles [173].

Following the process of etching, ion tracks are read out by a computer controlled, automated optical microscope [174]. The microscope is equipped with a motorized stage and a CCD camera, scanning the CR39 line by line in a predefined area at a magnification of typically 50×. A pattern recognition software (SAMAICA) analyzes the obtained images and saves a series of attributes for each detected ion crater, such as position, semi-minor and semi-major axis, etc. By precise control

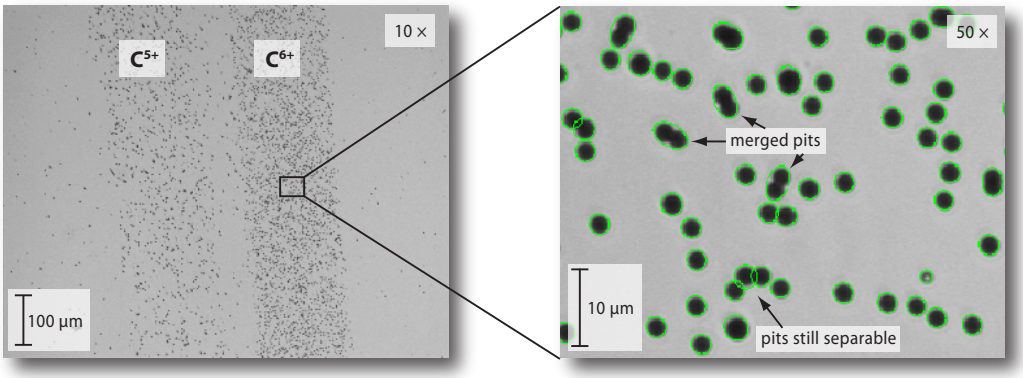

Fig. 4.6. *Exemplary images of carbon ion induced tracks on CR39 as seen after etching via an optical microscope at 10× (left) and 50× (right) magnification. The zoomed view of C^{6+} pits demonstrates the capability of the pattern recognition software to identify single ion impacts and determine their respective geometry (highlighted by green ellipses).*

of the etching parameters, different particle species can thus be distinguished by the characteristics of their respective pit. Figure 4.6 presents exemplary images of carbon ion tracks on CR39 obtained at 10× and 50× magnification and demonstrates the capability of the software to identify the geometry of single ion induced craters in the material. An even more detailed analysis of the tracks by virtue of an AFM could additionally provide energy resolution from measurements of the conical track length [175]. However, this method was not applied within the framework of this thesis.

Despite the prime qualities of CR39 as an ion detector, such as the high reliability, the insensitivity to electromagnetic radiation and electrons and the needlessness of an elaborate calibration to infer particle numbers, its main disadvantage remains the greatly time-consuming data analysis. The described evaluation procedure requires several hours, making CR39 unattractive as a long term solution for day-to-day ion beam characterization.

Radiochromic Film (RCF)

Radiochromic film (RCF) is widely employed for dosimetry of ionizing radiation in medical physics, being specifically designed for dose measurements of absorbed high-energy photons. Nevertheless, it has also successfully served as a detector for laser-accelerated proton beams [176]. Two different types of RCF have been used for experiments described within this thesis, namely GAFCHROMIC HD-810 and CAFCHROMIC MD-55, both supplied by ISP International Specialty Products. A schematic of the configuration of such films is depicted in figure 4.7. RCF is largely

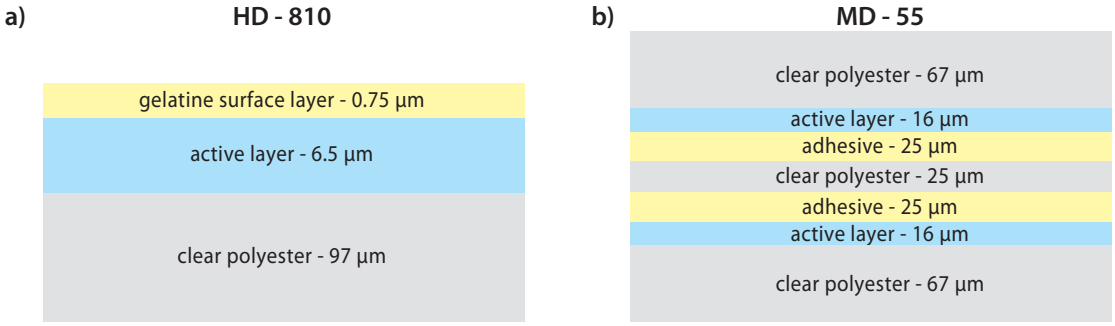

Fig. 4.7. *Configuration of (a) GAFCHROMIC HD-810 and (b) GAFCHROMIC MD-55 radiochromic dosimetry film (RCF).*

insensitive to light in the visible range, but in contrast to CR39 sensitive to all kinds of ionizing radiation. When exposed, the monomer in the active layer undergoes a polymerization to form a dye of darker blue color. No additional development of the film is required and the optical density response is nearly linear over several orders of magnitude in dose. While the $\sim$ 100 μm thin HD-810 provides only a single active layer, MD-55 of $\sim$ 250 μm thickness features two pieces that are laminated together by adhesive tape. Owing to the thus increased active layer thickness, MD-55 offers a sensitivity that is about a factor of 6 higher than in the case of HD-810.

After exposure, the film can be read out by means of a densitometer, spectrophotometer or even a simple flatbed color scanner in transmission mode. To obtain the absorbed dose however, a calibration measurement with a well defined dose is needed beforehand [176]. In practice, this requirement proofs to be of concern due to batch-to-batch variations in the RCF sensitivity that can be as high as 10%. Additionally, the effect of dose suppression near the Bragg peak in the energy loss distribution (see figure 4.10) has to be taken into account in an actual experiment. Consequently, a resulting error in the determined dose of $\sim$ 20% can typically be achieved.

Image Plate (IP)

Image plate detectors were initially developed and applied as an alternative to photofilm in the medical x-ray diagnostics field [177]. However, similar to RCF, image plates are sensitive to a much broader range of radiation kinds, such as UV, ions, electrons, gamma rays etc. For the experiments presented in this thesis, commercially available IPs manufactured by Fujifilm were used, more specifically the types BAS-SR (high resolution) and BAS-MS (high sensitivity).

The IP film is a flexible imaging sensor that incorporates a layer of photo-

stimulable phosphor, i.e., barium fluorobromide containing a trace amount of bivalent europium as a luminescence center, $BaFBr:Eu^{2+}$. Bunches of very small crystals of this specially designed luminescent material are uniformly coated on a polyester support film. Upon irradiation, europium ions are exited into a metastable state that traps and stores the incident energy. Readout is done by photo-stimulation of such metastable states, where the ions are excited to higher energies that are no longer metastable before returning to the ground state while emitting a photon. This photo-stimulated luminescence (PSL) process is initiated by a scanning laser beam and the released energy at a wavelength of 400 nm is collected via a light guide and amplified by a photomultiplier tube. Such scanners are also commercially available, for the described work a Fujifilm FLA 7000 was mostly employed. Typically, a pixel size of $50 - 25\,\mu$m is achieved, limited by the scanning system.

The prime features of the image plate detector are its ultrahigh sensitivity, its large dynamic range and its superior linearity, meaning that the recorded PSL signal is proportional to the incident dose in the entire detector range. Moreover, it is reusable after erasing residual stored energy with an intense white light source.

For the experiments described in the following, image plates have been used to detect highly energetic electrons and ions. The response of image plates to exposure of such particle beams has been extensively studied and calibration curves for electrons [178, 179] and ions [180] can be found in the existing literature.

Micro Channel Plate (MCP)

A MCP is closely related to an electron multiplier. The one that was used for the experiments conducted at MBI Berlin (see chapter 7) is a single stage device composed of one plate that is formed by an array of miniature electron multiplier channels and a phosphor screen. A schematic drawing of the configuration of such an instrument is depicted in figure 4.8. The channels are orientated in parallel, exhibiting a small angle of 8° with respect to the surface normal. In the case of the particular MCP utilized, the channels have a diameter of $25\,\mu$m and a pitch of $31\,\mu$m. The plate has an effective diameter of 77 mm at a thickness of 1 mm. In order to build up a potential gradient along the plate surface normal, a high voltage of $V_{MCP} \simeq -1\,$kV is applied.

Due to the angle of the channels with respect to the plate surface normal, an energetic particle or photon that is entering the small channel orifice is likely to hit the channel wall. Subsequently to the impact, secondary electrons will be emitted from the channel surface if the energy of the incident particle or photon is sufficient.

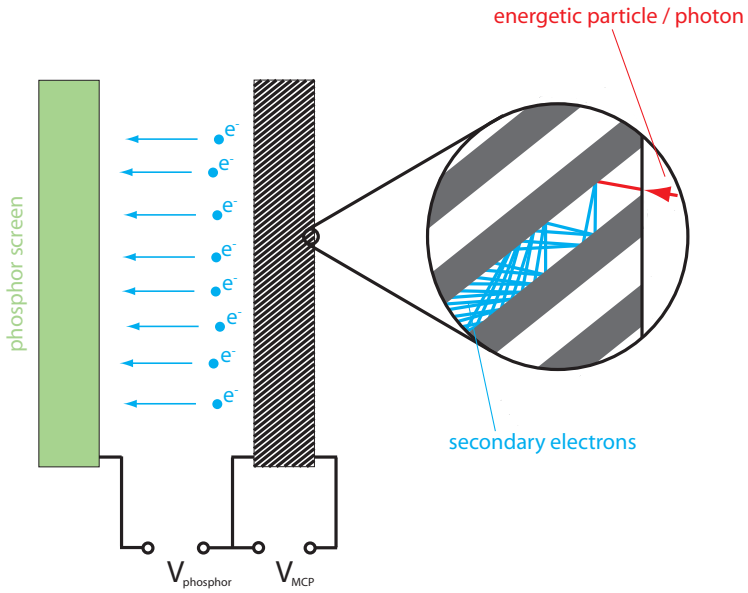

Fig. 4.8. *Shown is a schematic of a MCP detector cross section and the high voltage circuit. The plate can be regarded as an array of miniature electron multipliers. When an energetic particle or photon hits an inner channel wall, a cascade of secondary electrons is generated by the potential gradient along the plate surface normal. Those electron bunches are then accelerated to hit a phosphor screen and the resulting fluorescent light is imaged onto a CCD camera.*

These electrons are accelerated by the potential gradient, thus being capable of generating another generation of secondary electrons when they are striking the inner wall again. Hence, a cascade of secondary electrons is produced that leads to a huge magnification in signal strength. Upon channel exit, the electron bunches are accelerated towards a phosphor screen by a second potential gradient of $V_{\mathrm{phosphor}} \simeq 5\,\mathrm{kV}$. Resulting fluorescent light emitted by the phosphor screen is imaged onto a cooled CCD camera attached to the MCP.

Calibration of the MCP detection system was done using 5.48 MeV alpha particles from a ^{241}Am source [181]. By this method, the camera response as a result of the impact of a single ion onto a channel is obtained. The calibration value was verified by counting corresponding particle numbers on CR39 plates that were irradiated in parallel. Varying the energy of the incident alpha particles (at about 3.8 and 1.5 MeV) did not influence the registered camera response. It has to be noted here that, even though all operating parameters are kept constant, the calibration value strongly depends on the MCP age as the detector tends to degrade over time, necessitating repeated revision.

In contrast to previously described detectors, such as CR39, RCF and IP, the micro channel plate offers a genuine online detection of ions without the need of film

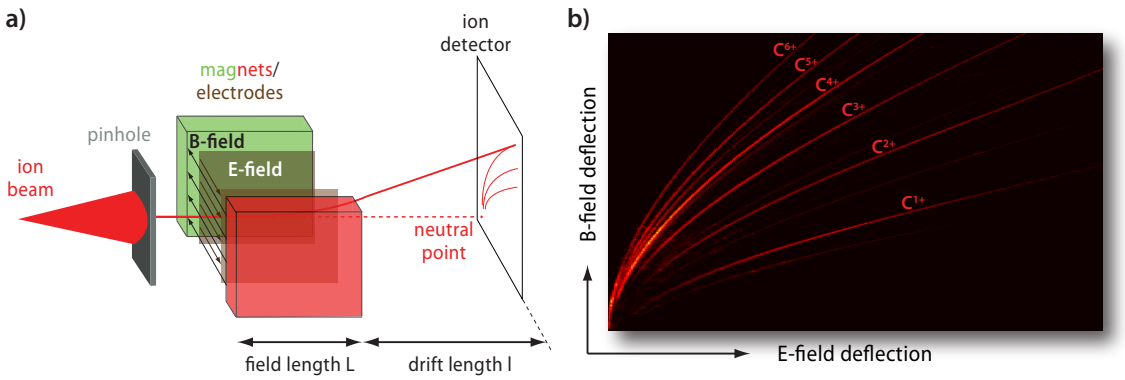

Fig. 4.9. *The basic scheme of a Thomson parabola spectrometer is illustrated in (a). Ions within a small solid angle of typical order 1×10^{-7} sr are selected by a pinhole and subsequently deflected in parallel orientated electric and magnetic fields of length L being set up orthogonal with respect to the initial propagation direction. After a field-free drift distance l, ions hit a two-dimensional detector. An exemplary image of the resulting parabolic tracks of carbon ions covering all charge states as seen on an etched and scanned CR39 plate is presented in (b).*

development, scanning etc. Thus, such a system is preferable for use in numerous-shot experiments on high repetition rate systems. However, MCPs are comparably expensive, susceptible to electromagnetic noise and require ultra-high vacuum conditions. A future alternative might be provided by scintillators, an approach that is currently being pursued in collaboration with Physikalisch-Technische Bundesanstalt (PTB), Braunschweig.

4.2.2 Measuring Instruments

Thomson Parabola Spectrometer

Although the Thomson parabola spectrometer was developed by J. J. Thomson nearly hundred years ago [182], laying the foundation for mass spectrometry, it still remains a prime tool for characterization of laser-driven ion beams nowadays. The main advantage of the spectrometer is its capability to record the energy distributions of all accelerated ion species in one single shot.

A schematic setup of the device is depicted in figure 4.9a. A pinhole of typical diameter $100 - 300\,\mu$m is placed into the cone of ions to produce a pencil beam. Particles passing the aperture are subsequently deflected in parallel electric and magnetic fields that are orientated orthogonally with respect to the beam propagation axes. The magnetic field is provided by two permanent magnets surrounded by an iron yoke, giving a nearly homogenous field of a few 100 mT in between. Two copper plates, molded in insulating plastic, are inserted in the gap of the magnet,

typically separated by a distance of $\sim 2\,\mathrm{cm}$. By applying a voltage of several kV across the plates, an electric field of order MV/m parallel to the magnetic field is generated. Upon exit of such fields and after a field-free drift region, ions hit a two-dimensional ion sensitive detector (see section 4.2.1) placed at the back of the spectrometer. The origin (or neutral point) is hereby given by impacts of uncharged particles propagating straight through the spectrometer. Figure 4.9b shows an exemplary image of carbon ion traces covering all charge states as seen on an etched and scanned CR39 plate.

An analytical solution for the shape of the parabolic tracks appearing on the detector can be found starting from the Lorentz force

$$\vec{F} = q_i \left(\vec{E} + \vec{v} \times \vec{B} \right) \tag{4.1}$$

with $q_i = Ze$ being the respective ion charge. The initial ion propagation axis is chosen as z and the electric and magnetic field are oriented along the x-direction. Assuming constant, homogenous fields of equal length L and a field-free drift length l, the corresponding particle deflection along x and y calculates to

$$x = \frac{q_i E L}{m_i v^2} \left(\frac{L}{2} + l \right) \tag{4.2}$$

$$y = \frac{q_i B L}{m_i v} \left(\frac{L}{2} + l \right) \tag{4.3}$$

where m_i refers to the ion mass and v to its velocity. By combining the two equations while eliminating the velocity, the well known parabola expression

$$y^2 = \frac{q_i B^2 L}{m_i E} \left(\frac{L}{2} + l \right) x \tag{4.4}$$

which defines the ion track shape is obtained. The ion kinetic energy $E_{kin} = 1/2\, m_i v^2$ at a given position $[x, y]$ on the track can simply be extracted from the deflection due to the magnetic field (equation 4.3) and is thus given by

$$E_{kin} = \frac{\left[q_i B L (L/2 + l) \right]^2}{2 m_i} \frac{1}{y^2} \tag{4.5}$$

Accordingly, a spatial interval $[y, y+\Delta y]$ on the detector corresponds to an energy bin $[E_{kin}, E_{kin} + \Delta E_{kin}]$, and the spectrum $dN/dE_{kin} \simeq \Delta N/\Delta E_{kin}$ of each ion species can be determined by counting ion numbers ΔN in the respective intervals ΔE_{kin}. Keeping the spatial bin size Δy constant will result in growing intervals ΔE_{kin} as the

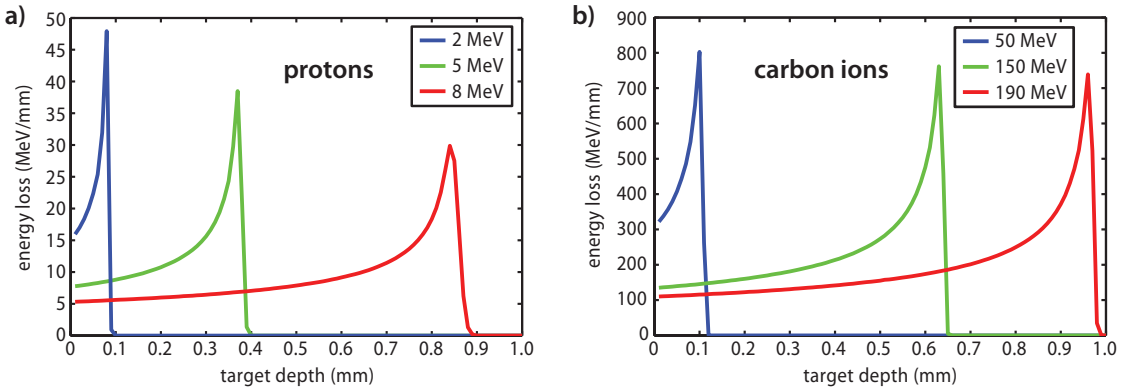

Fig. 4.10. *Energy loss distributions of protons (a) and carbon ions (b) of varying initial energy incident on 1 mm of CR39, calculated using the Monte Carlo code TRIM. The majority of the ion's respective energy is deposited in the Bragg peak, shortly before the particle is finally stopped.*

particle energy increases, reducing the resolution of the obtained spectrum towards the cut-off. However, a lower limit for the spatial binning is imposed by the pinhole diameter in order not to introduce artificial noise. Therefore, Δy was chosen to be of constant value larger than the pinhole size for the analysis of ion traces presented in the following chapters. Finally, the retrieved ion number is normalized to an energy interval of 1 MeV and a solid angle of 1 msr. A home-made software was used to evaluate Thomson parabola tracks according to the described routine [183].

To test the accuracy of the analytical solution given by equation 4.4 for a realistic scenario where the fields are not exactly constant and homogenous, but instead inhomogeneous fringe fields are present, the equations of motion were solved numerically in previous work [184]. The three-dimensional electric and magnetic fields were hereby simulated and the obtained magnetic field was verified by measurements on axis using a Hall probe. Comparison between the simple analytical solution of equation 4.4 and the exact numerical solution yielded only for low energetic ions detectable but still marginal differences between the calculated ion tracks. For the high energetic part of the spectrum the deviation becomes negligible.

Detector Stack

While the Thomson parabola spectrometer served as the prime diagnostic in numerous experiments to obtain energy distributions of all accelerated ion species in a single shot, its main limitation is given by the small solid angle of typical order 1×10^{-7} sr detected. In case quite inhomogeneous ion beams need to be characterized and/or the ion beam pointing exhibits large shot-to-shot fluctuations, a measuring

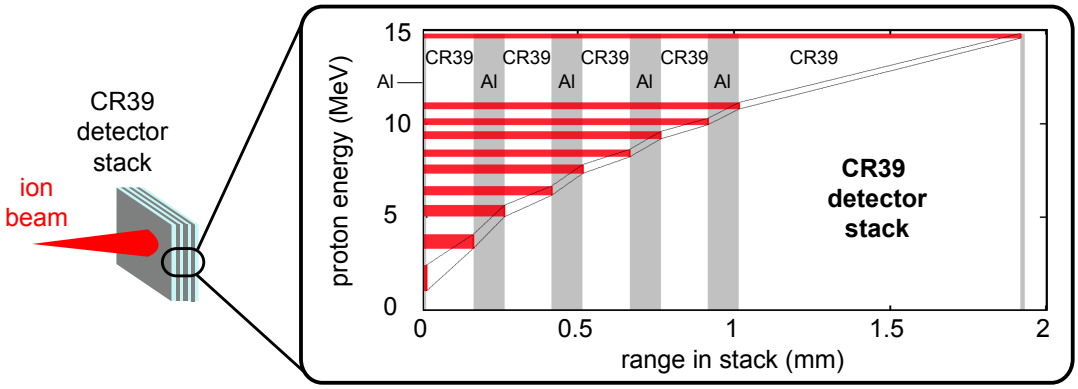

Fig. 4.11. *Presented is a schematic of a detector stack composed of* 150 μm *thin CR39 plates (white) alternating with aluminum slices of thickness* 100 μm *(grey). A* 1 mm *thick CR39 layer is included at the back and the whole stack is covered by* 15 μm *thin aluminum foil. The red horizontal bars illustrate proton energy intervals corresponding to a specific layer's front or back surface that were calculated on the basis of stopping range tables available from the SRIM code.*

instrument capable of capturing the full beam is desired. Additionally, ion beam imaging at varying energies is of interest to obtain information on the beam profile and extract values for laser-to-ion conversion efficiencies.

These needs are met by detector stacks composed of RCF or thin CR39 plates. In contrast to the previously described Thomson parabola spectrometer, no electric or magnetic fields are applied to disperse the incident ion beam. Instead, energy resolution is obtained by the difference in penetration range for varying particle velocities. The scheme takes advantage of the fact that ions deposit the vast majority of their energy shortly before being finally stopped, a feature known as the Bragg peak in the energy loss distribution. Figure 4.10 gives examples of such energy loss curves over target depth for protons and carbon ions of different initial energies incident on 1 mm of CR39. The data was calculated using the Monte Carlo code "Transport of Ions in Matter" (TRIM) [185]. Following from the ion energy loss characteristics, each layer in the stack corresponds to a certain energy of a given ion species, so that the Bragg peak coincides with the respective layer depth. Owing to their comparably short stopping ranges, heavier ions typically appear only on the very first few layers of the stack whereas protons penetrate much deeper, making this type of diagnostic particularly suitable for the characterization of proton beams.

An exemplary detector stack schematic as it was used in the experiments focussing on ion acceleration from microspheres (chapter 5) is shown in figure 4.11. Here, 150 μm thin CR39 plates (white) alternating with aluminum slices of thickness 100 μm (grey) were used, including a 1 mm thick CR39 layer at the back. The whole

stack is covered by 15 μm thin aluminum foil to protect the ion sensitive layers from damage by intense residual laser light hitting the stack. Proton energy intervals corresponding to a specific layer were calculated on the basis of stopping range tables available from the "Stopping and Range of Ions in Matter" (SRIM) package [185] and are illustrated by red horizontal bars in figure 4.11. In contrast to stacks composed of RCF, ion energy deposition located near the front surface or the back face of each CR39 plate can be distinguished as a pit appears either on the front or the back after etching. This results in two energy intervals per layer instead of only one, providing enhanced energy resolution.

Detector stacks have also been used in combination with Thomson parabola spectrometers (see chapter 6). For this purpose, the highest energetic ions forming the central part of the beam are transmitted through a small hole in the stack center and captured by the spectrometer.

Chapter 5

Shock Acceleration of Ion Beams from Spherical Targets

In the vast majority of previous experimental studies on ion acceleration driven by highly intense laser pulses that were carried out over the past 10 years, solid density planar foils in the micrometer thickness range were used as targets. Here, target normal sheath acceleration (TNSA [67], refer to section 2.5.1 for details) was found to be the predominant mechanism responsible for the emission of multi-MeV, high-quality ion beams. Relativistic electrons are driven through the target by the intense laser pulse and set up an electric field at the nonirradiated side of the target. Reaching magnitudes above 1 TV/m, those fields ionize atoms in the surface layers and subsequently accelerate the ions, predominantly protons due to their high charge-to-mass ratio, to energies of up to 60 MeV [82] in a collimated beam. Lower energetic protons are produced in the outer regions of the electric field, which extends transversely to a diameter of several 100 μm [77, 80, 186]. This enormous lateral extension is attributed to recirculating electrons which spread around the target, thus causing a decay of the acceleration field. Therefore, mass-limited targets, i.e. targets with transverse dimensions comparable to the laser focus are expected to enhance the electric fields, owing to the confinement of recirculating hot electrons, which ultimately results in increased ion energies [187]. With this respect, recent particle-in-cell (PIC) simulations [188, 189] and experiments [190, 191] favor a spherical target geometry with the drawback of a nearly isotropic ion emission.

In this chapter, the first time observation of strongly directed ion beam emission from laser irradiated mass-limited plastic spheres is presented. The protons exhibit a broad spectrum with cutoff energies of up to 8 MeV, which compares to $1-3$ MeV obtained from extended aluminum and plastic foils when irradiated under identical

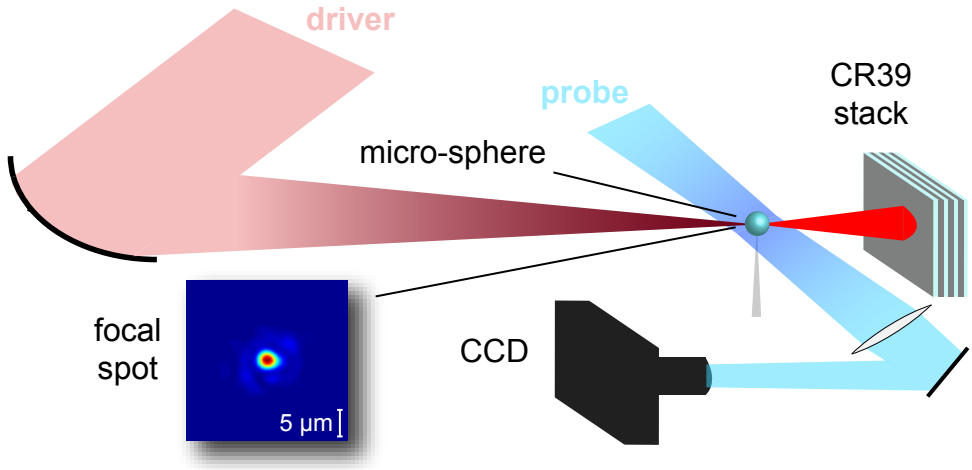

Fig. 5.1. *Experimental setup including the driver beam at the fundamental wavelength, the frequency-doubled transverse probe pulse used for capturing shadowgraphy images of the interaction and the CR39 film stack for ion detection. In addition, a characteristic focal spot image of the driver is presented, reaching a peak intensity of* $1 \times 10^{20}\,\mathrm{W/cm^2}$ *at a Strehl ratio of 0.29.*

laser conditions. Three-dimensional PIC simulations were carried out as a part of my PhD work in addition to the experimental studies, supporting the interpretation that the directed ion beams are accelerated in a converging shock launched by the laser. The reported results are published in Physical Review Letters [40].

5.1 Experimental Setup

The experiments were conducted using the ATLAS Ti:Sapphire laser at the Max-Planck-Institute for Quantum Optics in Garching as it is described in detail in section 3.2.1. The system delivers light pulses to the target containing 0.6 J of energy within a pulse duration of 45 fs at a center wavelength of $\lambda_0 = 790\,\mathrm{nm}$. A 15 cm focal length parabolic mirror tightly focuses the 7 cm diameter beam to a measured typical spot size of $3.3\,\mu\mathrm{m}$ full width at half maximum (FWHM) diameter. This yields a peak intensity of around $1 \times 10^{20}\,\mathrm{W/cm^2}$, which is equivalent to a dimensionless laser field amplitude of $a_0 \simeq 6.7$. The Strehl ratio, i.e. the ratio of the peak intensity of the measured point spread function (PSF) to the peak intensity of a diffraction-limited PSF of a flattop beam, calculates to 0.29. The relative intensity of both the ASE pedestal and short prepulses on the ps timescale was characterized by a 3rd order autocorrelation measurement, giving a contrast of better than 10^8 until 4 ps before the main peak (see figure 3.6). At above 400 ps before the arrival of the main peak, a fast Pockels cell further suppresses the ASE pedestal and prepulses by additional

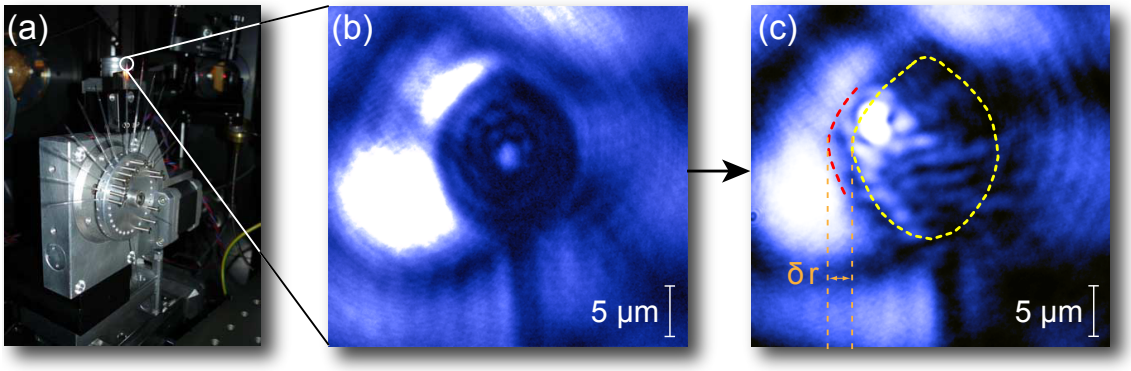

Fig. 5.2. *Shown is the motorized target wheel employed for quick sphere replacement after a shot (a) and a magnified view of a typical microsphere target as it appears on the imaging system before the shot (b) and at the time of interaction (c). The white regions visible both in (b) and (c) outside the contour of the spherical target arise from inhomogeneities of the probe beam profile, whereas the bright white spot that appears on the target shadow in (c) is generated by self-emission of the target at the second harmonic of the incident pulse. The increased radius of the sphere δr results from the deflection of the probe laser pulse in the pre-formed plasma.*

two orders of magnitude.

A schematic setup of the experiment comprising the transverse probe beam and the ion detector is shown in figure 5.1. To generate the probe, a small fraction was split off the edge of the full driver beam by use of a pick-off mirror. Subsequently, the beam was converted to the second harmonic in a beta barium borate (BBO) nonlinear crystal, passed a $\lambda/2$ waveplate to rotate the polarization by 90° with respect to the main beam, and was finally guided to the target. The targets were positioned by imaging the focal spot volume with a magnification of around 50 onto two CCD cameras.

Figure 5.2a displays the motorized target wheel that was employed for a quick replacement of a microsphere after a shot. In figure 5.2b, an exemplary picture of such a mass-limited target, i.e. a poly(methyl methacrylate) (PMMA) sphere of 15 μm in diameter mounted on a sub-μm thin glass capillary is shown as it appears on one of the monitoring cameras. A detailed description of the target fabrication process that was developed as a part of this PhD work can be found in section 4.1.1. The same CCD imaging system was used to capture a snapshot of the sphere right at the time of the interaction using the frequency-doubled transverse probe pulse with a duration of approximately 100 fs as a backlighter (figure 5.2c). Precise synchronization with the main pulse was achieved by shadowgraphy of plasma channels generated when focussing the driver beam at increased background gas pressures.

In the image obtained during the interaction the spheres appear about 4.4 ±

0.4 μm larger in diameter, which is attributed to the presence of a preplasma caused by the amplified spontaneous emission (ASE) pedestal. For simplicity, an exponential density profile is assumed outside the initial sphere radius r_0

$$n_e(r) = n_{e0}\, e^{-(r-r_0)/L} \tag{5.1}$$

where n_{e0} is the electron density of a fully ionized PMMA sphere and L stands for the density scale length of the plasma. Performing ray-tracing calculations for the employed imaging system (f/2), the apparent radial increase of the sphere δr equals *twice the distance* between the critical surface and the surface of the undisturbed sphere,

$$n_e(r_0 + \delta r/2) = n_{c,\lambda_0/2} = n_{e0}\, e^{-\delta r/(2L)} \tag{5.2}$$

with $n_{c,\lambda_0/2}$ representing the critical density for the probe-laser pulse. Thus, we obtain the scale length

$$L = \delta r \, \left(2\ln(n_0/n_{c,\lambda_0/2})\right)^{-1} \simeq 0.3\,\mu\text{m} \tag{5.3}$$

This value is in excellent agreement with one-dimensional calculations for the named prepulse conditions that were done in collaboration with R. Ramis of the ETSI Aeronáuticos, Universidad Politécnica de Madrid, Spain using the hydrodynamic code MULTI [192]. Besides displaying the shadow of the expanded preplasma, figure 5.2c also shows the self-emission of the target at the second harmonic of the incident pulse, giving a measure of the laser focal spot size and position on the target surface.

Stacks of CR39 plastic track detectors alternating with aluminum foils were used to record the proton beam profile at different energies. Details on CR39 are given in section 4.2.1. Additionally, an in-depth description of the detector stack is presented in section 4.2.2, where figure 4.11 shows the sensitivity in energy of a typical stack used in the experiments. As specified in these sections, CR39 plates were etched in sodium hydroxide after irradiation to make each ion impact visible, so that the absolute number of accelerated ions could be counted with an automated scanning microscope. Unmistakable identification of protons is enabled by their characteristic damage spots imprinted in CR39. Only protons which are stopped close to the front or the rear surface of the CR39 plates are visible, which allows the definition of a detectable energy interval for both sides of each layer of the stack. The energy losses of protons inside the detector stack were calculated using the stopping power data tabulated in the SRIM package [185]. In order to reduce the gaps in energy between

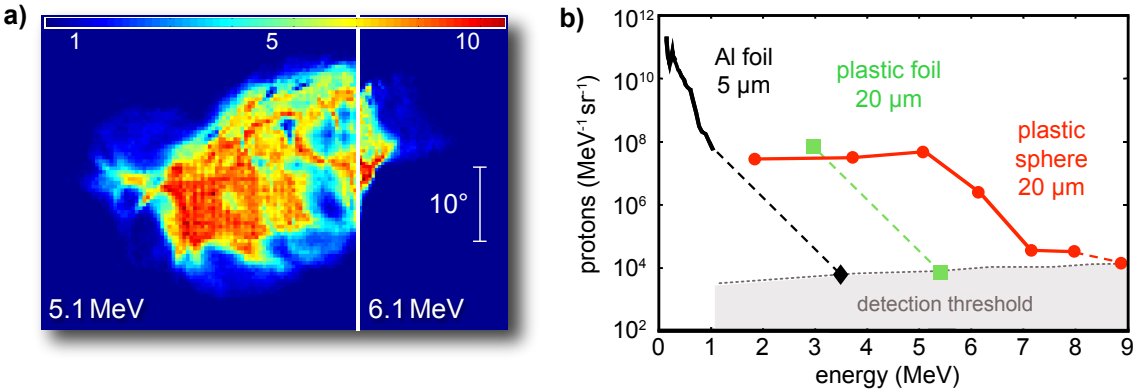

Fig. 5.3. *(a) Typical proton beam profile at the highest energy as obtained from the CR39 stack (colorbar indicates number of particles in units of $10^6/\mathrm{rad}^2$, energies represent the center of the respective interval). The fine grid-structure is an artifact resulting from double counts in the automated scanning analysis. (b) Proton energy distributions from aluminum foils (black), plastic foils (green), and plastic spheres (red). The curves for the plastic targets are extracted from the CR39 stack to appear as in the case of a spectrometer with small angular acceptance (10^{-7} sr) placed in laser propagation direction. The dashed lines are a linear extension of the spectra to the next higher energy level in the stack where no proton signal was observed.*

intervals, the stack was split by using an additional 50 μm aluminum filter covering one half of the area.

Alternatively, the detector stack could be replaced by a Thomson parabola spectrometer which was used for the measurement of ions accelerated from aluminum foil targets due to the low ion energies obtained in this case. Full particulars on the configuration and operation principles of a Thomson parabola spectrometer can be found in section 4.2.2. Although Thomson parabola spectrometers are frequently used to detect ions accelerated by high intensity laser pulses, their main drawback is the small acceptance angle which is usually less than 1 μsr, resulting from a pinhole of around 100 μm in diameter placed at a distance of up to one meter. In the experiments presented here, the detector stack covered a solid angle of ~ 0.5 sr (i.e., $\sim \pm 20°$) in forward direction.

5.2 Measured Ion Beams

A typical profile of the proton beam produced from a mass-limited target is shown in figure 5.3a. The images are obtained by counting the ion impacts on each CR39 plate and plotting a two-dimensional histogram. In fact, the resulting figures show the same information as may be obtained by a two-dimensional detector with a linear response on the number of incident ions. For smaller energies, similar proton profiles with comparable angular divergences of $30 - 40°$ are obtained except for the lowest

energy of around 1 MeV. Here, the CR39 plates were homogenously irradiated which is attributed to an isotropically emitted proton beam. Owing to the small spatial separation of ion impacts on the low energy layers of the stack, the automated scanning system could not be used. Therefore, representative parts of the CR39 plates were counted manually which allows to extract the spectral distribution as it would appear in a spectrometer with a small angular acceptance ($\sim \mu$sr).

The proton spectrum obtained for the spheres is compared to results from irradiated foils in figure 5.3b. For 5 μm thick aluminum foils the exponential spectrum usually extends to energies between 1 and 2 MeV (black solid line), while 3 MeV protons were observed from a 20 μm thick plastic foil (green). The flat spectrum of protons accelerated from spheres extends to 8 MeV. It is noteworthy, that an energetic, highly directed proton beam originating from the irradiation of a microsphere was seen in approximately one out of four shots. This limit in reproducibility can be attributed to a random pointing instability of the laser focus on target of $\sim \pm 5\,\mu$m. A more detailed discussion will follow later in the text.

5.3 PIC Simulations

Evidently, spherical targets emit proton beams into an angle of divergence comparable to that observed for extended foils. This observation contradicts the assumption that ions are predominantly emitted from the surfaces of the sphere, where a nearly isotropic emission pattern is expected. To explain this behavior, three-dimensional particle-in-cell simulations were conducted using the code ILLUMINATION [193]. The experimental setup was modeled by placing a sphere of diameter 6.4 μm at the center of a rectangular simulation box with dimensions 23 μm in transverse and 54 μm in longitudinal, i.e., laser propagation direction, which is smaller than the actual sphere size of around $15 - 20\,\mu$m owing to computational limitations. The microsphere was composed of a preionized hydrogen plasma with an initial electron density of 10^{22} electrons/cm^3. To remove the influence of unwanted reflections, absorbing layers were added to the boundaries of the box. The transverse and longitudinal grid size amounted to 46 nm and 23 nm, respectively. The laser pulse was of hyperbolic secant envelope shape with parameters such as FWHM pulse duration, spectrum center wavelength, Gaussian focal spot FWHM diameter at the center of the simulation box and dimensionless laser field amplitude chosen to match the actual experimental settings.

Although the real density of the targets is considerably higher than the micro-

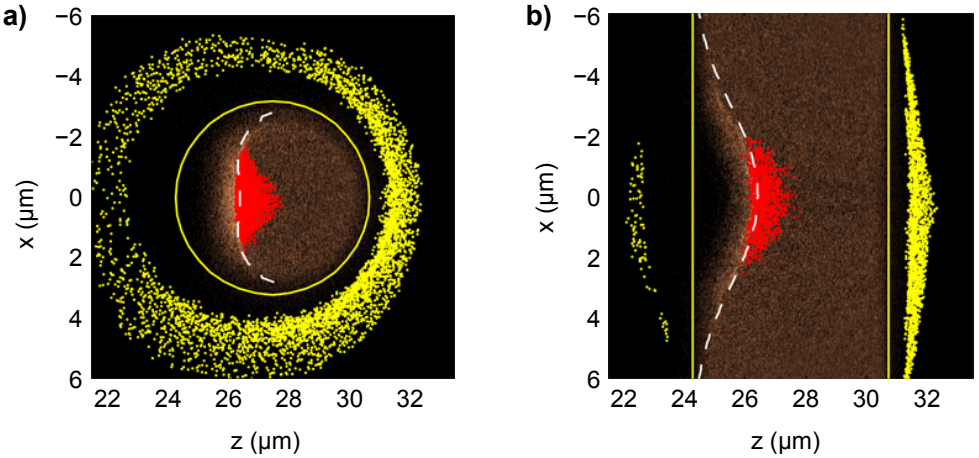

Fig. 5.4. *Color-scale plot of the proton density (ranging from 0 to $4 \times 10^{22}/\mathrm{cm}^3$) obtained from 3D-PIC simulations 133 fs after the arrival of the laser pulse maximum on (a) a sphere and (b) a foil target. The yellow lines indicate the initial target boundaries. Protons with energy in access of 1 MeV are represented by yellow and red dots, marking surface and shock accelerated ions, respectively. The white dashed lines illustrate the shock-front as calculated using the analytical model which is described in the text.*

sphere density used in the simulations, the laser-plasma interaction is expected to happen within the preplasma at density values around the relativistically corrected critical density γn_c, where $\gamma = (1 + a_0^2/2)^{1/2}$ and $n_c = 1.75 \times 10^{21}$ electrons/cm^3, which for the experimentally achieved peak laser amplitude of $a_0 \simeq 6.7$ yields 8.5×10^{21} electrons/cm^3. The presence of a preplasma is expected for the prepulse conditions at ATLAS and was indeed observed in the images of the spheres obtained within the time window of the interaction (figure 5.2c).

Figure 5.4a shows the resulting ion density distribution in the plane of laser polarization as obtained from the described 3D-PIC simulations and every 8th proton (macro particle) close to this plane with energies above 1 MeV. The snapshot was taken 133 fs after the interaction of the laser pulse maximum with the sphere. It is apparent from this picture, that the directed ion beam originates from the interaction zone (red dots) where a converging shock structure forms. In fact, closer analysis reveals that the fastest ions move with twice the shock velocity as expected for shock acceleration [38]. The ions from the surface of the sphere (yellow dots) are emitted almost isotropically into 4π, which was reported in a number of recent studies using PIC codes [187–189, 194] and is confirmed experimentally [190, 191].

This behavior is contrary to the case of a flat foil irradiated under identical conditions (figure 5.4b). The TNSA ions are now directed, while the shock established at the target front is divergent, owing to the laser hole-boring which also reflects in a larger divergence of the accelerated proton beam.

5.4 Analytical Model

For a better understanding of the directed emission a 2D analytical model for the evolution of the shock front was developed, based on the equation for the shock velocity ([39], refer to section 2.5.2 for details)

$$v_s/c = a_L/\sqrt{2}\ \ (m_e/m_i)^{1/2}\,(n_c/n_i)^{1/2} \tag{5.4}$$

where m_i and m_e are ion and electron mass, n_i and n_c are ion density and critical density for the driving laser pulse. The laser amplitude $a_L = a_0 \cdot f(r)$ varies with the radial coordinate r with a gaussian shape in accordance with above described simulations, i.e., $f(r) = \exp(-2\ln 2\ r^2/w^2)$ where w is the FWHM diameter of the spatial intensity distribution. Depending on the local angle of incidence α, the intensity must be corrected by multiplication with $\cos\alpha$. The direction of the radially varying shock velocity with magnitude $v_m = v_s\,(\cos\alpha)^{1/2}$ is given by the gradient of the reflecting surface $z(r)$, i.e., the shock front. Using $\tan\alpha(r,t) = \partial z/\partial r|_{(r,t)}$ and $\cos\alpha = 1/\sqrt{1+\tan^2\alpha}$, the equations of motion for the points defining the shock front are obtained

$$\begin{aligned}\frac{dr}{dt} = v_r(r,t) &= -v_m \sin\alpha \\ &= -v_s(\cos\alpha)^{1/2}\sin\alpha \\ &= -v_s \tan\alpha(1+\tan^2\alpha)^{-3/4} \\ &= -v_s\,\partial z/\partial r\left[1+(\partial z/\partial r)^2\right]^{-3/4}\end{aligned} \tag{5.5}$$

$$\begin{aligned}\frac{dz}{dt} = v_z(r,t) &= v_m \cos\alpha \\ &= v_s(\cos\alpha)^{3/2} \\ &= v_s(1+\tan^2\alpha)^{-3/4} \\ &= v_s\left[1+(\partial z/\partial r)^2\right]^{-3/4}\end{aligned} \tag{5.6}$$

which can be integrated numerically over the laser pulse duration τ_L. For the sake of simplicity, the pulse envelope was assumed to be flattop in time. The shape of the shock front at later times is then obtained by propagating each point (r,z) using the corresponding velocity $(v_r(\tau_L), v_z(\tau_L))$.

The result of this simple consideration is depicted by the white dashed lines in figure 5.4a and b for the two initial geometries. Given the simplicity of the

assumptions, the agreement of those estimates with the 3D-PIC results is quite remarkable. Calculations of the shock front for $15 - 20\,\mu$m diameter spheres closely resemble the results obtained for $6.4\,\mu$m, which validates the applicability of the conducted PIC simulations to model the experimental observations.

Introducing a transverse offset of $5\,\mu$m in the position of the laser focus, corresponding to the experimentally observed random pointing fluctuations of the incident beam on target, leads to a deflection of the shock front propagation direction of $\sim 30^\circ$ for a $20\,\mu$m diameter sphere, as well as a slight reduction in proton energy. Such a large deviation would exceed the detector acceptance half angle of 20°, causing the shock accelerated proton beam to miss the CR39 stack. Based on these considerations, the experimentally observed limit in reproducibility is attributed to the known jitter in the pointing of the laser focus.

Finally, the angular distributions of protons obtained from the PIC simulations for a foil and a sphere target were compared, dividing each into components accelerated from the front and from the rear surface, respectively. Motivated by the observation of the shock front, only protons with velocities greater than the shock velocity in the center were considered (energies above 1 MeV). For the foil target, the flux of the ions emitted from the rear surface exceeds the one of the front accelerated ions by a factor of 10. In the case of the sphere the result is inverted, the proton beam from the *front* is about *50 times as intense* as the beam of surface ions emitted into 4π.

It is worth noting, that the enormous difference in particle flux for protons originating from the two different sources, i.e., target front and back side, were not observed in 2D-PIC simulations which were performed for comparison. This shows the necessity of taking into account the full three-dimensional geometry when describing the interaction of the laser with a spherical target. Above considerations substantiate the conclusion that protons beams accelerated from the front of the target in a converging shock launched by the impinging laser pulse were indeed observed.

5.5 Summary/Conclusion/Outlook

In summary, the first experimental observation of strongly directed proton beams emitted from spherical mass-limited targets was achieved. When irradiated with an ultrashort, highly intense laser pulse, a converging shock front forms at the front side of the target. Protons accelerated in this shock reach energies well in excess of

the values observed in the TNSA regime under identical laser conditions, showing a plateau-shaped spectrum as predicted by Silva *et al.* [38]. 3D-PIC simulations of laser interactions with over-dense proton plasmas support the presented observations. The equation for the shock velocity [39] was extended to a radially dependent intensity and target profile and successfully implemented to reproduce the shape of the shock front obtained from PIC simulations.

Acceleration of energetic ion beams at high fluxes from the front surface of spherical targets is of great interest for the generation of high energy densities with interesting opportunities for fast-ignition concepts [34, 35] and neutron generation [190]. Moreover, the presented experimental study and modeling demonstrates the possibility to compensate for the effect of non-planar hole-boring by means of a pre-curved target surface. As will be seen in the following chapters, bending of ultrathin foil targets due to hole-boring of a non-tophat laser intensity distribution in the focus is a major obstacle in the quest for a strongly radiation pressure dominated ion acceleration regime. The findings obtained here motivate future experiments employing pre-curved nm-thin foils, which might be a promising technique to overcome this hurdle. Thus, a close-to-planar ion acceleration front could potentially be maintained for an extended period of time.

Chapter 6

Enhanced Ion Acceleration in the Transparency Regime

When the TNSA mechanism was investigated in previous studies, it was found that for fixed laser parameters the resulting ion energies can be increased by decreasing the foil target thickness. This effect is well understood in theory and described by a variety of existing models (e.g. [74, 75, 81, 82]). However, in actual experiments a lower limit for the foil thickness is imposed by the restriction that the shock wave launched at the target front side by the ASE-pedestal and prepulses must not have time to reach the target back to interfere with the rear surface sheath acceleration. In case the foil is chosen too thin, the sharp ion density gradient is massively perturbed, leading to a pronounced reduction in the ion cut-off energy. Thus, an optimum foil thickness exists for a given laser contrast, pulse duration and intensity [79] with typical values in the range of several microns.

Following this train of thoughts immediately poses the question if such an optimum is also present for an ideally perfect laser pulse contrast and what conditions define the optimum thickness in this scenario. As pointed out in more detail in section 2.5.1, the currently available popular models of Mora *et al.* [73, 74, 81] are no longer applicable for ultrathin targets, while in the analytical approach of Schreiber *et al.* [75] the maximum ion energy saturates as the foil thickness approaches zero. Nevertheless, recent theoretical studies based on PIC simulations indicate an enhanced acceleration when a sub-micron foil target is irradiated under ultra-high contrast, with a distinct optimum at thicknesses in the range of nanometers, i.e. at much smaller values than previously typically employed [195–199]. In particular, Esirkepov *et al.* carried out multiparametric PIC simulations and deduced an

empirical scaling law for the optimal normalized electron areal density [197]

$$\sigma_{opt} \approx 3 + 0.4\, a_L, \tag{6.1}$$

where $\sigma = (n_e/n_c)(d/\lambda_L)$. Giving a numerical example, for an electron density of $n_e = 660\, n_c$, a laser wavelength of $\lambda_L = 1\,\mu$m and a dimensionless laser vector potential of $a_L = 7$ (corresponding to a laser intensity of $7 \times 10^{19}\,\mathrm{W/cm^2}$) the expected optimum target thickness amounts to $d_{opt} \simeq 9\,$nm. The authors also noted that above condition is similar to the criteria of relativistic transparency for a thin foil [55]. That stands in strong contrast to the previous TNSA case where the foil remains opaque throughout the interaction.

To study this new regime experimentally, two challenging key requirements needed to be fulfilled.

Firstly, a technique had to be developed to fabricate free-standing, mechanically stable foils of only a few nanometers in thickness. For that purpose, diamond-like carbon (DLC) was chosen as target compound for all experiments carried out within the framework of this thesis. DLC is a metastable form of amorphous carbon containing a significant portion of sp^3-bonded atoms in the matrix, giving DLC its diamond-like properties. Compared to other materials available, the optically nearly transparent DLC foils offer an exceptionally high tensile strength, hardness and heat resistance, thus making DLC an ideally suited material for ultrathin self-supporting targets. An in-depth description of the methods used for target fabrication and characterization is given in section 4.1.2.

Secondly, an ultra-high laser contrast must be provided to prevent the accompanying ASE-pedestal and prepulses from ionization and preheating and to ensure the interaction of the main pulse with an ideally unperturbed target. Such a clean laser pulse can be achieved by use of plasma mirrors, acting as an ultrafast switch. Here, the beam is focussed onto an anti-reflection (AR) coated glass substrate at intensities in the range of $(10^{14} - 10^{16})\,\mathrm{W/cm^2}$, depending on the respective main pulse parameters. Thus, the ASE-pedestal and prepulses are kept below the ionization threshold and are therefore transmitted, while the main pulse is reflected off the dense plasma surface created by its own rising edge at typical efficiencies of $\sim 75\%$ [141, 142]. The contrast enhancement per reflection is therefore determined by the reflection coefficient of the AR coating, yielding values around 10^{-2}. Despite their high reliability and the potential to include plasma mirrors as an add-on to an already existing not-so-high contrast laser facility, their main disadvantages are the energy loss on every reflection and the limited repetition rate as the plasma mirror surface needs

to be replaced after every shot. A very recently introduced alternative approach for contrast enhancement that circumvents the energy losses and complies with high repetition rates is provided by short pulse pumped OPCPA (SPP-OPCPA). This new technique was investigated within the ATLAS based OPCPA laser development studies (chapter 8) and is implemented in the upgraded TRIDENT frontend type 1 (section 3.2.3).

Owing to these challenges, ion acceleration from ultrathin foils has so far been experimentally restricted to intensities of $1 \times 10^{19}\,\mathrm{W/cm^2}$ and below, as well as maximum pulse energies of 1 J on targets down to 20 nm in thickness [154–156]. Clearly, these parameters are more than an order of magnitude away from the predicted optimum condition. Enhanced ion acceleration in the transparency regime could therefore not be observed and only ion beams accelerated by TNSA from opaque foils have been obtained up to now using such nm-scale targets.

Within this PhD work, a series of measurements was carried out at different laser facilities and a variety of pulse parameters / target thicknesses that will be described in the following. For the first time, the anticipated enhanced ion acceleration in the transparency regime was demonstrated.

In the pioneering campaign, acceleration of proton and carbon beams from ultrathin, diamond-like carbon (DLC) foils of 50, 30 and 10 nm thickness irradiated with high-contrast pulses at significantly increased intensities of $\sim 7 \times 10^{19}\,\mathrm{W/cm^2}$ was investigated. At the optimum foil thickness of 30 nm, carbon ions reach cut-off energies of 185 MeV (15 MeV/u) which is a factor of 3 higher than reported so far [5, 18, 19]. The strong energy transfer from the electric field of the laser to the ions is attributed to an enhanced acceleration field, owing to relativistic transparency and subsequent volumetric energy transfer to the target electrons. These interpretations are confirmed by one- and two-dimensional particle-in-cell (PIC) simulations. In addition, a simple analytical model is presented to predict the optimum thickness for given laser parameters, demonstrating the direct connection between the instantaneous laser intensity at the time when the target becomes relativistically transparent and the resulting maximum ion energies. The results are published in Physical Review Letters [41].

6.1 Experimental Setup

The first set of experiments that are presented here were conducted at the TRIDENT laser facility at Los Alamos National Laboratory (LANL) using frontend

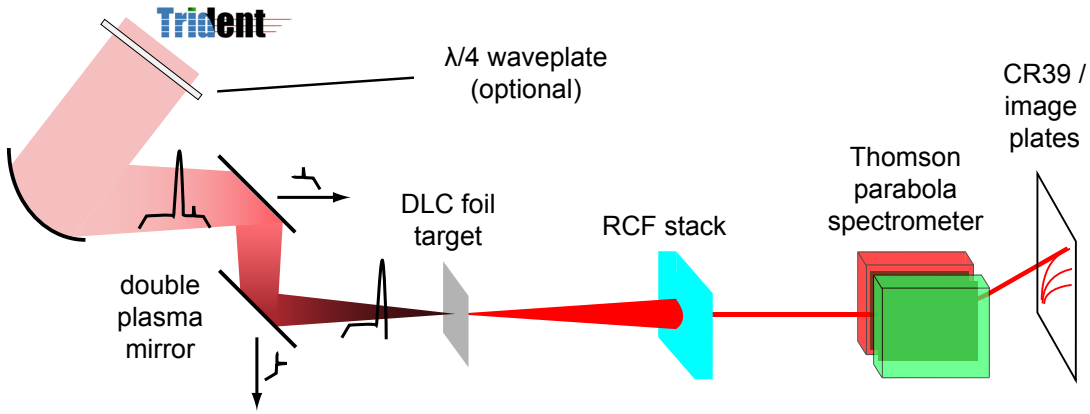

Fig. 6.1. *Experimental setup on the first TRIDENT campaign. To enhance the laser contrast, two AR coated glass slides acting as a double plasma mirror were placed into the converging beam after the focussing parabolic mirror. DLC foils of thicknesses 50, 30 and* 10 *nm, free-standing over a diameter of* 1 *mm, were placed at the focus and irradiated under normal incidence. The accelerated ions were characterized by a stack of RCF with the central, most energetic part of the beam being transmitted through a hole and guided to a Thomson parabola spectrometer equipped with CR39 and image plates.*

type 0, i.e., without SPP-OPCPA cleaning. A detailed description of the system is given in section 3.2.3. The employed 100 TW short pulse beam delivers 80 J pulses compressed to 700 fs at a central wavelength of 1053 nm. The initial contrast, i.e. the relative intensity of the amplified spontaneous emission (ASE)-pedestal arriving ~ 400 ps prior to the main peak, was determined to be $\sim 10^{-8}$.

In order to further enhance that value, two AR coated glass slides (R $< 0.5\%$) were introduced into the converging beam after reflection off a f/3.5 off-axis parabolic mirror (see figure 6.1 for the experimental setup). Each glass was placed at around 45° angle of incidence at intensities of 5×10^{14} W/cm^2 and 2×10^{15} W/cm^2, respectively. By use of this double-plasma mirror technique, a ps-timescale pulse contrast of $\sim 10^{-12}$ was achieved. The laser energy after the double reflection was measured to be $40 - 50$ J, depending on the input polarization, resulting in peak intensities of $\sim 7 \times 10^{19}$ W/cm^2 $- 9 \times 10^{19}$ W/cm^2 in a 10 μm FWHM diameter focal spot.

Diamond-like carbon (DLC) foil targets of thicknesses 50, 30 and 10 nm, free-standing over a diameter of 1 mm, were placed at the focus and irradiated under normal incidence. The presented experiment relied on foils with a fraction of $\sim 50\%$ sp^3 bonds and a density of 2.2 g/cm^3 produced by a modified DC glow discharge sputtering technique ([158], refer to section 4.1.2).

To characterize the accelerated particles, two complementary diagnostics were implemented behind the target: (i) a 5×5 cm stack of radiochromic films (RCF)

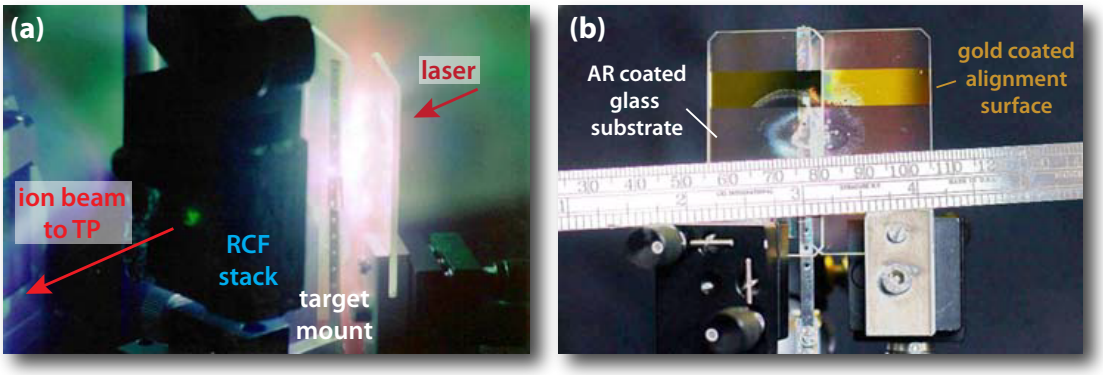

Fig. 6.2. *(a) Image of the experimental setup in action during a full system shot onto a DLC foil. Green background light arises from second harmonic generation in the laser-plasma interaction. The plasma mirror substrate is partly coated with gold to allow for precise beam alignment at low intensity prior to a target shot. Large-scale debris is generated by the blow-off plasma, requiring to exchange the substrates after each shot (b).*

separated 4 cm from the target to obtain the angular distribution of the emitted proton beam, (ii) a Thomson parabola spectrometer (TP) at a distance of 97.5 cm (solid angle $\sim 3.3 \times 10^{-8}$ sr) to detect particles propagating along the target normal, that were transmitted through a hole of diameter 4 mm located in the RCF stack center. At the back of the spectrometer, CR39 nuclear track detectors of 1 mm thickness were positioned, capable to stop and thus record traces of ions ranging in energy from $\sim$ 100 keV up to $\sim$ 10 MeV for protons and $\sim$ 210 MeV for carbon ions, respectively. To extend the detection interval to higher energy ions with ranges above 1 mm, an image plate covered by a 15 μm aluminum foil was placed behind the CR39 plate.

An actual image of a full system shot with the whole experimental setup in action is depicted in figure 6.2a. Owing to the small separation of the AR coated glass plates, large-scale debris originating from the blow-off plasma required to replace the plasma mirror substrates after each shot (figure 6.2b).

6.2 Measured Ion Beams

Irradiating a 50 nm DLC target with a linearly polarized pulse at high contrast, a maximum proton energy of 25 MeV was obtained. The corresponding beam profiles as seen on the RCF stack (figure 6.3) showed a homogenous angular distribution with opening angles of $\sim 40°$ for 14 MeV, $\sim 30°$ for 20 MeV and $\sim 18°$ for 25 MeV protons. Additionally, traces of carbon ions covering all charge states from C^{1+} to

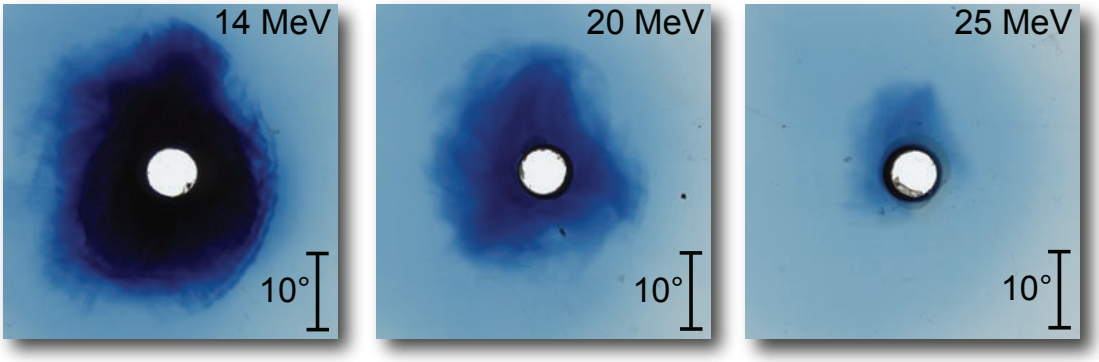

Fig. 6.3. *Characteristic image of the proton beam profile as seen on different layers of the RCF stack after a single shot on a 50 nm DLC target. A specific energy can be allocated to each layer, corresponding to the respective stopping range of ions penetrating the stack. As the proton energy increases, the beam opening angle narrows down with full cone angles of* $\sim 40°$ *for 14 MeV,* $\sim 30°$ *for 20 MeV and* $\sim 18°$ *for 25 MeV protons.*

C^{6+} were detected on the CR39. The broad energy distribution of fully ionized carbon extended to 157 MeV (figure 6.4a). Both the cut-off value, i.e., the ion energy where the observed number of particles equals the noise level, as well as the spectral shape were closely reproduced when the laser polarization was changed to circular before the double plasma mirror by passing the beam through a KDP crystal operating as $\lambda/4$-waveplate. Owing to the stronger absorption of p-polarized components of laser light reflected from plasma, the target was irradiated by an elliptically polarized beam in this configuration. By use of 1D PIC-simulations the ellipticity, i.e. the ratio between the p- and s-polarized fraction of the laser electric field, could be estimated to a value of $\epsilon = 0.5$.

Comparing the spectra of C^{6+} for varying DLC-foil thicknesses from 50 nm down to 10 nm, a distinct maximum in cut-off energy was observed for irradiation of a 30 nm target (figure 6.4a). Here, the distribution reached up to 185 MeV. Lower charge states were detected at significantly reduced energies below 20 MeV, showing no noticeable dependence on target thickness. The proton spectra also exhibited an optimum at the foil thickness of 30 nm, reaching values of 35 MeV, while 50 nm and 10 nm gave 20 MeV and 11 MeV, respectively (figure 6.4b).

Clearly, at the time when this experimental study was carried out none of the existing analytical ion acceleration models was capable of predicting the obtained distinct optimum in ion energies at a foil thickness of 30 nm. Even qualitatively, the strong dependence of the resulting maximum ion energies on small, nm-scale changes of the initial foil thickness was not foreseen. As mentioned before, from multiparametric PIC simulations at shorter pulse durations and higher intensities

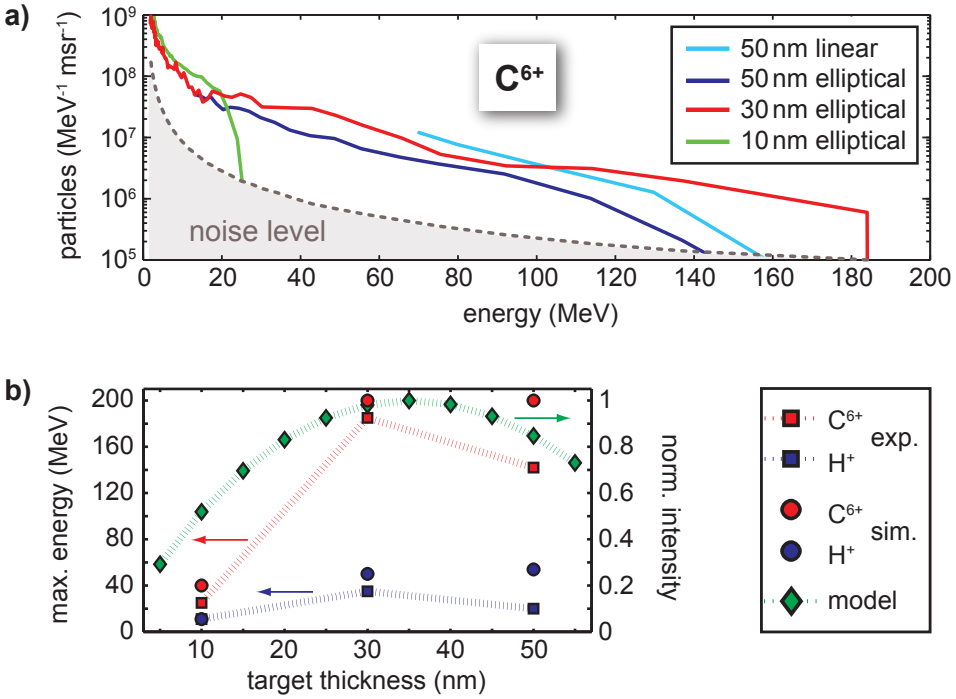

Fig. 6.4. *Observed spectra of fully ionized carbon ions (a) for foil thicknesses of 50, 30 and 10 nm. An optimum in acceleration is seen for the 30 nm target, in excellent agreement with maximum energies of C^{6+} and protons deduced from 1D PIC simulations (b). The normalized instantaneous laser intensity at burn-through time as derived from the presented analytical model (green diamonds) closely follows the cut-off energy curve.*

Esirkepov *et al.* found an empirical equation for the optimum normalized areal density $\sigma_{opt} \approx 3 + 0.4\, a_L$ [197]. However, at the empirically estimated thickness value of $d_{opt} \simeq 9\,\mathrm{nm}$ a drastic drop in ion energies was already observed in the experiment, where the optimum appears at about 3 times larger foil thicknesses. Thus, a more detailed theoretical investigation was needed.

6.3 PIC Simulations

To aid the understanding of the experimental findings, 1D and 2D PIC simulations at parameters matched with the presented experiment were carried out in collaboration with L. Yin and B. Albright of the X-1 Group, Applied Physics Division, LANL, employing the VPIC code [200]. Solid density (2.2 g/cm^3; $n_e/n_c = 660$) C^{6+} targets, 10 nm, 30 nm, and 50 nm thick mixed with 20% protons (in number density), are considered. Here, n_e stands for the electron density, whereas $n_c = \epsilon_0 m_e \omega_L^2 / e^2$ denotes the critical density of the plasma with electron mass m_e and laser carrier frequency ω_L. A linearly polarized pulse of intensity $I(t) = I_0 \sin^2(t\pi/\tau)$ with $I_0 = 7 \times 10^{19}$

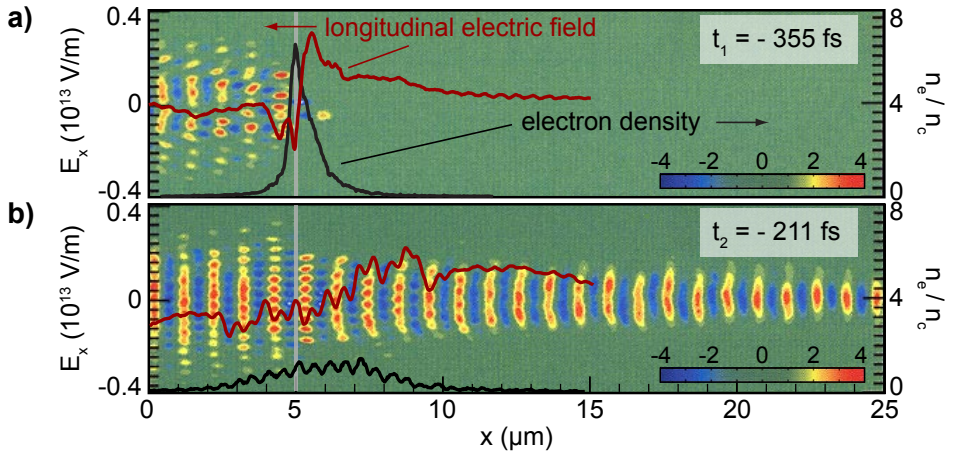

Fig. 6.5. *Electric field in y-direction as deduced from a 2D PIC simulation at times $t_1 = -355$ fs (a) and $t_2 = -211$ fs (b) before the peak of the laser pulse reaches the 10 nm target initially located at $x = 5\,\mu$m (color scale given in units of 10^{13} V/m). The black curve shows the normalized electron density n_e/n_{cr}, while the longitudinal electric field E_x is marked in red. Each quantity represents an average over 2 μm in transverse (z) direction around the focal spot center.*

W/cm^2 and $\tau = 1400$ fs (FWHM 700 fs) is used to model the TRIDENT laser. The simulation domain is 100 μm long in 1D and 50 μm in both laser (x) and transverse (z) direction in 2D. The cell size is $0.3\lambda_D^0$ with 167×10^3 particles per cell in 1D and $0.4\lambda_D^0$ along x and $1.6\lambda_D^0$ along z with 500 particles per cell in 2D (λ_D^0 is the initial Debye length; the initial electron temperature is $T_e = 165$ keV).

A comparison of 1D PIC simulation and experimental results on C^{6+} and proton cut-off energies is presented in figure 6.4b. For each foil thickness, the experimentally obtained maximum energies of both ion species are closely reproduced.

Calculating the collisionless skin depth, i.e. the decay length $l_s \simeq c/\omega_p$ of the evanescent field in the initially highly overdense plasma layer where ω_p is the Langmuir frequency $\omega_p = (n_e e^2/\epsilon_0 m_e)^{1/2}$, a value of $l_s \sim 6.2$ nm is obtained. Thus, even the thinnest, 10 nm DLC foil is opaque to the incident laser beam at the beginning of the interaction. However, the simulations show that within the laser pulse duration each of the three targets becomes relativistically transparent to the laser electric field eventually.

In figure 6.5, a 2D simulation of the 10 nm target case is used to demonstrate the effects of relativistic transparency. The black curve in figure 6.5a is the electron density n_e/n_c at a time $t_1 = -355$ fs prior to the peak of the pulse, when the laser beam has just penetrated the target. Up to this point in time, the target has expanded to a thickness comparable to the laser wavelength with a peak density $n_e/n_c \sim 6.8$. Accounting for relativistic effects, the peak density normalized over

the corrected critical density $n_e/(n_c\gamma) \sim 1$, where $\gamma \sim 6.8$ was obtained from the simulation as an average over electrons situated at the spatial location of the peak density, and the target becomes marginally underdense.

From this moment on the foil is no longer opaque but relativistically transparent to the laser beam. As a consequence, all electrons within the focal volume are directly driven by the penetrating laser field. In contrast to conventional TNSA where the electron dynamics at the rear surface of a thick and opaque target are considered purely thermal at all times, now the thermally expanding electron cloud is in addition collectively pushed in forward direction by the longitudinal component of the Lorentz force, giving rise to an enhanced charge separation field. Subsequently, rapid ion acceleration follows as the C^{6+} ions co-move with that localized, non-stationary enhancement in the electric field E_x, shown by the red curve in figure 6.5a.

This stage lasts approximately until the target thickness increases to several microns and the peak density n_e/n_c reduces to unity, as captured by the black curve in figure 6.5b. Owing to the drop in electron density and the thus decreased absorption, the co-propagating field enhancement breaks down around that classical transparency time t_2. During the time interval between t_1 and t_2, the carbon ions and protons gain the major fraction of their energy and reach their respective maximum of 40 and 11 MeV.

However, the 10 nm target becomes transparent to the laser at a time much before the laser intensity has evolved to its peak. Consequently, the short period of strong ion acceleration between times t_1 when the target becomes relativistically transparent ($n_e/(n_{cr}\gamma) \sim 1$) and t_2 when the electron density dropped to the critical density ($n_e/n_{cr} \sim 1$) takes place at the early rising edge of the laser pulse. Already at $t_2 = -211$ fs before the pulse maximum reaches the target, the acceleration of ions is terminated. This explains the observed low ion cut-off energies obtained from a 10 nm target as most of the laser pulse energy passes the foil after t_2, therefore not contributing to the acceleration.

On the other hand, the 50 nm target becomes transparent near the end of the laser pulse where the intensity has dropped already. The 30 nm target becomes transparent when the intensity is closer to the peak; in this case the transfer of laser energy into electric field energy between times t_1 and t_2 is maximized, resulting in the highest ion energies.

Figure 6.6 shows the spatial distribution of proton energies in two dimensions as resulting from the simulation of a 10 nm target and, in addition, the proton energies (blue curve) and the C^{6+} energies (red curve) at the focal spot center

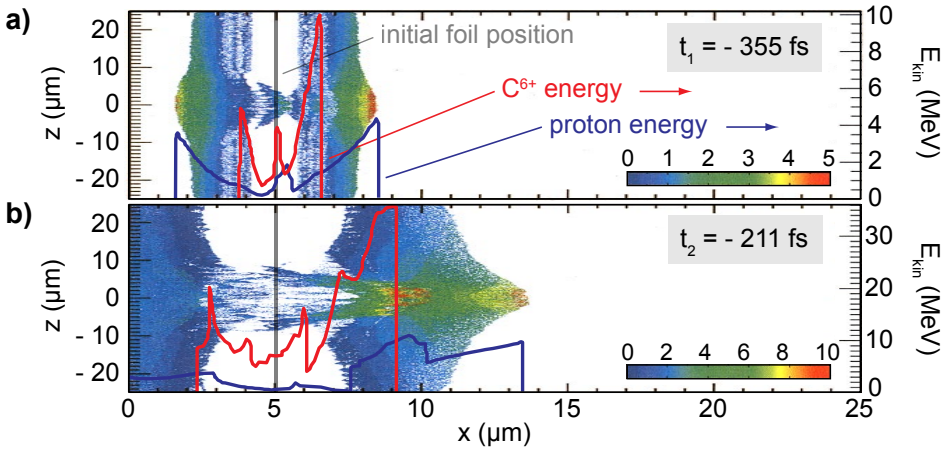

Fig. 6.6. *Two-dimensional spatial distribution of proton energies as seen in a 2D PIC simulation of a 10 nm foil at times $t_1 = -355$ fs (a) and $t_2 = -211$ fs (b) before the arrival of the main pulse at the target (color scale given in units of MeV). Overlaid are the proton energies (blue curve) and the C^{6+} energies (red curve) at $z = 0$.*

($z = 0$). Ions accelerated in forward direction obtain significantly higher energies than the ones moving backwards, with the component originating from the target back surface being dominant over the fraction from the front. This behavior can again be attributed to the longitudinal component of the Lorentz force pushing the heated and expanding electron cloud in forward direction as the laser penetrates the relativistically transparent target.

The observed asymmetry in the acceleration of ions stands in strong contrast to the recently published model of an adiabatic foil expansion as described in [201], where shorter pulses (< 100 fs) focussed to comparable intensities are considered, leading to a symmetric acceleration that happens primarily after the end of the laser pulse. While that model is certainly valid for short pulse irradiation at low intensities ($< 10^{19}$ W/cm^2) as studied previously, it obviously fails to explain the novel experimental results presented in this thesis.

Consequently, a new analytical approach was needed.

6.4 Analytical Model

In order to be able to guide future experimental design, a simple analytical model for the dynamics of the laser-driven target expansion was developed. The model is capable of forecasting the instantaneous laser intensity at the time t_1 when the target becomes relativistically transparent for a given set of laser and target parameters. As specified above, this "burn-through intensity" $I(t_1)$ needs to be maximized in

order to obtain the highest ion energies.

The model starts from the first law of thermodynamics, stating that the amount of energy dQ transfered to the system should be balanced by the sum of the change of internal energy dU and the pressure-volume work pdV

$$dQ = dU + pdV \tag{6.2}$$

Assuming that electrons are heated to a single temperature $T_e(t)$ that evolves in time, the correlation is rewritten as

$$\varepsilon\, I(t)\, dt \;=\; \frac{3}{2}\, n_{e0}\, L_0\, k_B\, dT_e \;+\; n_e(t)\, k_B\, T_e(t)\, dL \tag{6.3}$$

where the left-hand side represents the laser energy absorption into electrons with efficiency ε and instantaneous laser intensity $I(t)$. The first term on the right-hand side describes the resulting change in electron internal energy with initial foil thickness L_0, while the second includes the pressure-volume work due to longitudinal plasma expansion. A common factor of spot size area has been divided from all terms. In above equation, the plasma expansion is taken as purely 1D, which is a good approximation until the relativistic transparency time t_1 is reached. After t_1, 3D expansion would have to be taken into account. In addition, both radiative and conductive losses are neglected since lateral thermal conduction can generally be ignored for sub-micron target thicknesses and the radiative cooling time is of order $\sim 100\,\mathrm{ps}$, thus well exceeding the laser pulse duration.

Assuming a longitudinal self-similar plasma expansion at the ion sound speed

$$c_s = \sqrt{\frac{5}{3}\frac{Z\, k_B\, T_e(t)}{m_i}}, \tag{6.4}$$

i.e., that

$$n_e(t) \;=\; n_{e0}\, \frac{L_0}{L(t)}, \tag{6.5}$$

where the thickness $L(t)$ evolves as

$$L(t) = L_0 + \int_0^t dt' c_s(t'), \tag{6.6}$$

then $L(t)$ and $T_e(t)$ can be obtained numerically from a system of two nonlinear

ordinary differential equations

$$\frac{dL(t)}{dt} = c_s = \sqrt{\frac{5}{3}\frac{Z\,k_B\,T_e(t)}{m_i}} \tag{6.7}$$

$$\begin{aligned}\frac{dT_e(t)}{dt} &= \frac{2}{3}\frac{1}{k_B n_{e0} L_0}\left(\epsilon I(t) - n_e(t) k_B T_e(t)\frac{dL(t)}{dt}\right) \\ &= \frac{2}{3}\left(\frac{\epsilon I(t)}{k_B n_{e0} L_0} - \sqrt{\frac{5}{3}\frac{Z k_B}{m_i}}\frac{T_e(t)^{3/2}}{L(t)}\right).\end{aligned} \tag{6.8}$$

Burn-through of the target occurs at time t_1 when $n_e(t) \approx \gamma\, n_{\mathrm{cr}}$, where

$$\gamma \;=\; 1 \;+\; 3\,k_B T_e(t)\,/\,(2\,m_e\,c^2). \tag{6.9}$$

The instantaneous laser intensity (normalized to peak intensity) at burn-through time (i.e., $I(t_1)$) as derived from the model with $\varepsilon = 0.04$, which is low owing to the small target thicknesses used [196], has been overlaid in figure 6.4b for varying initial target thickness L_0. The dependency of the ion maximum energy on initial target thickness is closely reproduced by the corresponding burn-through intensity curve resulting from the model, thus verifying the direct connection between the two quantities. With given laser conditions, an optimal target thickness exists such that the laser pulse is near its maximum intensity at the time the target becomes transparent to the laser.

More details on the model can be found in [202]. Here, a refined approach is presented which includes the transition from 1D to 3D expansion at times larger than t_1. Despite the simplicity of the model and its shortcomings such as the ad hoc assumption of laser absorption or the instantaneous relaxation of the electron gas to a single, equilibrium temperature, it provides a first theoretical description of the dynamics of target heating and expansion and therefore gives insight into the main processes defining the optimum condition of enhanced ion acceleration in the regime of ultrathin, relativistically transparent targets. Moreover, the model is capable of predicting the optimum target thickness and density for a given set of laser parameters, hence proofing highly useful for follow-up experiments.

Building onto these first results, Yan, Tajima *et al.* recently reported a self-similar analysis of ion acceleration in the described regime [29, 203]. Named theory is rooted in the Mako-Tajima problem of 1984 considering collective ion acceleration by a reflexing electron beam [204], where an electron beam with delta-function energy spectrum centered around E_0 exits from a metallic surface into vacuum. Here,

the dependece of the resulting electron current density J on electron energy E is characterized by a power-law

$$J(E) = -J_0(1 - E/E_0)^{\alpha}. \tag{6.10}$$

This scenario exhibits similarities with the situation of laser-driven ion acceleration from ultrathin foils, where the laser heats and pushes a cloud of electrons out of the target. The authors fitted above function to the electron current density obtained from 1D PIC simulations around the optimum foil thickness and determined the index α, which is referred to as coherence parameter, to $\alpha \approx 3$. Tracking the evolution of electrons, ions and electrostatic field self-consistently in time, an expression for the maximum energy of accelerated ions of charge $q_i = Ze$ is obtained in its simplest form for short pulses and an ab initio transparent target

$$\mathcal{E}_{max} = (2\alpha + 1)ZE_0. \tag{6.11}$$

In the case of long pulses where thicker targets are optimal that are not transparent from the start, the authors follow the arguments of relativistic transparency and resulting strong ion acceleration between times t_1 and t_2 as given here. Treating the process again in self-similar fashion yields

$$\mathcal{E}_{max} = (2\alpha + 1)Z\overline{E_0}\left[(1 + \omega_L(t_2 - t_1))^{1/2\alpha+1} - 1\right], \tag{6.12}$$

where the characteristic electron energy $\overline{E_0}$ is evaluated over the time interval (t_1, t_2) and a laser pulse duration of $2\tau > t_1, t_2$ is assumed. By use of this semi-analytical approach, the authors achieve good agreement with the experimental results presented here.

6.5 Increasing the Intensity

As a part of my PhD work, a follow-up series of measurements was carried out at the upgraded TRIDENT facility delivering increased peak intensities. The above described lead-off campaign relied on a double plasma mirror setup to suppress ASE and prepulses and thus ensure interaction with an ultrahigh contrast laser pulse, however giving rise to energy losses of around $\sim 45\%$. For the subsequent experiment, the TRIDENT frontend was redesigned to incorporate idler generation in a short-pulse pumped OPA stage [146]. An in-depth description of the upgraded

frontend type 1 is presented in section 3.2.3. Thus, the use of plasma mirrors became obsolete and the mentioned energy losses were avoided. Consequently, energies of $\sim 90\,\mathrm{J}$ at high contrast on target were achieved. In addition to making plasma mirrors dispensable, in the upgrade the pulse duration was successfully narrowed down further, yielding $\sim 550\,\mathrm{fs}$ as compared to the previous value of $\sim 700\,\mathrm{fs}$. By virtue of those measures, the resulting peak intensity on target could be increased to $\sim 2 \times 10^{20}\,\mathrm{W/cm^2}$.

While the DLC foils of the first TRIDENT campaign were fabricated by V. Liechtenstein at Kurchatow Institute in Moscow using a modified glow discharge technique, for the follow-up measurements DLC targets could be produced for the first time at the newly established target fabrication laboratory at LMU employing cathodic arc deposition. For details on the respective target fabrication method refer to section 4.1.2. With cathodic arc deposition, the DLC foils exhibit a higher fraction of sp^3 bonds amounting to $\sim 75\%$, and consequently also higher density of $2.7\,\mathrm{g/cm^3}$. Self-suporting targets of thicknesses spanning from 2.5 nm up to 58 nm were successfully manufactured. Thus, a broader range of target parameters was available for investigation in the second campaign. Foils thicker than $\sim 60\,\mathrm{nm}$ turned out to be mechanically unstable, owing to internal stress in the material arising from the deposition process.

The damage threshold of DLC was tested at TRIDENT upon controlled irradiation with an attenuated 1.2 ns pulse simulating the extended ASE pedestal and a 500 fs pulse modeling short prepulses. Target degradation was observed at respective intensities ratios of $\sim 2 \times 10^{-12}$ and $\sim 5 \times 10^{-10}$ in relation to the peak intensity on a full system shot, giving an estimate of the contrast on target employing the new OPA frontend. On actual target shots, a full aperture backscatter (FABS) diagnostic was used to monitor light backscattered from the foil surface and thus ensure target integrity on interaction with the main pulse [205].

Two Thomson parabola spectrometers were employed, one orientated along target normal, the second located at an angle of 8.5° orthogonal to the laser polarization direction. For characterization of the proton beam profile detector stacks composed of RCF and CR39 were used. In addition, a magnetic electron spectrometer was placed at an angle of 6.5° orthogonal to the laser polarization direction. All diagnostics were operated in parallel in single-shot mode.

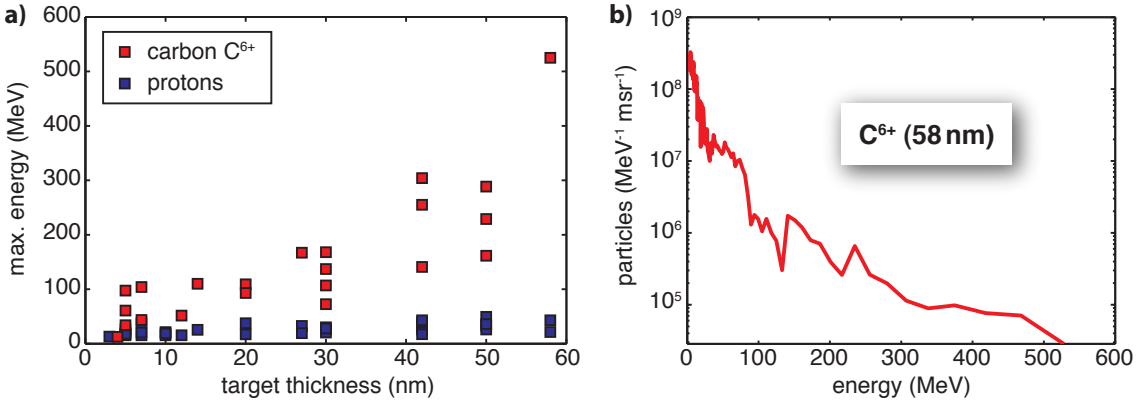

Fig. 6.7. *(a) Maximum proton (blue squares) and carbon C^{6+} (red squares) ion energies over target thickness observed at increased intensities of 2×10^{20} W/cm^2. The data shown was obtained from a Thomson parabola spectrometer placed at an angle of 8.5° with respect to target normal, orthogonal to the laser polarization. As expected by the developed analytical model, the optimum foil thickness shifts to larger values. Using a 58 nm thick target, the measured carbon C^{6+} ion spectrum extended beyond 0.5 GeV (b), representing the current world record for a laser-driven accelerator.*

6.5.1 Measured Ion Beams

From the analytical model specified above, the optimum foil thickness for maximizing the energy of accelerated ions is expected to be shifted to larger values of ~ 80 nm due to the increase in intensity [202]. Indeed, at the upgraded laser parameters of ~ 90 J pulse energy, ~ 550 fs pulse duration and $\sim 2 \times 10^{20}$ W/cm^2 peak intensity the largest ion energies were experimentally observed at the maximum available target thickness of 58 nm (see figure 6.7a). Here, the spectrum of fully ionized carbon reached out all the way up to 525 MeV, while the proton cut-off energy amounted to 43 MeV. The corresponding C^{6+} ion spectrum is illustrated in figure 6.7b. This result represents the current world record in carbon ion energies generated via laser-driven acceleration, superseding the all-time high of 185 MeV C^{6+} presented beforehand and by far outreaching the previous top mark of ~ 40 MeV for carbon C^{5+} seen at TRIDENT [5].

For targets as thin as 5 nm, the measured carbon C^{6+} ion energies are down by around one order of magnitude with respect to the optimum. However, for such thin foils a distinct quasi-monoenergetic electron spectrum peaked at an energy of 30 MeV was observed [97]. This might be a first experimental indication of the generation of highly dense electron bunches as predicted in theory when the laser ponderomotive force exceeds the restoring force of the induced charge separation field [95, 96].

6.6 Summary and Conclusion

In summary, experimental results on proton and carbon ion acceleration from ultrathin DLC foils of 50, 30 and 10 nm thickness are presented [41]. A distinct maximum in the ion cut-off energies is observed using a 30 nm target. Compared with conventional TNSA, which is dominant for opaque foils, the acceleration of ions is drastically enhanced, resulting in unprecedented C^{6+} cut-off energies up to 185 MeV. This increase is attributed to a large longitudinal electric field, generated by strong volumetric energy transfer to electrons in the bulk when self-induced transparency enables the laser beam to penetrate the target; moreover, this localized field co-moves with the C^{6+} ions, resulting in rapid ion acceleration [199]. In previous work, a lower limit for the foil thickness was imposed by the shock wave generated from imperfect laser contrast. Here, it is demonstrated for the first time experimentally that such a limit also exists when high-contrast pulses are used because target transparency arises before the peak intensity of the laser pulse, resulting in a lower longitudinal field and decreased total absorption. This major outcome is understood within a simple analytical model of the target evolution from opaque to relativistically underdense as the foils electrons are heated and expand, capable of predicting the optimum condition for a given set of laser parameters in future experiments.

In a follow-up campaign, the TRIDENT peak intensity was increased to $2 \times 10^{20}\,\mathrm{W/cm^2}$, resulting in a shift of the optimum foil thickness to larger values as expected by the model. For a target thickness of 58 nm, carbon C^{6+} ions of energy beyond 0.5 GeV were observed, representing the current world record obtained from a laser-driven accelerator.

Chapter 7

Radiation Pressure Dominated Acceleration of Ions

In the previous chapter, ion acceleration from ultrathin DLC foils irradiated by comparably long laser pulses (500 fs - 700 fs FWHM) was discussed. It was found that ions gain the majority of their energy during a short period starting at time t_1, when the target becomes relativistically transparent, and ending at t_2, when the foil density drops below the classical critical density n_c. In order to optimize the energy of ions, the foil thickness has to be chosen such that the instantaneous laser intensity within this time interval of strong ion acceleration is maximized.

As demonstrated in chapter 6, this condition implies that a longer pulse duration calls for a thicker target when compared to a shorter pulse at equal peak intensity to account for target expansion and heating on the extended rising edge of the laser field amplitude. Consequently, the experimentally observed optimum thickness is larger than predicted by the empirical scaling law for the normalized electron areal density $\sigma_{opt} \approx 3 + 0.4\, a_L$ derived by Esirkepov *et al.* [197].

Shorter pulses are hence needed, in order to access the stage of enhanced ion acceleration when the target turns into transparent more directly. For shorter pulses, the amount of foil expansion and heating prior to the pulse peak is reduced. Thus, the optimum foil thickness is expected to be closer to the predictions of the empirical condition given above.

Moreover, it is important to note that the named empirical scaling law is practically identical to the optimum condition for phase stable acceleration of ions driven by the laser radiation pressure (see equation 2.51),

$$\sigma_{opt} \simeq a_L \tag{7.1}$$

While for use of linear polarization in the discussed intensity range ion acceleration is still largely dictated by the expansion of highly energetic, hot electrons, a transition to a radiation pressure dominated regime was hoped to be observed when changing the laser polarization to circular [90, 92, 94, 98, 99, 101, 102, 107].

As specified in section 2.5.3, for RPA to become dominant a thin foil is irradiated by a circularly polarized laser pulse at normal incidence. Owing to the absence of an oscillating component in the $\vec{v} \times \vec{B}$ force, electron heating is strongly suppressed. Instead, electrons are compressed to a highly dense electron layer piling up in front of the laser pulse which in turn accelerates ions. By choosing the laser intensity, target thickness and density such that the radiation pressure equals the restoring force given by the charge separation field, the whole focal volume eventually propagates ballistically as a quasi-neutral plasma bunch, continuously gaining energy from the laser field. In this scenario, all particle species are accelerated to the same velocity, which intrinsically results in a monochromatic spectrum. As long as the electron temperature is kept low, a phase-stable acceleration can be maintained, and the process is expected to lead to very high conversion efficiencies and ion energies scaling linearly with laser intensity under optimum conditions.

The possibility to accelerate quasi-monoenergetic ion bunches has already been demonstrated within the TNSA-regime by restricting the ion source to a small volume where the sheath field is homogenous [5, 20, 21]. However, this method suffers from a very low conversion efficiency.

Despite the anticipated highly promising characteristics of RPA, experimental investigation of ion acceleration using circular polarization has only been carried out at intensities smaller than $4 \times 10^{18}\,\mathrm{W/cm^2}$ and targets of several micron thickness irradiated at oblique incidence [206, 207], thus being far off the parameters necessary for radiation pressure to become the dominant acceleration mechanism.

In this chapter, unprecedented experimental studies of ion acceleration driven by circularly polarized laser pulses at significantly increased intensities of $5 \times 10^{19}\,\mathrm{W/cm^2}$ are presented, corresponding to a radiation pressure of $\sim 30\,\mathrm{Gigabar}$. Diamond-like carbon (DLC) foils of thickness $2.9 - 40\,\mathrm{nm}$ have been irradiated at normal incidence and ultra-high laser pulse contrast. When compared to the case of linear polarization, a pronounced decrease in the number of hot electrons is observed. While for linear polarization the spectra of all ion species decay monotonically up to a certain cut-off value, a distinct peak of energy 30 MeV emerges in the spectrum of fully ionized carbon ions at the optimum target thickness of $(5.3 \pm 1.3)\,\mathrm{nm}$ and circular polarization. Two-dimensional PIC simulations confirm, that under these conditions C^{6+} ions are for the first time dominantly accelerated by the laser radiation pressure

at values up to $\sim 10^{21}\,\mathrm{m/s^2}$. The obtained results are published in Physical Review Letters [42].

7.1 Experimental Setup

The described experiments have been carried out in collaboration with the group of Prof. W. Sandner at the 30 TW Ti:sapph laser system located at Max Born Institute, delivering 1.2 J of energy stored in pulses of $\tau_L = 45\,\mathrm{fs}$ FWHM duration at a central wavelength of $\lambda_L = 810\,\mathrm{nm}$. An in-depth description of the facility is given in section 3.7. The relative intensity of prepulses and of the amplified spontaneous emission (ASE) pedestal was characterized by means of a 3rd order autocorrelator to be smaller than 10^{-7} at times earlier than $-10\,\mathrm{ps}$ prior to the arrival of the main peak (figure 3.8a). In order to further enhance that value, a re-collimating double plasma mirror [142, 208] was introduced into the laser beam path, resulting in an estimated contrast of $\sim 10^{-11}$. Taking into account the measured 60% energy throughput of this setup, $\sim 0.7\,\mathrm{J}$ were focussed by an f/2.5 off-axis parabolic mirror to a FWHM diameter focal spot size of $2w_0 = 3.6\,\mu\mathrm{m}$. A peak intensity of $I_0 = 5 \times 10^{19}\,\mathrm{W/cm^2}$ was achieved, corresponding to a normalized laser vector potential maximum of $a_0 = 5$ for linear and $a_0 = 5/\sqrt{2} = 3.5$ for circular polarization. To vary the laser polarization to circular, a mica crystal operating as $\lambda/4$-waveplate was introduced into the beam path behind the plasma mirror setup.

DLC foils of thickness $d = 2.9 - 40\,\mathrm{nm}$ and density $\rho = 2.7\ \mathrm{g/cm^3}$ were placed in the focal plane at normal incidence. The targets were produced by cathodic arc deposition, resulting in a high fraction of $\mathrm{sp^3}$-, i.e. diamond-like bonds of ∼75%. The thickness of the DLC foils was characterized by means of an atomic force microscope (AFM), including the hydrocarbon contamination layer on the target surface which was present during the experiments. In addition, the depth-dependend composition of the target was measured via Elastic Recoil Detection Analysis (ERDA), yielding a thickness of $\sim 1\,\mathrm{nm}$ for the hydrocarbon contamination layer. Throughout the thesis, given foil thicknesses are referring to the combined thickness of bulk and surface layer as it appears in the actual ion acceleration experiments presented. More details on target fabrication and characterization can be found in chapter 4, section 4.1.2.

To characterize the accelerated ions, a Thomson parabola spectrometer was placed at a distance of $\sim 0.5\,\mathrm{m}$ (solid angle $\sim 1.14 \times 10^{-7}\,\mathrm{sr}$) along the laser propagation, i.e target normal direction. Ion traces were detected at the back of

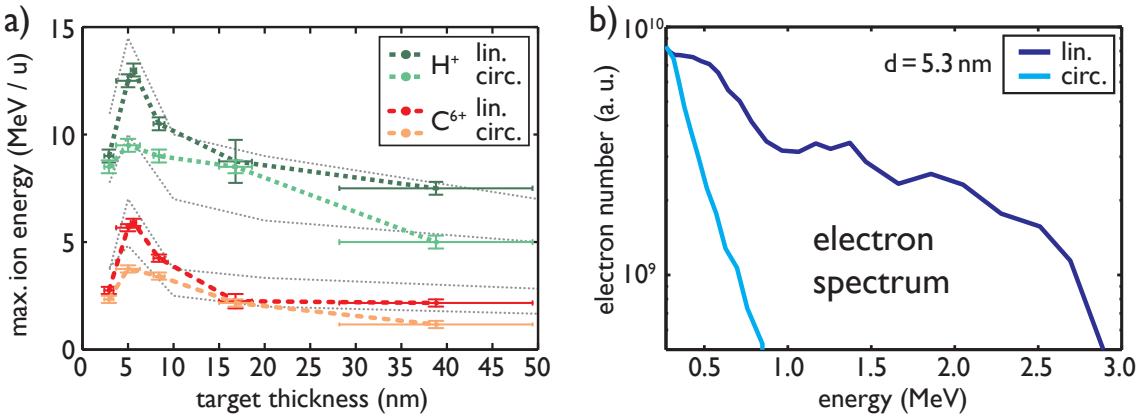

Fig. 7.1. *(a) Experimentally observed maximum proton (green dotted line, light green dotted line) and carbon C^{6+} (red dotted line, orange dotted line) energies per atomic mass unit over target thickness for linearly and circularly polarized irradiation. Grey dotted lines represent the respective values obtained from 2D PIC simulations. Corresponding electron spectra measured at the optimum target thickness $d = 5.3\,\mathrm{nm}$ are given in (b), showing a strong reduction in electron heating for circularly polarized irradiation.*

the spectrometer by a CCD camera coupled to a micro-channel plate (MCP) with phosphor screen [181]. In addition, a magnetic electron spectrometer (solid angle $\sim 2 \times 10^{-4}\,\mathrm{sr}$) equipped with Fujifilm BAS-TR image plates was positioned behind the target at an angle of 22.5° with respect to the laser axis.

7.2 Measured Ion Beams

The obtained maximum ion energies per atomic mass unit plotted over target thickness d are shown in figure 7.1a for linear and circular polarization. While linearly polarized irradiation yields higher proton and carbon energies, a strong dependence on initial foil thickness is visible in both cases, with a distinct optimum at $d = 5.3\,\mathrm{nm}$. It is found, that the corresponding value of the normalized electron areal density of $\sigma \simeq 3.3$ is closely consistent with the the prediction of the empirical scaling law for linear laser polarization $\sigma_{opt} \simeq 3 + 0.4a_0 = 5$ [197]. The experimentally observed conformance is contrary to case of long pulse irradiation (chapter 6), where targets thicker than the foreseen optimum are required to compensate for electron heating and expansion on the extended rising edge of the pulse.

As discussed earlier, using circular polarization the value of the optimum foil thickness is theoretically expected to be given by the similar condition $\sigma_{opt} \simeq a_0$ [98]. This prevision is in excellent agreement with the experimentally observed result of $3.3 = \sigma \simeq a_0 = 3.5$.

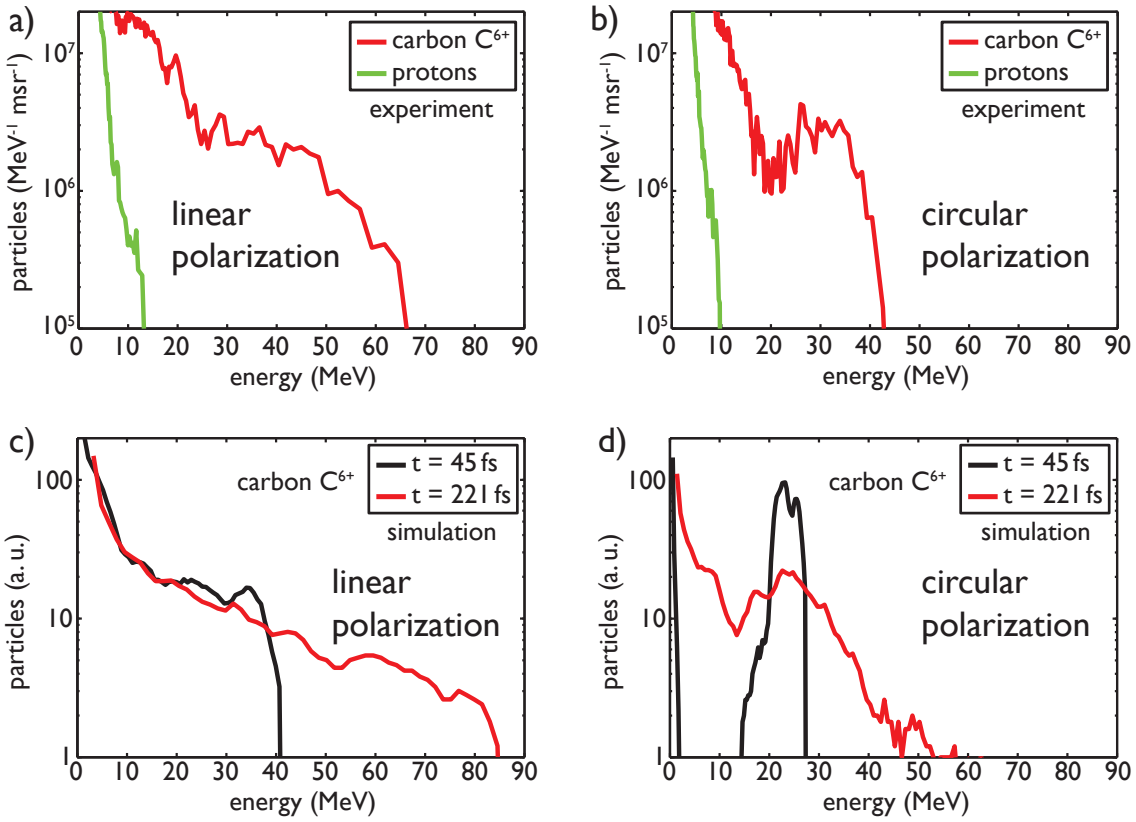

Fig. 7.2. *Experimentally observed proton (green curves) and carbon C^{6+} (red curves) spectra in case of linear (a) and circular (b) polarized irradiation of a 5.3 nm thickness DLC foil. The corresponding curves as obtained from 2D PIC-simulations (c,d) show excellent agreement with the measured distributions at late times (red curves, $t = 221$ fs after the arrival of the laser pulse maximum at the target). A quasi-monoenergetic peak generated by radiation pressure acceleration is revealed for circular polarization, which is still isolated at the end of the laser-target interaction (black curve, $t = 45$ fs).*

At the optimum target thickness, maximum energies for protons and carbon ions of 10 MeV and 45 MeV are generated for circular polarization, while linear polarization gives 13 MeV and 71 MeV, respectively. The corresponding electron spectra for $d = 5.3$ nm are shown in figure 7.1b. It can be clearly seen, that circularly polarized irradiation results in a pronounced reduction in the number of highly energetic electrons as expected.

To illustrate the consequent impact on the acceleration of ions, experimentally observed proton and carbon spectra are plotted in figure 7.2a,b for linear and circular polarization at the optimum foil thickness. A monotonically decaying spectrum is obtained for both protons and carbon ions in case of linear polarization. In contrast, when the laser polarization is changed to circular the spectrum of fully ionized carbon C^{6+} atoms (fig. 7.2b) reveals two components.

In addition to the continuously decreasing low energetic ion population reaching up to $\sim 20\,\mathrm{MeV}$ a distinct peak is seen at higher energies, centered around 30 MeV. A conversion efficiency of $\sim 2.5\,\%$ to C^{6+} ions within the peak energy interval $20 - 40\,\mathrm{MeV}$ and a beam of half angle $\sim 9°$ is deduced, in good agreement with the corresponding value predicted by [94] (refer to section 2.5.3, equation 2.52)

$$\eta = \frac{v_f}{c} = \frac{2 I_0 \tau_L}{c^2 \rho\, d} \simeq 3.7\,\%. \tag{7.2}$$

As mentioned earlier, in a publication by Hegelich *et al.* that appeared in Nature in 2006 [5], quasi-monoenergetic carbon C^{5+} ion beams at a nearly identical apex energy of 35 MeV were reported from an experiment within the regime of TNSA by employing a reduced source volume of ions. However, while [5] measured $\sim 1 \times 10^7$ particles/msr within an energy spread of $\frac{\Delta E}{E} = 17\%$ employing a laser pulse of energy 20 J, here about 50% more particles within the same spread at a pulse energy of only 0.7 J are obtained, corresponding to a more than 40 times increase in conversion efficiency.

The spectral spike of C^{6+} ions was repeatedly observed in consecutive shots at the optimum foil thickness of 5.3 nm and circular polarization, whereas the shape of the proton spectrum was not affected when varying the polarization. For protons, only the cut-off energy shifts to a slightly smaller value of $\sim 10\,\mathrm{MeV}$.

7.3 PIC Simulations

In order to support the experimental findings, two-dimensional particle-in-cell (PIC) simulations were carried out in collaboration with X. Q. Yan. The DLC foil targets were modeled by a solid density ($n_e/n_c = 500$), rectangularly shaped plasma slab of zero initial electron temperature, composed of 90% C^{6+} ions and 10% protons in number density. The laser pulse is of Gaussian shape in both the spatial distribution in the focal plane as well as in time, with a FWHM diameter of $4\,\mu$m and a FWHM duration of 45 fs, resulting in a peak intensity of $I_0 = 5 \times 10^{19}\,\mathrm{W/cm^2}$. A simulation domain of size 10μm in transverse (y) and 20μm in longitudinal (x) dimension was used, subdivided into a grid of 1200×10000 cells each occupied by 2000 particles. In the following, PIC simulation times are given relative to $t = 0$, when the peak of the laser pulse reaches the initial position of the target ($x = 3\lambda_L$).

The calculated carbon spectra are presented in figure 7.2c,d for linearly and circularly polarized irradiation. To account for the small solid angle of observation of the Thomson parabola spectrometer, only particles propagating in forward

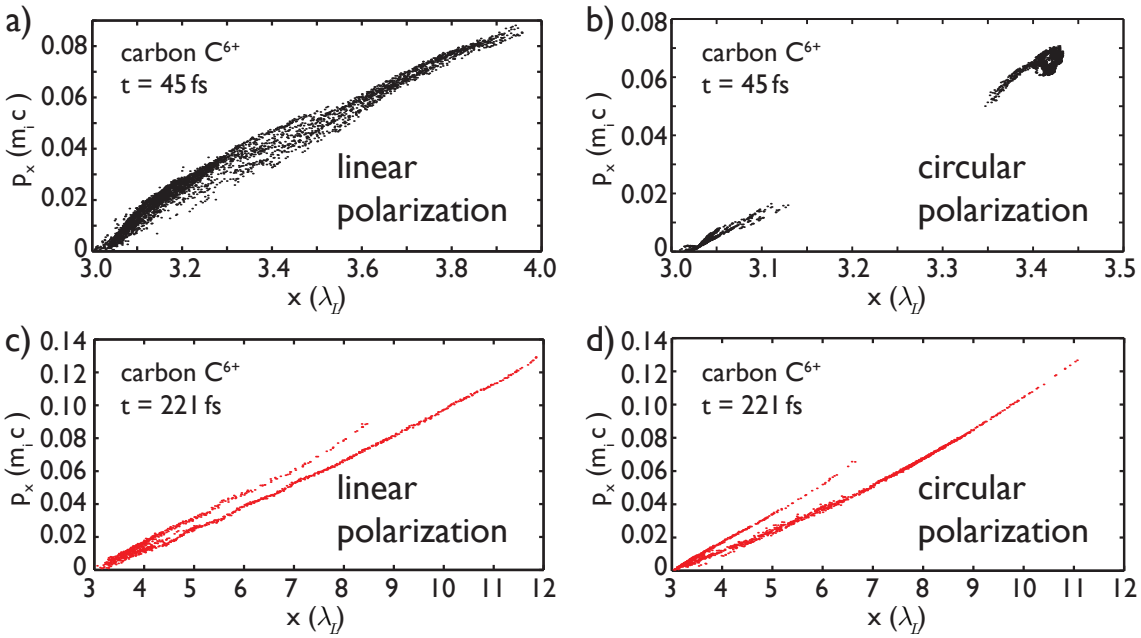

Fig. 7.3. *(a,b) Carbon ion phase space at the end of the laser-target interaction (black curves, $t = 45$ fs). A significant amount of particles forms distinct loops in case of circular polarization (b), giving evidence of a phase-stable acceleration driven by the laser radiation pressure. At late times (red curves, $t = 221$ fs), the characteristic phase space rotation disappears, indicating that phase-stable acceleration breaks down (d).*

direction within a cone of half angle 0.01 rad were considered for the simulated graphs. A continuously decaying spectrum is generated in case of linear polarization, which agrees well with the experimental result (figure 7.2a,c). This scenario changes drastically when circular polarization is used. As shown in figure 7.2d, an isolated, quasi-monoenergetic peak emerges in this configuration at the end of the laser-target interaction (black, $t = 45$ fs).

In the carbon ion phase space (figure 7.3b), a significant amount of particles is located in a discrete area, constituting a rotating structure. The series of loops originates from the continuing front side acceleration and the ballistic evolution of the target, thus giving clear evidence of radiation pressure to be the dominant acceleration force ([90, 92, 94, 98, 99, 101, 102, 107], see section 2.5.3 for details on the phase stable acceleration process). This is in strong contrast to the use of linear polarization, where at that moment the carbon ion phase space already forms a continuous, straight line (figure 7.3a).

The striking difference in the acceleration dynamics can also be directly inferred when examining the electron and ion density distributions as observed in described simulations (see figure 7.4). For use of circular polarization, the electron population

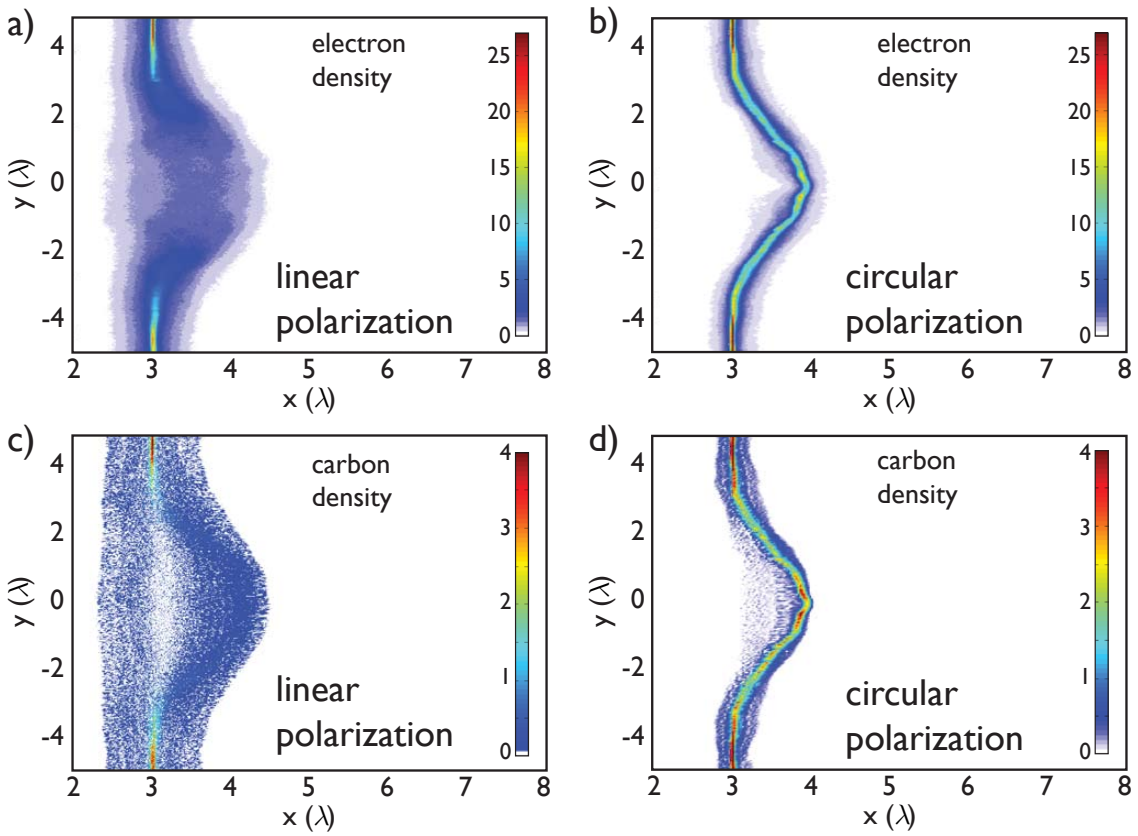

Fig. 7.4. *Cycle-averaged electron (a,b) and carbon ion (c,d) density at $t = 61\,fs$ after the peak of the laser pulse reached the $5.3\,nm$ target initially located at $x = 3\lambda$. While linear polarization results in strong expansion of the target caused by hot electrons, for circularly polarized irradiation the foil is accelerated as a dense, quasi-neutral plasma bunch.*

maintains its structure as a thin layer of high density being pushed by the laser in forward direction. As a consequence, carbon ions co-propagate with the compressed electron cloud and the whole focal volume is accelerated as a quasi-neutral dense plasma bunch by the laser radiation pressure. Since all ion species move at equal velocity, RPA-driven protons attain only $30/12 = 2.5\,MeV$ energy, thus not being visible in the continuous experimental spectrum reaching up to $\sim 10\,MeV$ (figure 7.2b).

This scenario is contrary to the case of linear polarization (figure 7.4a,c), where the foil electrons are heavily heated by the laser. Accordingly, electrons have already spread significantly and the electron density in the focal spot center, where electrons gain their highest energies, is considerably reduced. Although the acceleration of carbon ions is still asymmetric, favoring the laser forward direction (see also [41], chapter 6), it is dominated by the sheath field of the expanding electrons.

However, given the laser parameters used in the presented experiment, the nar-

row isolated quasi-monoenergetic peak in the carbon spectrum as it is present right after the end of laser-target interaction does not preserve its shape upon further propagation of the ion beam (figure 7.2b,d). Even though the apex energy stays constant, the spectral distribution broadens and partially merges with the low energetic ion population which at this point still gains energy, resulting in the carbon ion spectrum as observed experimentally. Simultaneously, the characteristic ion phase space loops disappear, indicating that phase-stable acceleration breaks down at late times (figure 7.3d).

This behavior can be attributed to the considerable deformation of the foil plasma by the tightly focussed gaussian laser spot (figure 7.4b,d). Owing to the thus no longer normal but rather oblique incidence on the bent plasma surface, particularly at the end of the laser-target interaction, perpendicular electric field components are present. Those efficiently heat electrons located in the warped spatial regions, which then quickly spread around the target, causing the mono-energetic peak in the carbon spectrum to broaden as well as ions in the low energetic part of the distribution to gain further energy and close the gap to the RPA-generated population. Moreover, as the electron energy rises the thin, compressed layer of cold electrons co-moving with ions, which is a crucial requirement for phase-stable acceleration, can no longer be maintained and the RPA process terminates.

One should note that this temporal evolution of the foil plasma shape was already discussed theoretically in [94], where in order to prevent the distortion of the ion spectrum an upper limit for the laser pulse duration is given by

$$t_{max} \simeq \sqrt{2 w_0 c \rho d / I_0} = 176\,\mathrm{fs}. \tag{7.3}$$

Even though the laser pulse duration used in the presented experimental study is significantly shorter than t_{max}, a spectral deformation is still observed, taking place after the end of the laser-target interaction.

7.4 Summary/Conclusion/Outlook

In summary, experimental investigations on ion acceleration from nm-thin DLC foil targets irradiated by linearly and circularly polarized, highly intense, short laser pulses are presented. A strong decrease in the number of hot electrons was observed for use of circular polarization, resulting in a pronounced peak centered at 30 MeV in the carbon C^{6+} ion spectrum at the optimum foil thickness of 5.3 nm, which is in excellent agreement with the condition $a_0 \simeq \sigma$ [98]. Compared to [5], a more

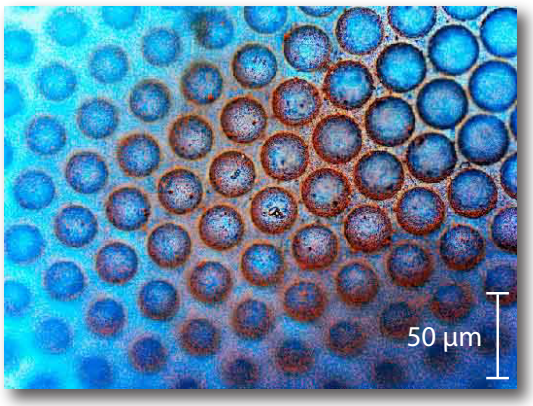

Fig. 7.5. *Microscopic image of a prototype for future shaped DLC targets. The pre-curved 10 nm thin foil is freestanding, with a radius of curvature of 34 µm of each hemisphere. (by courtesy of P. Hilz, LMU)*

than 40 times increase in conversion efficiency is demonstrated when considering an identical energy spread around the apex. 2D PIC-simulations have been carried out, giving clear evidence that those ions are for the first time dominantly accelerated in a phase-stable way by the laser radiation pressure. While linear polarization gives rise to the generation of a large number of highly energetic electrons, causing the target plasma to expand rapidly, in case of circular polarization electrons and ions co-propagate as a dense, quasi-neutral plasma bunch over the whole duration of the laser pulse.

Being recently widely studied in theory, the comparative measurements of this PhD work provide the first experimental proof of the feasibility of radiation pressure acceleration to become the dominant mechanism for ion acceleration when circular polarization is used. These results are a major step towards highly energetic, monochromatic ion beams generated at high conversion efficiencies as demanded by many potential applications. Those include fast ignition inertial confinement fusion (ICF) [36, 37] as well as oncology and radiation therapy [29].

In follow-up experiments planned for the near future, the observed spectral deformation might be successfully compensated for by properly shaping the laser focal spot distribution [105] and/or the nm-thin foil target [106]. Here, the latter publication discusses a planar foil target of radially varying density to balance the spatially varying laser electric field amplitude in the focus. However, in practice it turns out that fabrication of such foils is highly challenging and currently not within reach using the methods of DLC foil fabrication as described in section 4.1.2. A promising alternative approach might be to employ a pre-curved target. This idea builds

a bridge to the experiments on ion acceleration from the front surface of spherical targets presented in chapter 5, where a convex surface was applied to generate a closer-to-planar acceleration front of ions. In a first try, self-suporting, 10 nm thin DLC foils of hemispherical shape were successfully produced by cathodic arc deposition. A microscopic image of these prototypes is depicted in figure 7.5.

Additionally, increasing the intensity to $7 \times 10^{21}\,\mathrm{W/cm^2}$ is expected to result in a stabilization of the mono-energetic feature due to plasma instabilities [109], while beyond $10^{23}\,\mathrm{W/cm^2}$ RPA is predicted to become dominant even for linear polarization with a laser-to-ion conversion efficiency approaching unity in the highly relativistic limit [89].

Chapter 8

ATLAS-Driven Short Pulse Pumped OPCPA

In order to build upon the accomplished novel results on laser-driven ion acceleration presented in the last three chapters and eventually be able to compete with conventional particle accelerators, further advances in high-intensity laser technology are a key requirement. In particular, compact systems operating at high repetition rates are needed, capable of producing ultra-high contrast short pulses with a steep rising edge that are focusable to ultra-high peak intensities. A promising technique to achieve those demanding prerequisites is optical parametric amplification (OPA, see section 3.1.4 for an introduction to the basic concepts).

This chapter will present advances on short pulse pumped ultrabroadband noncollinear optical parametric chirped-pulse amplification (SPP-OPCPA) that have been accomplished as part of my PhD work [43]. Those findings represent an important step towards the Petawatt Field Synthesizer (PFS) project that is currently being pursued by our group at MPQ [44], aiming for an energy of 5 J stored in pulses as short as 5 fs.

8.1 Motivation for SPP-OPCPA

In typical ultra-broadband high-intensity OPCPA setups the duration of pump pulses obtained from a Nd:YAG laser are mostly on the order of 100 ps [120–122, 209]. Using shorter pump pulses of $\sim$ 100 fs, sub-10 fs pulse durations were successfully generated, but prior to the work presented here the resulting energies were limited to the microjoule range [117–119, 127, 210, 211]. Output pulse energies of 300 μJ have been reported from an OPCPA system pumped by pulses of 150 fs

[212], the signal pulse duration however was about 20 fs.

Despite being put into practice only on rather small-scale systems before this study, OPCPA pumped by short pulses offers great potential for boosting the output pulse energy up to the Joule level while keeping the shortest pulse durations. As compared to conventional laser amplifiers or long-pulse-pumped OPCPA, the conditions for the generation of ultra-short high-power pulses are improved in a number of different aspects. Firstly, the short pump duration reduces the stretching factor for the seed pulse, thereby increasing stretching and compression fidelity and allowing for the use of simple, high throughput stretcher-compressor pairs, e.g. a block of glass and a set of chirped multilayer mirrors. Secondly, the significantly increased pump power provides sufficient gain even in very thin OPA crystals, implying an increase of amplification bandwidth as compared to OPA driven by longer pulses. Finally, unwanted signal background arising from parametric superfluorescence is effectively narrowed down to the short amplification time window of the pump pulse duration. Hence, a dramatically enhanced pulse contrast is achieved outside this window. Such ultra-high intensity pulses at ultra-high contrast are a crucial prerequisite for a multitude of laser-plasma interaction studies, especially in experiments focussing on particle acceleration from ultra-thin foils as presented in chapters 6 and 7.

In this chapter, first experimental results verifying the scalability of the SPP-OPCPA concept to higher power levels are presented. The proof-of-principle study drew on the ATLAS TW-scale Ti:sapphire CPA laser (refer to section 3.2.1 for details on ATLAS) for both seeding and pumping an OPCPA stage. This optical synchronization was essential as on the pulse duration timescale of < 100 fs no electronic method could have provided sufficient accuracy. The strict requirements on femtosecond-scale synchronization of the OPA process were still met even after propagating the two beams along path lengths of about 20 m before overlapping them in the OPA crystal.

8.2 Experimental Setup

Figure 8.1 illustrates the layout of the system. The seed beam was provided by inserting a glass plate into the uncompressed ATLAS beam just before the compressor chamber to split off a small fraction of the pulse energy. Those pulses were subsequently compressed from ~ 350 ps down to ~ 43 fs in a separate grating compressor set up in air. To supply the required ultrabroad seed bandwidth, the compressed

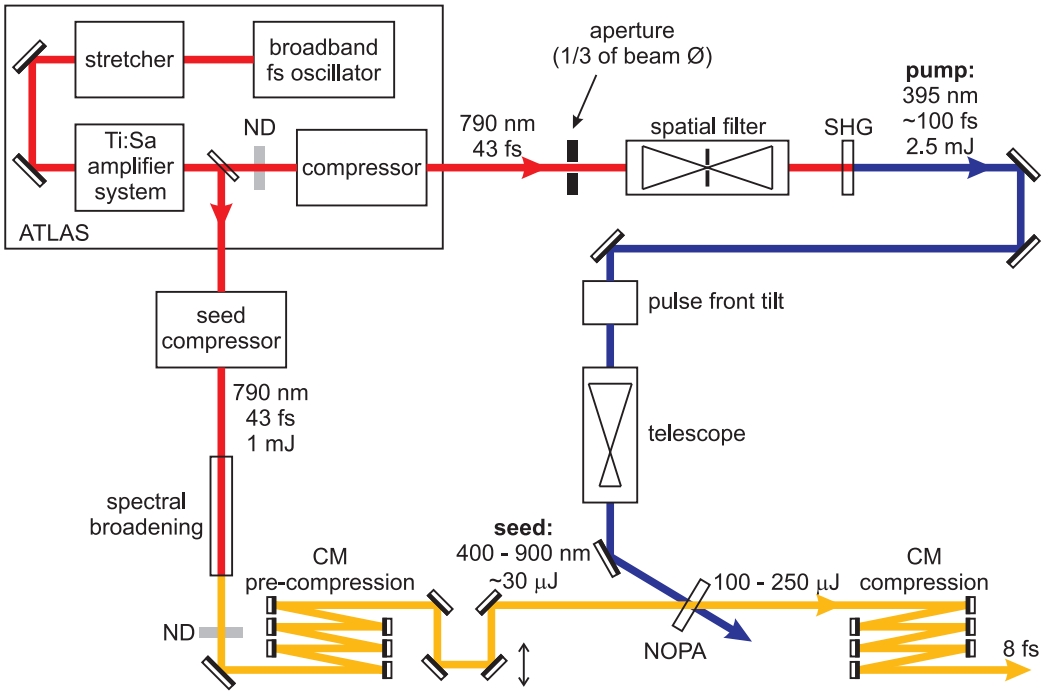

Fig. 8.1. *Schematic setup of the ATLAS-based OPCPA stage (ND: neutral density filter, CM: chirped mirror, SHG: second harmonic generation).*

pulses were then focussed by a spherical mirror of focal length 1.75 m into a gas cell filled with 1.4 bar of argon gas for spectral broadening. Using 1 mJ of input pulse energy in a 1 cm diameter beam, a stable filament was generated with an energy transmission of $\sim 80\,\%$, i.e., $800\,\mu$J. A typical broadened spectrum as measured at the filament output is displayed in figure 8.2. The input spectrum is broadened by a factor of about four, giving a transform-limited pulse duration of about 10 fs, which is in good agreement with the results of Hauri *et al.* [213] obtained for similar parameters. Following the gas cell, the seed beam was recollimated by a second spherical mirror of focal length 1.5 m.

Apart from the intense section between ~ 750 nm and ~ 850 nm, the broadened spectrum also exhibited a weak tail of exponentially decreasing intensity extending down to 400 nm as shown in the left inset of figure 8.2, which was of crucial importance for the presented amplification studies. The filament not only expanded the spectrum but additionally acted as a spatial filter resulting in an excellent output beam quality, pictured in the right inset of figure 8.2. Characterization of the seed pulses prior to amplification was done by means of spectral phase interferometry for direct electric field reconstruction (SPIDER) [214], giving a duration of about 100 fs which was comparable to the duration of the pump pulse. In order to avoid spectral

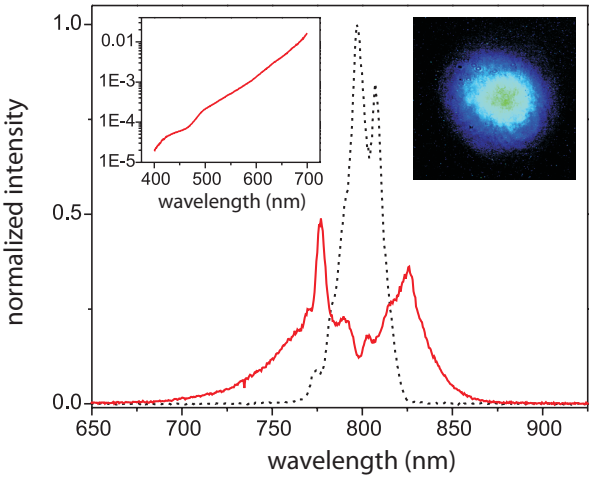

Fig. 8.2. *Seed spectrum before (black dashed line) and after (red solid line) spectral broadening in an argon filament. The left inset reveals the long short-wavelength tail of the broadened spectrum in a semi-logarithmic plot, while the inset on the right hand side demonstrates the excellent quality of the output beam spatial profile.*

narrowing in the OPA process, the seed pulses were in some cases pre-compressed by a set of chirped mirrors.

A fraction of the ATLAS laser output was frequency doubled to be used as pump beam in the OPCPA stage (see figure 8.1). Owing to the fact that in OPA the resulting gain sensitively depends upon the local pump intensity [126, 215, 216], providing a pump beam of sufficiently smooth beam profile was of fundamental importance. This issue is especially critical in case of large gain factors as typically present in the first amplifier stage. Thus, efforts were made to supply a pump beam profile as uniform as possible while simultaneously keeping the pulse energy at a sufficient level.

As known from experience based on previous experiments [217], frequency-doubling the output of ATLAS directly would be inadequate to meet the stringent requirements on pump beam uniformity. In order to address this problem and to significantly improve the pump beam profile prior to frequency doubling, a soft aperture (diameter $\sim 1/3$ of the full beam diameter) and a vacuum spatial filter were inserted into the beam path. A cone-shaped capillary pinhole [218] made of fused silica was employed as the filtering aperture (see figure 8.6a), allowing for stable operation over an extended period of time owing to the high damage threshold of the material. With this setup, pulse energies of up to 6 mJ in the fundamental were obtained at an acceptable beam profile. Subsequent frequency doubling in a 2 mm thick potassium dihydrogen phosphate (KDP) crystal at a conversion efficiency of

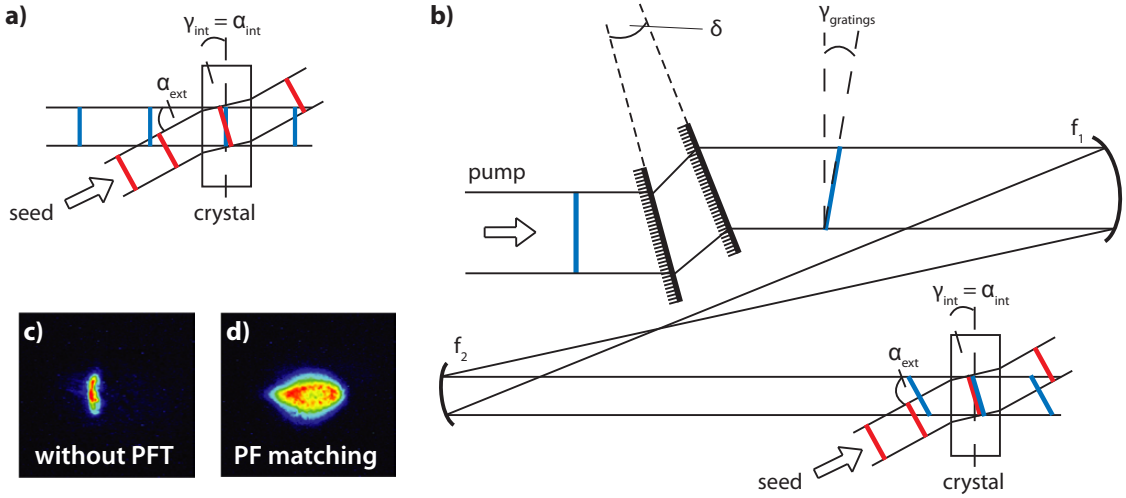

Fig. 8.3. *Short pulse pumped NOPA gives rise to poor spatial overlap of pump and seed pulse fronts in the horizontal dimension (a), resulting in severe distortion of the amplified signal beam profile (c). By angularly dispersing the beam using a pair of fused silica transmission gratings followed by an imaging telescope (b), the pump pulse front was tilted with respect to its propagation direction to match the seed pulse front within the nonlinear crystal. In this setup, the pulse front tilt angle γ was tunable by varying the grating tilt angle δ and amplification over the full extension of the seed beam could be achieved (d).*

$\sim$ 40 % resulted in 395 nm wavelength pulses at energies of 2.5 mJ and a smooth beam profile as demonstrated in figure 8.6b. The bandwidth of the second harmonic pulses was limited to $\sim$ 3 nm by the relatively thick KDP crystal, yielding an estimated pulse duration of 85 fs.

In order to obtain broadband phase matching, the OPA stage was set up in non-collinear geometry (refer to the previous section 3.1.4 for details on NOPA) with a pump-seed angle $\alpha = 3.7°$ inside the nonlinear crystal. This configuration along with the short pump and seed pulse durations and the relatively large beam diameters of a few millimeters naturally results in a poor overlap of the pump and seed pulse fronts in the horizontal direction as illustrated in figure 8.3a. Without taking any additional measures, amplification will thus only occur on a vertical stripe, leading to a serious deterioration of the signal beam. An example of such a distorted amplified beam profile is pictured in figure 8.3c.

To overcome this quandary, a setup capable of tilting the pulse front of the pump beam with respect to its propagation direction was required [118, 127]. A tilted pulse front can be generated by angularly dispersing the beam, with the tilt angle γ given by

$$\tan\gamma = -\lambda \frac{\mathrm{d}\epsilon}{\mathrm{d}\lambda} \tag{8.1}$$

Here, ϵ stands for the exit angle of the beam after the dispersive element which is dependent on the respective wavelength λ. Within the framework of the presented NOPA studies, a 45° apex angle fused silica prism was first used for beam dispersion. However, this approach was lacking γ-tunability and added a significant amount of material to the beam path, giving rise to the accumulation of nonlinear phase. Therefore the prism was replaced by a pair of fused-silica transmission gratings with 2500 lines/mm groove density, optimized for high diffraction efficiency ($> 90\,\%$) into the -1st order. The gratings were fabricated in a collaboration with the group of Prof. Tünnermann at the Institute of Applied Physics in Jena by employing electron beam lithography and reactive ion beam etching [219]. With the new setup illustrated in detail in figure 8.3b, tuning of the pulse front tilt angle γ was facilitated by varying the small angle δ between the gratings, thus controlling the amount of residual angular dispersion. In order to suppress temporal pulse distortion effects due to dispersion and spatial chirp, the grating separation was kept at a minimum.

The grating tandem was followed by a reflective Keplerian telescope serving two purposes. Firstly, the beam diameter needed to be demagnified to guarantee a low intensity value at the gratings but at the same time ensure a sufficient pump intensity level in the OPA crystal. Hence, the B-integral in the grating substrates as well as the risk of damage is reduced on one hand, while on the other hand high gain and efficient amplification is allowed for. Secondly, spectral-lateral walk-off [127] leading to an unwanted spatial chirp in the pump beam is eliminated by imaging the grating surface onto the OPA crystal. An exemplary image of the amplified beam obtained after matching the pump and seed pulse fronts within the nonlinear crystal is shown in figure 8.3d, demonstrating parametric amplification over the full seed beam profile.

8.3 Results and Discussion

In the OPCPA experiments, BBO crystals of thicknesses 0.5, 1 and 2 mm were utilized. Ultra-broadband amplification was observed from all three crystal types with the amplified signal energy varying between 100 and 250 μJ, depending on the amplification range and bandwidth which was tuned by changing the orientation of the crystal and thereby the phase matching condition.

The crystal was set up for type I phase matching in the visible and near-infrared spectral range with a non-collinear angle $\alpha = 3.7°$ to ensure the broadest possible amplification bandwidth. In order to prevent damage of the last telescope mirror

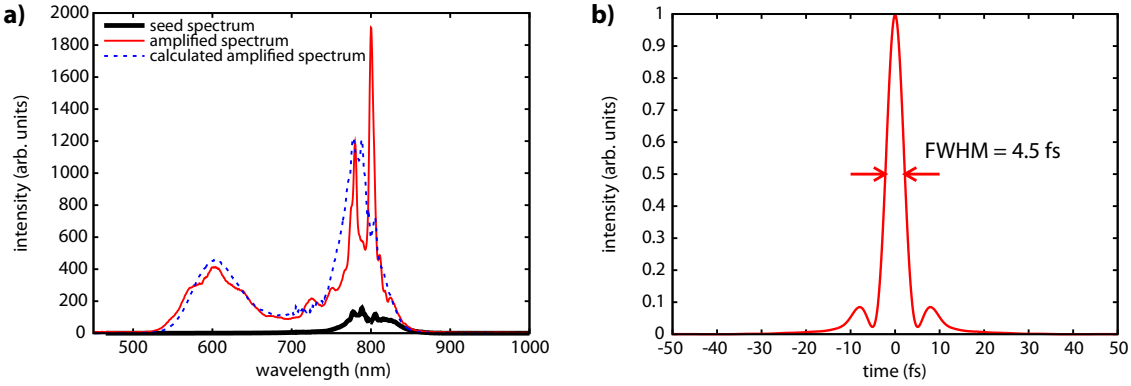

Fig. 8.4. *(a) Seed spectrum (black) and a typical signal spectrum obtained after optical parametric amplification in a 1 mm thick BBO crystal (red). The experimental results show good agreement with calculations using the measured seed spectrum as an input (blue/dashed). In (b), the Fourier transformation of the measured amplified spectrum of (a) is presented, yielding a transform-limited pulse duration as low as 4.5 fs.*

and the BBO crystal, the pump energy was attenuated to $\sim$ 1 mJ. Given the beam diameter of about 3 mm and a pulse duration of $\sim$ 85 fs, the corresponding peak pump intensity amounts to $\sim$ 150 GW/cm^2. Owing to the limited pump energy used in this proof-of-principle study, the seed energy was also reduced to $\sim$ 30 μJ prior to amplification.

A resulting typical amplified signal spectrum obtained from three-wave interaction in the 1 mm thick BBO is depicted in figure 8.4a, demonstrating a large amplification bandwidth ranging from below 550 nm to above 800 nm. In this case, a pump energy of 560 μJ and a seed energy of 20 μJ was used, which gave an amplified pulse energy of about 150 μJ with each value being subject to shot-to-shot fluctuations of $\sim$ 7 % root mean square (rms). Figure 8.4b shows the corresponding Fourier-transformation of the experimentally gained spectrum, yielding a Fourier-limited pulse duration of less than 5 fs.

A comparison of seed and amplified signal spectra in figure 8.4a clearly indicates enormous variations in gain for different spectral ranges. A gain factor of only 3-4 is observed between 750 and 850 nm where the spectral intensity of the seed is strong, whereas in the weak exponential tail below 700 nm (see figure 8.2) the gain was witnessed to be several orders of magnitude larger. This experimental finding can be attributed to different amplification regimes along the spectrum. While the signal is strongly saturated around the 800 nm peak, the short-wavelength low-intensity wing of the spectrum is unsaturated and experiences a much larger (small-signal) gain. Consequently, the resulting bandwidth is considerably enhanced and the corresponding transform-limited pulse duration is significantly reduced, from

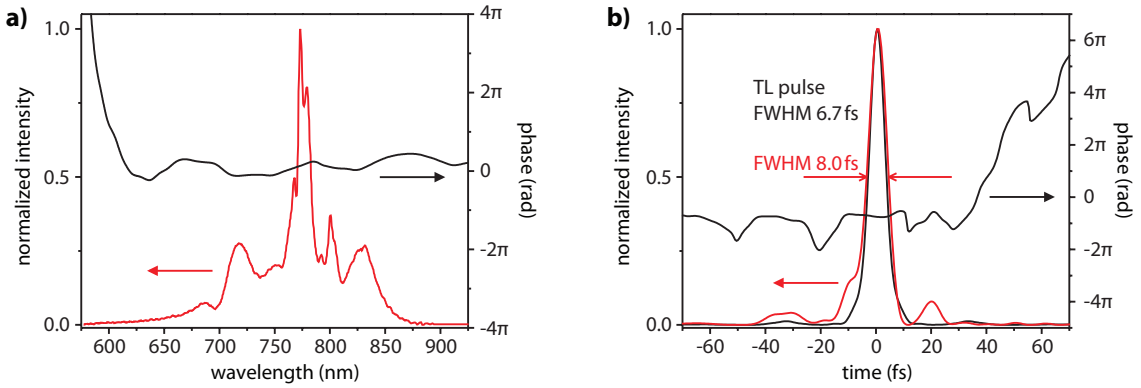

Fig. 8.5. *(a) Measured amplified signal spectrum (red) and corresponding spectral phase (black) after compression, as characterized via the SPIDER technique. In (b), the reconstructed temporal phase and intensity are presented. The experimentally obtained pulse shape (red curve) closely resembles the transform-limited (TL) distribution (black curve).*

about 10 fs for the seed to below 5 fs for the amplified signal as demonstrated in figure 8.4b.

To support the measurements, numerical calculations of the OPA gain were performed, building on a simplified 1D model [126] that uses the experimentally obtained seed spectral intensity as an input. The model assumes a monochromatic pump, a restriction which was circumvented by superimposing several calculations in order to account for the bandwidth and the angular chirp of the pump pulse. In figure 8.4a, the resulting spectrum for a set of non-collinear and phase matching angles (α and θ) close to the experimental values is shown as a dashed line. The calculation evidences good agreement with the measured amplified spectrum, reproducing both the characteristic dip in the spectrum at around 680 nm as well as the saturated (around 800 nm) and unsaturated (below 700 nm) gain regimes.

Compressibility of the amplified spectrum was tested by reflecting the beam off a set of chirped dielectric multilayer mirrors and employing a home-made SPIDER apparatus for characterization. To maximize the amplified output energy, the BBO crystal was chosen to be of thickness 2 mm in these measurements. Owing to the limited bandwidth of the chirped mirrors in the short-wavelength range, the OPA crystal was tuned to generate a narrower amplification bandwidth centered around 770 nm. In this case, the amplified spectrum as presented in figure 8.5a (red) supported a transform-limited pulse duration of 6.7 fs, with pump, seed and resulting amplified energies of 370, 60 and 150 μJ, respectively. The obtained spectral phase is nearly flat across the signal spectrum, thus indicating good compression. Fig-

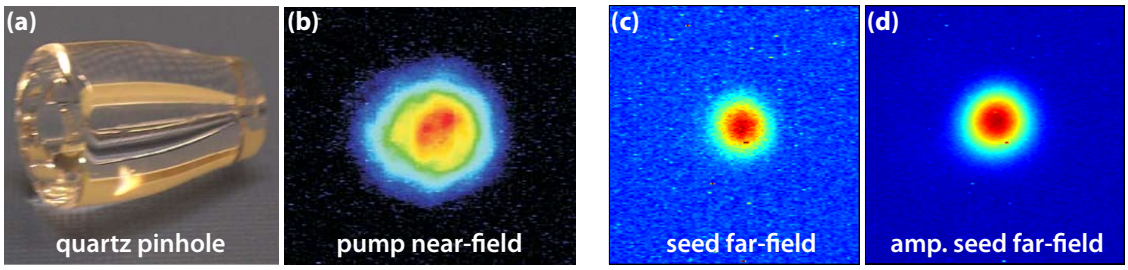

Fig. 8.6. *Cone-shaped fused silica pinhole (a) as employed to spatially filter the pump beam profile in order to meet the stringent requirements imposed by the OPA process, with the resulting near-field distribution at an energy of* $\sim 1\,mJ$ *shown in (b). The seed beam focal spot behind the filament (c) maintained its excellent quality after amplification (d). Note that images (c) and (d) are shown on the same spatial but different color scale, as the latter has been adjusted to the same maximum value.*

ure 8.5b reveals the corresponding reconstructed pulse shape, exhibiting a nearly transform-limited compressed amplified pulse duration of 8.0 fs.

It shall be noted here, that pulses generated by above described proof-of-principle OPCPA stage based on ATLAS do not yet represent a new regime in terms of pulse duration and achieved peak powers. Alternative approaches, such as the compression of a spectrally broadened hollow-fibre output [220], have been shown to deliver pulses in the few-cycle regime with pulse durations down to 5.6 fs and pulse energies up to 1.2 mJ [221]. However, scalability is a known limitation, hence disqualifying those methods for systems aiming at multi-TW to PW peak power levels.

Finally, the focusability of the signal pulse was examined for potential distortions arising from the matched pulse front SPP-OPCPA amplification process. This particular beam characteristic is of prime importance for experiments that require near diffraction-limited peak intensities in the focus, such as high-intensity laser-driven ion acceleration studies. Figure 8.6 illustrates the seed far-field beam profile before (c) and after (d) amplification. It can be clearly seen, that the excellent focusability of the beam delivered by the plasma filament is not noticeably disturbed in the OPA process employing a pulse front matched pump.

8.4 Conclusion and Outlook

In summary, a proof-of-principle ultra-broadband OPCPA stage pumped by short ($\sim$ 100 fs) pulses was demonstrated, yielding an output energy on the 100 μJ level stored in signal pulses that were compressed down to sub-10 fs. The experiments being carried out within the framework of this PhD thesis constitute the first step

towards a multi-TW, few-cycle SPP-OPCPA system. Owing to the short pump pulse duration, such a system will be capable of delivering high-intensity ultra-short pulses at a much improved nanosecond and picosecond contrast when compared to existing facilities, which is a key prerequisite for a multitude of future high-intensity laser-matter interaction studies.

Scaling up SPP-OPCPA to larger output energies calls for high power pump lasers being capable of delivering beams of high spatial uniformity in order to meet the stringent requirements of OPCPA pumping. As the system size increases, providing a suitable pump beam becomes more and more challenging. The Petawatt Field Synthesizer (PFS) project [44] that is pursued at MPQ aims to boost the output power to the petawatt level (5 J in 5 fs at a repetition rate of 10 Hz), based on the short pulse OPCPA concept and the presented first proof-of-principle results. This large-scale system is planned to be pumped by few-ps pulses, an intermediate regime where the advantages of the SPP-OPCPA concept will be combined with less critical requirements, e.g. in terms of pulse front matching, making the system design and operation more robust.

Chapter 9

Summary, Conclusions and Future Perspectives

9.1 Summary and Conclusions

In summary, advanced approaches to high intensity laser-driven ion acceleration were investigated that go beyond the previously widely studied regime of target normal sheath acceleration (TNSA). In case of TNSA, a micrometer-thick foil target is irradiated by a linearly polarized laser pulse. Highly energetic, thermal electrons are generated in a blow-off plasma at the target front which traverse the foil to set up a quasi-static electric field at the rear surface accelerating ions. It is important to note that in case of TNSA the target remains opaque to the laser light throughout the interaction. Thus, energy transfer of the laser to the target electrons is spatially decoupled from ion acceleration by the resulting longitudinal charge separation field. Only a small fraction of electrons within the laser focal volume actually participate in the ion acceleration process. Once electrons loose their energy to ions, feel the restoring force and turn around in the sheath field at the target back, they quickly spread over diameters exceeding the focal spot size by about two order of magnitude [80] which naturally reduces the longitudinal accelerating field in the center where the highest energetic ions are produced. Moreover, the sheath field is stationary, bound to the target rear surface, instead of co-propagating with the ions as they get accelerated.

Since the pioneering work that was carried out 10 years ago [1–4], it turned out that the record proton energy of 58 MeV in a continuous, exponentially decaying spectrum already achieved back in 2000 [3] could not be surpassed since then. Owing to the fact that protons preferentially gain energy in the sheath field due to their

high charge-to-mass (q/m) ratio, acceleration of heavier ions is unfavorable within the regime of TNSA, yielding medium-mass ion cut-off energies of $\sim$ 3.5 MeV/u for carbon C^{5+} [5] and 5 MeV/u for fluorine F^{7+} [18]. Furthermore, even though quasi-monochromatic ion beams have been demonstrated within the TNSA-regime by restricting the ion source to a small volume where the sheath field is homogenous [5, 20, 21], attaining a conversion efficiency from the laser to the mono-energetic ion bunch that is sufficient for potential applications does not seem feasible using these techniques.

To overcome those severe limitations and advance laser-driven ion acceleration to a higher level, acceleration from two novel target systems was explored, namely microspheres and nanometer-thin, self-supporting diamond-like carbon (DLC) foils. As opposed to typical TNSA targets, such ultra-thin foils are no longer permanently opaque to the laser but can turn into transparent instead. In multiparametric PIC simulations, a distinct optimum foil thickness at values of a few nanometers only was seen by Esirkepov *et al.* [197] upon irradiation at high laser intensities and linear polarization. Reaching these parameters experimentally is challenging, as a very high laser contrast is required to ensure an ideally unperturbed target prior to the interaction with the main pulse while simultaneously maintaining a sufficiently high intensity in the focus. In addition, preparation of the free-standing foils itself is delicate as the thickness corresponds to just a few atomic layers. Paying tribute to those hurdles, this range of laser/target parameters studied in simulations had so far been experimentally unexplored.

Employing DLC as a target compound, ultrathin foils of thickness $2.5 - 58$ nm, freestanding over diameters of 1 mm were successfully fabricated. As a part of this PhD work, acceleration from such DLC foils was investigated at a number of different laser facilities worldwide, allowing to experimentally access a broad range of varying laser parameters. In the leadoff campaign at the TRIDENT laser facility located at Los Alamos National Laboratory (LANL) in the US, DLC foils of 10, 30 and 50 nm were irradiated by pulses of energy $\sim$ 45 J stored in a FWHM duration of 700 fs, focussed to a peak intensity of 7×10^{19} W/cm^2. High contrast was achieved by placing a double plasma mirror setup acting as an ultrafast switch into the converging beam after the focussing parabolic mirror. A distinct optimum in ion acceleration was observed for an initial foil thickness of 30 nm, yielding continuous spectra of carbon C^{6+} with unprecedented cut-off values of 185 MeV. For the first time it was shown experimentally that such an optimum exists even for a clean laser pulse without accompanying ASE-pedestal/prepulses.

In order to gain further insight into the enhanced ion acceleration process and

the measured drastic drop in ion energies when the foil thickness is reduced to 10 nm, 2D PIC simulations were carried out in collaboration with L. Yin and B. Albright of the LANL plasma physics theory group. It was found that ions receive the majority of their energy in a very short period of time that is related to a transparency condition. While all targets are initially opaque to the laser and TNSA-like ion acceleration takes place in the beginning of the interaction, as the electron energy increases and the population expands more and more, eventually each foil becomes relativistically transparent, i.e., $n_e = \gamma n_c$. At that moment t_1, the laser light is enabled to fully penetrate the target and transfer energy to all electrons located within the focal volume. Moreover, the still classically overdense population of electrons is collectively pushed into the forward direction by the longitudinal component of the Lorentz force. Consequently, a strong longitudinal charge separation field enhancement is generated that is localized and co-propagates with the accelerated ions. In contrast to TNSA, energy transfer to electrons is no longer decoupled from ion acceleration but the electron energy is constantly replenished by the presence of the laser field during the acceleration process.

Nevertheless, this stage of strong ion acceleration is terminated approximately at a time t_2, when the electron density has dropped to values around the classical critical density $n_e \approx n_c$. By that time the target density is already too low to maintain a high level of absorption, three-dimensional electron expansion sets in and the localized co-moving longitudinal field enhancement breaks down. The duration of the phase of enhanced ion acceleration between times t_1 and t_2 is much shorter than the pulse duration, for given parameters only around $100 - 200$ fs. In order to maximize the resulting ion energies, the instantaneous laser intensity therefore has to be maximized during this time interval. Or, in other words, the laser intensity envelope should reach its peak at the moment when the target becomes relativistically transparent. In case of the 10 nm target, burn-through occurs much too early on the rising edge of the 700 fs FWHM pulse and most of the laser energy reaches the target past t_2, thus negligibly contributing to the acceleration of ions.

This major finding was transfered into the development of a simple analytical model of plasma expansion and heating to guide future experimental design. The model is capable of predicting the optimal target thickness for a given set of laser parameters, relying on the bottom-line conclusion reached here that $I(t_1)$ should be maximized to obtain the highest ion energies. The described experimental findings and theoretical understanding are published in [Henig *et al.*, Phys. Rev. Lett **103**, 045002 (2009)] [41]. Building onto these results and thoughts, Yan *et al.* developed a more rigorous self-similar model to additionally calculate the corresponding ion

energies, which shows good agreement with experimental data of this PhD work [203].

In the follow-up campaign again conducted at TRIDENT, higher laser intensities of $\sim 2 \times 10^{20}\,\mathrm{W/cm^2}$ could be achieved by being able to abandon the energy loss arising from plasma mirrors with the use of an upgraded, OPA-based, high contrast laser frontend. As expected by the developed analytical model, the optimum target thickness was observed to be shifted to larger values to account for the increase in intensity. At a foil thickness of 58 nm, carbon C^{6+} ions of energy exceeding 0.5 GeV were obtained, which by far outreaches previous values and constitutes the current world record gained from a laser-driven source.

For use of a rather long pulse laser like TRIDENT, the initial target thickness has to be chosen thick enough such that the moment t_1, when relativistic target transparency sets in, is sufficiently delayed until the peak of the intensity envelope is reached. To access this stage of enhanced ion acceleration more directly, a shorter pulse is beneficial owing to its steeper rising edge. Motivated by these conclusions, a series of experiments on ion acceleration from ultrathin DLC targets was carried out in collaboration with the group of Prof. Sandner at Max Born Institute (MBI) in Berlin. Behind a recollimating double plasma mirror setup, linearly polarized pulses of energy 0.7 J contained in 45 fs FWHM duration were focussed to intensities of $5 \times 10^{19}\,\mathrm{W/cm^2}$. Despite the intensity being comparable to the first LANL experiment, optimal ion acceleration was observed at a much lower foil thickness of only 5 nm. As indicated above, this result complies with the developed theoretical understanding of reduced target heating and expansion on the rising edge when a shorter Gaussian pulse is used. Maximum proton and carbon C^{6+} energies of 13 MeV and 71 MeV are obtained, which are unprecedented values for such a small scale laser system. For comparison, a typical TNSA target (1 μm thick Titanium) was shot without plasma mirrors, i.e. at two times higher laser intensity. Still, only 8 MeV protons are seen and, most notably, the conversion efficiency into protons drops by about one order of magnitude from $\sim 1.5\,\%$ to $\sim 0.1\,\%$. For carbon ions, the effect becomes even much more drastic as carbon ion acceleration from the (unheated) Ti target is negligible.

Despite the obvious benefits over conventional TNSA, the discussed enhanced ion acceleration in the regime of target transparency is still limited by the time t_2, as the linearly polarized laser pulses gives rise to highly energetic electrons causing the target to expand rapidly. However, this constraint can be overcome by changing the laser polarization to circular. Employing circular polarization at normal incidence, electron heating is strongly reduced as the longitudinal component of the Lorentz force lacks an oscillating component. Instead, electrons are piled up and compressed

at the front of the penetrating laser pulse. Within this compression layer, ions are accelerated in a phase-stable way which manifests itself in characteristic loops in the ion phase space. As long as the the electrons are being held to low energies and the compressed electron layer can be maintained, radiation pressure acceleration (RPA) of ions dominates. Thus, ions are ideally not only accelerated by a co-propagating longitudinal electric field over extended times, but the energy spread $\Delta E/E$ of the ion bunch is simultaneously compressed as the slowest, trailing ions experience the highest field within the compression layer.

This scenario of radiation pressure dominated acceleration from ultrathin foils irradiated by circularly polarized pulses has created a flurry of theoretical publications very recently, calling for experimental verification. For the first time, such measurements were successfully carried out as part of this PhD work during an experiment again at MBI Berlin with identical parameters as specified above but circular polarization. Compared to linear polarized irradiation, a significant drop in electron energies was observed as expected. Optimal ion acceleration was again obtained at a foil thickness of 5 nm, which is in accordance with the theoretically predicted RPA optimum for the normalized areal density $\sigma \simeq a_0$ [98]. Whereas the carbon C^{6+} ion spectrum decays monotonically up to its cut-off value in the case of linear polarization, now the distribution shows two components: A monotonically decaying fraction that extends up to ~ 20 MeV and a distinct peak at the highest energies, centered around 30 MeV. The spectral spike was repeatedly and exclusively seen in the carbon C^{6+} ion spectrum for circularly polarized irradiation of a 5 nm target. Compared to quasi-monoenergetic ion beam generation within the TNSA regime [5], a more than 40 times increase in conversion efficiency is demonstrated when considering an identical energy spread around the apex.

Two-dimensional PIC simulations carried out in collaboration with X. Q. Yan confirm the interpretation that those C^{6+} ions are indeed for the first time dominantly accelerated in a phase stable way by the laser radiation pressure. While an isolated carbon ion peak is still present at the end of the interaction, it later merges with the lower energetic, continuous distribution of ions dominantly accelerated by sheath fields, which at this point still gains energy, resulting in the spectrum as observed experimentally. This distortion of the carbon ion spectrum can be attributed to foil bending due to the non-flattop spatial intensity distribution in the focus. Towards the end of the interaction, highly energetic electrons are generated efficiently in the warped outer regions of the focal spot where the laser is no longer incident normally. Those electrons quickly spread around the target, causing the narrow, isolated, RPA-produced peak in the spectrum to broaden and merge with the lower

energetic component which originates from sheath acceleration in the edges of the focus. Described results and interpretations are published in [Henig *et al.*, Phys. Rev. Lett **103**, 245003 (2009)] [42].

In order to prevent a spectral deformation and maintain an isolated peak at the highest energies, the discussed late-time electron heating has to be suppressed. Since synthesizing a top-hat focal spot is far from trivial experimentally, a near-term solution might involve proper target design to account for the spatially varying intensity. This builds a bridge to earlier experiments of this PhD work on ion acceleration from microspheres. Here, the ATLAS laser located at MPQ was tightly focussed to intensities of $\sim 1 \times 10^{20}\,\mathrm{W/cm^2}$ onto the front surface of plastic spheres of diameter $\sim 15\,\mu\mathrm{m}$. A highly directed proton beam was observed that exhibited a plateau-shaped spectrum extending up to 8 MeV. Closer analysis based on three-dimensional PIC simulations revealed that this strongly pointed beam originates from the target front. Owing to the spherically curved instead of flat target surface, non-planar hole boring of the laser is compensated for. Consequently, a closer-to-flat or even convex ion acceleration front can be obtained. To predict the temporal evolution of this acceleration front an analytical model was developed where the radiation pressure acceleration model of Wilks *et al.* [39] was extended to 2D, including the effects of a spatially varying intensity distribution and a curved target surface. Those experimental and theoretical outcomes are published in [Henig *et al.*, Phys. Rev. Lett **102**, 095002 (2009)] [40].

9.2 Future Plans and Perspectives

9.2.1 Improving the Ion Beam Quality

The explored possibility to manipulate the temporal evolution of the ion acceleration front can be transfered to the scenario of RPA from ultrathin foils. By using a convex instead of planar foil in analogy to the described experiment employing microspheres, strong foil bending by a tightly focussed Gaussian spot is expected to be compensated for. With the current technology of cathodic arc deposition used for DLC foil fabrication, first prototypes of self-suporting hemispherical foils have already been produced successfully (see figure 7.5). In the very near future, such shaped DLC targets will be first applied in an experiment.

Another approach to account for the spatially varying intensity distribution would be the use of a planar target with radially varying density [106]. Although the fabrication process of such foils seems challenging and not within reach using

DLC as target compound, alternative materials and techniques are currently being tested. A promising candidate are meshes of carbon nanotubes. Prior to producing a foil of radially varying density, in a first step those carbon nanotube foams could be employed to form targets of homogenous but lower density than DLC. From RPA theory, the condition for optimum ion acceleration depends only on the normalized areal density $\sigma \approx a_0$ ([98], see equation 2.51). To verify this equation experimentally, thicker targets of lower density which exhibit a similar value of σ as a DLC foil would be highly useful.

The final energy achievable for non-relativistic ions when setting the whole focal volume in motion by RPA (i.e., in the *light sail regime*) is proportional to the square of the laser energy fluence and inverse proportional to the square of the initial ion areal density (see equation 2.52)

$$\mathcal{E}_{i,LS} \propto \frac{(I_L \tau_L)^2}{(n_{i0} d)^2} \tag{9.1}$$

Taking into account the lower limit for σ given by equation 2.51 to prevent electrons from escaping the foil ions, one obtains

$$\mathcal{E}_{i,LS} \propto I_L \tau_L^2 \tag{9.2}$$

Thus, assuming a proper choice of target parameters so that the optimum condition 2.51 is always fulfilled, for constant laser energy fluence $I_L \tau_L$ higher ion energies can be achieved in the light sail regime by stretching the pulse to longer durations. This comes at the expense of a lower number of ions in the accelerated bunch according to equation 2.51. In other words, following 1D analytical theory the energy and number of accelerated ions can be tailored for a given laser system by simply simultaneously varying the pulse duration and target thickness or density. However, the experimental studies of this thesis show that the foil plasma is significantly distorted on the extended rising edge of a long pulse with Gaussian envelope in time and multi-dimensional effects such as foil bending due to a radially varying intensity distribution in the focus deteriorate the interaction at late times. Here, an ideally rectangularly shaped pulse in both space and time would be highly desirable. The generation of a steep rising edge of the pulse could potentially be achieved by placing a second ultra-thin foil into the converging laser beam in close vicinity to the focus, acting as a reflector/absorber until becoming transparent [55, 222].

Besides driving the whole foil like a light sail, radiation pressure dominated ion acceleration can also be studied in the *hole boring regime*, where the energy of the

generated ion piston is given by (refer to equation 2.45)

$$\mathcal{E}_{i,HB} \propto \frac{I_L}{n_{i0}} \tag{9.3}$$

Hole boring RPA is easier to access experimentally since no nm-thin foil targets are required [90]. By irradiating a target of reduced density such as provided by a foam of carbon nanotubes, the predicted energy increase of radiation pressure accelerated ions in the hole-boring regime could be investigated.

In addition to future advances in target design, next generation laser systems are another important prospect for advancing the characteristics of laser-driven ion beams further. Higher laser pulse energies and intensities are expected to be beneficial to not only increase the resulting ion energy but also make the final spectrum more mono-energetic. In PIC simulations at intensities of $7 \times 10^{21}\,\mathrm{W/cm^2}$, Yan *et al.* [109] found Rayleigh-Taylor-like plasma instabilities to transversely stabilize the monochromatic ion bunch originating from the focal spot center. While the foil plasma in the wings of the laser focus is dispersed, a stable central clump is formed that maintains high density. The occurrence of such Rayleigh-Taylor-like instabilities in high intensity laser interactions with nm-thin foils was already observed within the frame of my PhD work during an experiment at the VULCAN Petawatt laser facility [153]. Analysis of that data is however partly ongoing and not included in this thesis.

To achieve large ion velocities already in the initial hole-boring phase when the laser pushes the acceleration front through the target picking up ions, high intensity irradiation of a low density target is favorable (equation 9.3). As the energy of ions accelerated by hole-boring RPA is predicted to scale linearly with laser intensity while in sheath acceleration the energy is just proportional to the square root of the intensity (refer to section 2.5.1), predominance of RPA will be more pronounced at higher laser intensities. For very high laser intensities, the ions eventually gain relativistic velocities and the non-relativistic treatment as presented in this thesis in accordance with the non-relativistic ion energies seen in the experiments is no longer adequate [104]. Recent PIC simulations at $I_L \sim 10^{22}\,\mathrm{W/cm^2}$ suggest that the acceleration of ions progresses more stable when ions reach relativistic velocities already in the initial hole-boring phase, i.e., prior to the transition to the light sail stage where the whole target propagates ballistically [107]. Finally, for ultra-high intensities ($I_L \gtrsim 10^{23}\,\mathrm{W/cm^2}$) protons become relativistic within a single laser cycle. This is referred to as the *laser-piston regime*, where RPA strongly dominates even for linear polarization [89]. Assuming that the laser pulse is perfectly reflected from

the flying foil which can be viewed as a relativistic plasma mirror co-propagating with the laser pulse, the resulting total energy transfered into ions is simply given by

$$\mathcal{E}_{i,tot} = (1 - \frac{1}{4\gamma^2})\,\mathcal{E}_L, \tag{9.4}$$

where γ denotes the Lorentz factor of the mirror and $\mathcal{E}_L$ stands for the laser energy. Thus, as γ increases towards the ultra-relativistic limit, the laser-to-ion conversion approaches unity.

9.2.2 Paving the Way Towards Applications

In terms of potential applications for laser-accelerated ion beams, three promising candidates have been discussed in the introductory chapter. Revisiting the stated necessary specifications of the ion beam for use as a fast ignitor in ICF, one aspires a quasi-monoenergetic ion bunch ($\Delta E/E$ below $\sim 10\%$) at moderate energies ($E \sim 450\,\mathrm{MeV}$ for carbon ions) but very high laser-to-ion conversion efficiencies ($\sim 10\%$) to achieve the required power density ($\sim 10\,\mathrm{kJ}/10\,\mathrm{ps}$ in a $20\,\mu\mathrm{m}$ diameter spot) to ignite the compressed DT fuel [36]. While these parameters are clearly out of reach when employing TNSA, the novel experimental results of this thesis provide a major advance, significantly reducing the gap towards ion-beam sparked ignition. Carbon ion energies beyond 0.5 GeV have been demonstrated at TRIDENT, LANL, while in the experiments at MBI Berlin a quasi-monoenergetic carbon ion spectrum was observed with a conversion efficiency of $\sim 2.5\%$ into the peak. Building onto these results, advanced target technology combined with increased laser pulse energies and intensities as described above provides excellent prospects for meeting fast ignitor requirements in the near future.

Over the course of this year, experimental efforts at MPQ will be aimed at acceleration of ion beams from nm-thin DLC foils using the upgraded ATLAS laser equipped with a re-collimating plasma mirror setup that can be operated at high repetition rates. Compared to MBI Berlin, higher peak intensities in excess of $10^{20}\,\mathrm{W/cm^2}$ will be reached in the focus, leading to increased ion energies. A biomedical beamline is currently being set up to facilitate controlled irradiation of biomedical samples by the laser-driven ion beam for radiation biology and dosimetric measurements. Those experiments will be carried out in collaboration with biologists and medical scientists as part of the cluster of excellence of the German Research Foundation "Munich-Centre for Advanced Photonics" (MAP) [223]. A

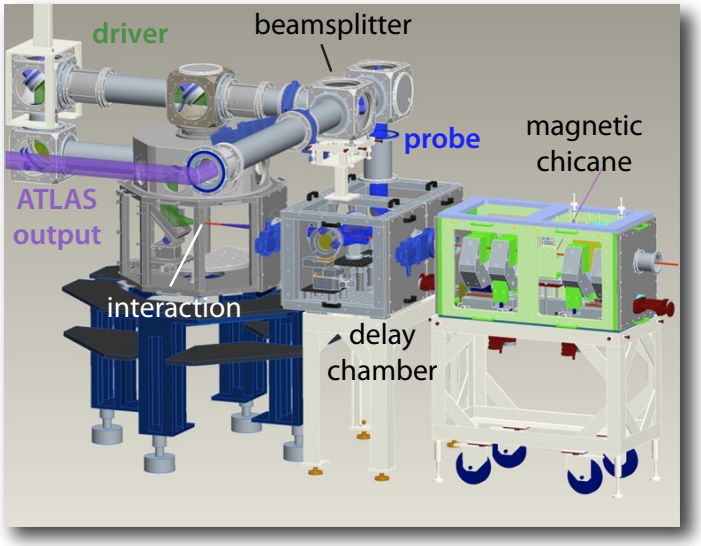

Fig. 9.1. *Drawing of the biomedical beamline currently under construction at MPQ. After pulse cleaning via a re-collimating plasma mirror setup, the ATLAS laser beam (purple color) is guided to the experimental area. Here, it is split into a strong driver beam (green color) and a probe (blue color). In the interaction chamber, the driver is focussed by an off-axis parabolic mirror onto an ultrathin foil target. The probe beam is properly timed with respect to main beam in the delay chamber and sent to the interaction region, e.g. in a counter-propagating geometry for X-ray generation via Thomson backscattering. The accelerated ion beam exits the interaction chamber to the right and is spectrally filtered in a magnetic chicane before entering the biomedical setup for cell irradiation located further downstream. (by courtesy of J. Wulz, LMU)*

drawing of the setup for ion beam generation is depicted in figure 9.1. To ensure sufficient monochromaticity of the beam, a magnetic chicane will be used as an interim energy filter [224]. Simultaneously, efforts will be aimed at producing ion beams with intrinsically well-defined energy as discussed earlier. First experiments are planned on irradiation of single cells, providing a comparative study of the relative biological effectiveness (RBE) of laser-driven ion beams versus beams from conventional ion sources such as the Munich tandem accelerator that have been investigated earlier by MAP collaborators [225]. In particular, potential variations of the RBE due to the extremely high dose rates within each particle bunch generated by one laser shot are investigated. Later, biomedical studies will be advanced to more complex samples such as hypodermic tumors in living mice.

Finally, it shall be noted that in addition to above discussed applications laser-acceleration of highly dense ion bunches provides exciting prospects for nuclear physics that could otherwise not be accessed via conventional accelerators. One prominent field of research here is the generation of neutron-rich nuclei in the range of the astrophysical r-process (the rapid neutron-capture process), far away from

the valley of stability [226–228]. Of particular interest are nuclei around the magic neutron number $N = 126$ which is a waiting point where the r-process is slowed down due to low neutron capture cross sections, representing the "bottle-neck" for the nucleosynthesis of actinides. While lower waiting point nuclei at $N = 50$ and $N = 82$ are rather well studied, nothing is known experimentally about the nuclear properties of nuclei at $N = 126$ and available models exhibit large uncertainties in this unexplored region. A possibility to produce these nuclei in an experiment is given by the fission-fusion reaction mechanism. The process relies on the fact that ion bunches of solid density can be produced with high efficiency by laser-driven radiation pressure acceleration as demonstrated for the first time in the presented thesis ([42], chapter 7), exceeding the density of ion bunches from conventional accelerators by a factor of $\sim 10^{15}$. These groundbreaking results fueled proposals for photonuclear experiments at future high-intensity laser facilities such as the Extreme Light Infrastructure (ELI) [229]. Here, it is planned to generate ^{232}Th ion bunches of energy $\sim 10\,\mathrm{MeV/u}$ and solid density via laser-driven RPA from a primary, ultrathin Th foil target, which then hit a thicker secondary Th foil located in close vicinity [230]. Fission of the heavy Th nuclei is initiated by deeply inelastic transfer of neutrons. The fission process proceeds asymmetrically, resulting in light fission fragments of nucleon number $A_L = 91$ and proton number $Z_L \approx 37.5$. Owing to the high density of the incident Th ion bunch, a high density of such light fission fragments is produced which in a second step fuse to nuclei close to the $N = 126$ waiting point in the r-process. Hence, the novel ion acceleration scheme of RPA firstly demonstrated within the framework of this PhD thesis might eventually allow to study the "terra incognita" region of neutron-rich nuclei, which is of great importance to nuclear physics and astrophysics.

Bibliography

[1] E. L. Clark, K. Krushelnick, M. Zepf, F. N. Beg, M. Tatarakis, A. Machacek, M. I. K. Santala, I. Watts, P. A. Norreys and A. E. Dangor. *Energetic Heavy-Ion and Proton Generation from Ultraintense Laser-Plasma Interactions with Solids.* Physical Review Letters, **85**(8), 1654–1657 (2000).

[2] A. Maksimchuk, S. Gu, K. Flippo, D. Umstadter and V. Y. Bychenkov. *Forward Ion Acceleration in Thin Films Driven by a High-Intensity Laser.* Physical Review Letters, **84**(18), 4108–4111 (2000).

[3] R. A. Snavely, M. H. Key, S. P. Hatchett, T. E. Cowan, M. Roth, T. W. Phillips, M. A. Stoyer, E. A. Henry, T. C. Sangster, M. S. Singh, S. C. Wilks, A. MacKinnon, A. Offenberger, D. M. Pennington, K. Yasuike, A. B. Langdon, B. F. Lasinski, J. Johnson, M. D. Perry and E. M. Campbell. *Intense High-Energy Proton Beams from Petawatt-Laser Irradiation of Solids.* Physical Review Letters, **85**(14), 2945–2948 (2000).

[4] S. P. Hatchett, C. G. Brown, T. E. Cowan, E. A. Henry, J. S. Johnson, M. H. Key, J. A. Koch, A. B. Langdon, B. F. Lasinski, R. W. Lee, A. J. Mackinnon, D. M. Pennington, M. D. Perry, T. W. Phillips, M. Roth, T. C. Sangster, M. S. Singh, R. A. Snavely, M. A. Stoyer, S. C. Wilks and K. Yasuike. *Electron, photon, and ion beams from the relativistic interaction of Petawatt laser pulses with solid targets.* Physics of Plasmas, **7**(5), 2076–2082 (2000).

[5] B. M. Hegelich, B. J. Albright, J. Cobble, K. Flippo, S. Letzring, M. Paffett, H. Ruhl, J. Schreiber, R. K. Schulze and J. C. Fernández. *Laser acceleration of quasi-monoenergetic MeV ion beams.* Nature, **439**, 441–444 (2006).

[6] T. H. Maiman. *Stimulated Optical Radiation in Ruby.* Nature, **187**, 493–494 (1960).

[7] T. Tajima and G. Mourou. *Zettawatt-exawatt lasers and their applications in*

ultrastrong-field physics. Physical Review Special Topics - Accelerators and Beams, **5**(3), 031301 (2002).

[8] G. A. Mourou, T. Tajima and S. V. Bulanov. *Optics in the relativistic regime*. Reviews of Modern Physics, **78**(2), 309 (2006).

[9] F. J. McClung and R. W. Hellwarth. *Giant Optical Pulsations from Ruby*. Journal of Applied Physics, **33**(3), 828–829 (1962).

[10] L. E. Hargrove, R. L. Fork and M. A. Pollack. *Locking of He-Ne Laser Modes Induced by Synchronous Intracavity Modulation*. Applied Physics Letters, **5**(1), 4–5 (1964).

[11] J. M. DiDomenico. *Small-Signal Analysis of Internal (Coupling-Type) Modulation of Lasers*. Journal of Applied Physics, **35**(10), 2870–2876 (1964).

[12] D. Strickland and G. Mourou. *Compression of amplified chirped optical pulses*. Optics Communications, **56**(3), 219 – 221 (1985).

[13] V. Yanovsky, V. Chvykov, G. Kalinchenko, P. Rousseau, T. Planchon, T. Matsuoka, A. Maksimchuk, J. Nees, G. Cheriaux, G. Mourou and K. Krushelnick. *Ultra-high intensity- 300-TW laser at 0.1 Hz repetition rate*. Optics Express, **16**(3), 2109–2114 (2008).

[14] T. Tajima and J. M. Dawson. *Laser Electron Accelerator*. Physical Review Letters, **43**(4), 267–270 (1979).

[15] W. P. Leemans, B. Nagler, A. J. Gonsalves, C. Tóth, K. Nakamura, C. G. R. Geddes, E. Esarey, C. B. Schroeder and S. M. Hooker. *GeV electron beams from a centimetre-scale accelerator*. Nature Physics, **2**, 696–699 (2006).

[16] A. P. Fews, P. A. Norreys, F. N. Beg, A. R. Bell, A. E. Dangor, C. N. Danson, P. Lee and S. J. Rose. *Plasma Ion Emission from High Intensity Picosecond Laser Pulse Interactions with Solid Targets*. Physical Review Letters, **73**(13), 1801–1804 (1994).

[17] T. E. Cowan, J. Fuchs, H. Ruhl, A. Kemp, P. Audebert, M. Roth, R. Stephens, I. Barton, A. Blazevic, E. Brambrink, J. Cobble, J. Fernández, J.-C. Gauthier, M. Geissel, M. Hegelich, J. Kaae, S. Karsch, G. P. Le Sage, S. Letzring, M. Manclossi, S. Meyroneinc, A. Newkirk, H. Pépin and N. Renard-LeGalloudec. *Ultralow Emittance, Multi-MeV Proton Beams from a Laser*

Virtual-Cathode Plasma Accelerator. Physical Review Letters, **92**(20), 204801 (2004).

[18] M. Hegelich, S. Karsch, G. Pretzler, D. Habs, K. Witte, W. Guenther, M. Allen, A. Blazevic, J. Fuchs, J. C. Gauthier, M. Geissel, P. Audebert, T. Cowan and M. Roth. *MeV Ion Jets from Short-Pulse-Laser Interaction with Thin Foils*. Physical Review Letters, **89**(8), 085002 (2002).

[19] P. McKenna, F. Lindau, O. Lundh, D. C. Carroll, R. J. Clarke, K. W. D. Ledingham, T. McCanny, D. Neely, A. P. L. Robinson, L. Robson, P. T. Simpson, C.-G. Wahlström and M. Zepf. *Low- and medium-mass ion acceleration driven by petawatt laser plasma interactions*. Plasma Physics and Controlled Fusion, **49**(12B), B223–B231 (2007).

[20] H. Schwoerer, S. Pfotenhauer, O. Jackel, K. U. Amthor, B. Liesfeld, W. Ziegler, R. Sauerbrey, K. W. D. Ledingham and T. Esirkepov. *Laser-plasma acceleration of quasi-monoenergetic protons from microstructured targets*. Nature, **439**(7075), 445–448 (2006).

[21] S. Ter-Avetisyan, M. Schnürer, P. V. Nickles, M. Kalashnikov, E. Risse, T. Sokollik, W. Sandner, A. Andreev and V. Tikhonchuk. *Quasimonoenergetic Deuteron Bursts Produced by Ultraintense Laser Pulses*. Physical Review Letters, **96**(14), 145006 (2006).

[22] M. Borghesi, D. Campbell, A. Schiavi, O. Willi, A. MacKinnon, D. Hicks, P. Patel, L. Gizzi, M. Galimberti and R. Clarke. *Laser-produced protons and their application as a particle probe*. Laser and Particle Beams, **20**(02), 269–275 (2002).

[23] M. Borghesi, A. Schiavi, D. H. Campbell, M. G. Haines, O. Willi, A. J. Mackinnon, P. Patel, M. Galimberti and L. A. Gizzi. *Proton imaging detection of transient electromagnetic fields in laser-plasma interactions (invited)*. Review of Scientific Instruments, **74**(3), 1688–1693 (2003).

[24] M. Borghesi, A. J. Mackinnon, D. H. Campbell, D. G. Hicks, S. Kar, P. K. Patel, D. Price, L. Romagnani, A. Schiavi and O. Willi. *Multi-MeV Proton Source Investigations in Ultraintense Laser-Foil Interactions*. Physical Review Letters, **92**(5), 055003 (2004).

[25] L. Romagnani, J. Fuchs, M. Borghesi, P. Antici, P. Audebert, F. Ceccherini, T. Cowan, T. Grismayer, S. Kar, A. Macchi, P. Mora, G. Pretzler, A. Schiavi, T. Toncian and O. Willi. *Dynamics of Electric Fields Driving the Laser Acceleration of Multi-MeV Protons.* Physical Review Letters, **95**(19), 195001 (2005).

[26] M. Borghesi, S. V. Bulanov, T. Z. Esirkepov, S. Fritzler, S. Kar, T. V. Liseikina, V. Malka, F. Pegoraro, L. Romagnani, J. P. Rousseau, A. Schiavi, O. Willi and A. V. Zayats. *Plasma Ion Evolution in the Wake of a High-Intensity Ultrashort Laser Pulse.* Physical Review Letters, **94**(19), 195003 (2005).

[27] D. Ondreka and U. Weinrich. *The Heidelberg Ion Therapy (HIT) accelerator coming into operation.* Proceedings of EPAC08, Genoa, Italy (2008).

[28] URL http://www.klinikum.uni-heidelberg.de/Startseite-HIT.113005.0.html.

[29] T. Tajima, D. Habs and X. Q. Yan. *Laser Acceleration of Ions for Radiation Therapy.* In A. W. Chao and W. Chou (editors), *Reviews of Accelerator Science and Technology (RAST)*, volume 2: "Medical Applications of Accelerators", pp. 201–228. World Scientific Publishing Co Pte Ltd (2009).

[30] URL http://www.iter.org/.

[31] URL https://lasers.llnl.gov/.

[32] M. Tabak, J. Hammer, M. E. Glinsky, W. L. Kruer, S. C. Wilks, J. Woodworth, E. M. Campbell, M. D. Perry and R. J. Mason. *Ignition and high gain with ultrapowerful lasers.* Physics of Plasmas, **1**(5), 1626–1634 (1994).

[33] R. Kodama, P. A. Norreys, K. Mima, A. E. Dangor, R. G. Evans, H. Fujita, Y. Kitagawa, K. Krushelnick, T. Miyakoshi, N. Miyanaga, T. Norimatsu, S. J. Rose, T. Shozaki, K. Shigemori, A. Sunahara, M. Tampo, K. A. Tanaka, Y. Toyama, T. Yamanaka and M. Zepf. *Fast heating of ultrahigh-density plasma as a step towards laser fusion ignition.* Nature, **412**, 798–802 (2001).

[34] M. Roth, T. E. Cowan, M. H. Key, S. P. Hatchett, C. Brown, W. Fountain, J. Johnson, D. M. Pennington, R. A. Snavely, S. C. Wilks, K. Yasuike, H. Ruhl, F. Pegoraro, S. V. Bulanov, E. M. Campbell, M. D. Perry and H. Powell. *Fast*

Ignition by Intense Laser-Accelerated Proton Beams. Physical Review Letters, **86**(3), 436–439 (2001).

[35] M. H. Key. *Status of and prospects for the fast ignition inertial fusion concept.* Physics of Plasmas, **14**(5), 055502 (2007).

[36] J. C. Fernandez, J. Honrubia, B. J. Albright, K. A. Flippo, D. C. Gautier, B. M. Hegelich, M. J. Schmitt, M. Temporal and L. Yin. *Progress and prospects of ion-driven fast ignition.* Nuclear Fusion, **49**(6), 065004 (8pp) (2009).

[37] J. J. Honrubia, J. C. Fernández, M. Temporal, B. M. Hegelich and J. Meyer-ter-Vehn. *Fast ignition of inertial fusion targets by laser-driven carbon beams.* Physics of Plasmas, **16**(10), 102701 (2009).

[38] L. O. Silva, M. Marti, J. R. Davies, R. A. Fonseca, C. Ren, F. S. Tsung and W. B. Mori. *Proton Shock Acceleration in Laser-Plasma Interactions.* Physical Review Letters, **92**(1), 015002 (2004).

[39] S. C. Wilks, W. L. Kruer, M. Tabak and A. B. Langdon. *Absorption of ultra-intense laser pulses.* Physical Review Letters, **69**(9), 1383–1386 (1992).

[40] A. Henig, D. Kiefer, M. Geissler, S. G. Rykovanov, R. Ramis, R. Hörlein, J. Osterhoff, Zs. Major, L. Veisz, S. Karsch, F. Krausz, D. Habs and J. Schreiber. *Laser-Driven Shock Acceleration of Ion Beams from Spherical Mass-Limited Targets.* Physical Review Letters, **102**(9), 095002 (2009).

[41] A. Henig, D. Kiefer, K. Markey, D. C. Gautier, K. A. Flippo, S. Letzring, R. P. Johnson, T. Shimada, L. Yin, B. J. Albright, K. J. Bowers, J. C. Fernández, S. G. Rykovanov, H.-C. Wu, M. Zepf, D. Jung, V. K. Liechtenstein, J. Schreiber, D. Habs and B. M. Hegelich. *Enhanced Laser-Driven Ion Acceleration in the Relativistic Transparency Regime.* Physical Review Letters, **103**(4), 045002 (2009).

[42] A. Henig, S. Steinke, M. Schnürer, T. Sokollik, R. Hörlein, D. Kiefer, D. Jung, J. Schreiber, B. M. Hegelich, X. Q. Yan, J. Meyer-ter-Vehn, T. Tajima, P. V. Nickles, W. Sandner and D. Habs. *Radiation-Pressure Acceleration of Ion Beams Driven by Circularly Polarized Laser Pulses.* Physical Review Letters, **103**(24), 245003 (2009).

[43] J. A. Fülöp, Zs. Major, A. Henig, S. Kruber, R. Weingartner, T. Clausnitzer, E.-B. Kley, A. Tunnermann, V. Pervak, A. Apolonski, J. Osterhoff, R. Horlein, F. Krausz and S. Karsch. *Short-pulse optical parametric chirped-pulse*

amplification for the generation of high-power few-cycle pulses. New Journal of Physics, **9**(12), 438 (2007).

[44] Zs. Major, S. Trushin, I. Ahmad, M. Siebold, C. Wandt, S. Klingebiel, T.-J. Wang, J. A. Fülöp, A. Henig, S. Kruber, R. Weingartner, A. Popp, J. Osterhoff, R. Hörlein, J. Hein, V. Pervak, A. Apolonski, F. Krausz and S. Karsch. *Basic Concepts and Current Status of the Petawatt Field Synthesizer A New Approach to Ultrahigh Field Generation.* Review of Laser Engineering, **37**, 431 (2009).

[45] W. L. Kruer. *The Physics of Laser Plasma Interactions.* Westview Press (2003).

[46] P. Gibbon. *Short Pulse Laser Interactions with Matter.* Imperial College Press (2005).

[47] L. V. Keldysh. *Ionization in the field of a strong electromagnetic wave.* Soviet Physics - JETP, **20**, 1307 (1965).

[48] M. V. Ammosov, N. B. Delone and V. P. Kraĭnov. *Tunnel ionization of complex atoms and of atomic ions in an alternating electromagnetic field.* Soviet Physics - JETP, **64**(6), 1191–1194 (1986).

[49] M. Uiberacker, T. Uphues, M. Schultze, A. J. Verhoef, V. Yakovlev, M. F. Kling, J. Rauschenberger, N. M. Kabachnik, H. Schröder, M. Lezius, K. L. Kompa, H. Muller, M. J. J. Vrakking, S. Hendel, U. Kleineberg, U. Heinzmann, M. Drescher and F. Krausz. *Attosecond real-time observation of electron tunnelling in atoms.* Nature, **446**, 627–632 (2007).

[50] I. H. Hutchinson. *Principles of Plasma Diagnostics.* Cambridge University Press, Cambridge (1987).

[51] Y. T. Lee. *A model for ionization balance and L-shell spectroscopy of non-LTE plasmas.* Journal of Quantitative Spectroscopy and Radiative Transfer, **38**(2), 131 – 145 (1987).

[52] J. Meyer-ter-Vehn, A. Pukhov and Z.-M. Sheng. *Relativistic Laser Plasma Interaction.* In D. Batani (editor), *Atoms, Solids and Plasmas in Super-Intense Laser Fields.* Kluwer Academic/Plenum Publishers (2001).

[53] C. I. Moore, J. P. Knauer and D. D. Meyerhofer. *Observation of the Transition from Thomson to Compton Scattering in Multiphoton Interactions with Low-Energy Electrons.* Physical Review Letters, **74**(13), 2439–2442 (1995).

[54] M. Borghesi, A. J. MacKinnon, L. Barringer, R. Gaillard, L. A. Gizzi, C. Meyer, O. Willi, A. Pukhov and J. Meyer-ter-Vehn. *Relativistic Channeling of a Picosecond Laser Pulse in a Near-Critical Preformed Plasma.* Physical Review Letters, **78**(5), 879–882 (1997).

[55] V. A. Vshivkov, N. M. Naumova, F. Pegoraro and S. V. Bulanov. *Nonlinear electrodynamics of the interaction of ultra-intense laser pulses with a thin foil.* Physics of Plasmas, **5**(7), 2727–2741 (1998).

[56] F. Brunel. *Not-so-resonant, resonant absorption.* Physical Review Letters, **59**(1), 52–55 (1987).

[57] F. Brunel. *Anomalous absorption of high intensity subpicosecond laser pulses.* Physics of Fluids, **31**(9), 2714–2719 (1988).

[58] W. L. Kruer and K. Estabrook. *J x B heating by very intense laser light.* Physics of Fluids, **28**(1), 430–432 (1985).

[59] D. D. Meyerhofer, H. Chen, J. A. Delettrez, B. Soom, S. Uchida and B. Yaakobi. *Resonance absorption in high-intensity contrast, picosecond laser–plasma interactions.* Physics of Fluids B: Plasma Physics, **5**(7), 2584–2588 (1993).

[60] T. Ditmire, T. Donnelly, A. M. Rubenchik, R. W. Falcone and M. D. Perry. *Interaction of intense laser pulses with atomic clusters.* Physical Review A, **53**(5), 3379–3402 (1996).

[61] D. R. Symes, M. Hohenberger, A. Henig and T. Ditmire. *Anisotropic Explosions of Hydrogen Clusters under Intense Femtosecond Laser Irradiation.* Physical Review Letters, **98**(12), 123401 (2007).

[62] G. S. Sarkisov, V. Y. Bychenkov, V. N. Novikov, V. T. Tikhonchuk, A. Maksimchuk, S.-Y. Chen, R. Wagner, G. Mourou and D. Umstadter. *Self-focusing, channel formation, and high-energy ion generation in interaction of an intense short laser pulse with a He jet.* Physical Review E, **59**(6), 7042–7054 (1999).

[63] T. Esirkepov, Y. Sentoku, K. Mima, K. Nishihara, F. Califano, F. Pegoraro, N. Naumova, S. Bulanov, Y. Ueshima, T. Liseikina, V. Vshivkov and Y. Kato. *Ion acceleration by superintense laser pulses in plasmas.* JETP Letters, **70**(2), 82–89 (1999).

[64] S. Bulanov, T. Esirkepov, F. Califano, Y. Kato, T. Liseikina, K. Mima, N. Naumova, K. Nishihara, F. Pegoraro, H. Ruhl, Y. Sentoku and Y. Ueshima. *Generation of collimated beams of relativistic ions in laser-plasma interactions.* JETP Letters, **71**(10), 407–411 (2000).

[65] Y. Sentoku, T. V. Liseikina, T. Z. Esirkepov, F. Califano, N. M. Naumova, Y. Ueshima, V. A. Vshivkov, Y. Kato, K. Mima, K. Nishihara, F. Pegoraro and S. V. Bulanov. *High density collimated beams of relativistic ions produced by petawatt laser pulses in plasmas.* Physical Review E, **62**(5), 7271–7281 (2000).

[66] C. Bellei, S. Nagel, S. Kar, A. Henig, S. Kneip, C. Palmer, A. Saevert, L. Willingale, D. Carroll, B. Dromey, J. Green, K. Markey, P. Simpson, R. J. Clarke, D. Neely, M. Kaluza, S. P. D. Mangles, P. McKenna, P. A. Norreys, J. Schreiber, M. Zepf, K. Krushelnick and Z. Najmudin. *Characterisation of Fast Electron Recirculation and Filamentation from Rear Side Optical Emission in High Intensity Laser-Solid Interactions.* submitted (2010).

[67] S. C. Wilks, A. B. Langdon, T. E. Cowan, M. Roth, M. Singh, S. Hatchett, M. H. Key, D. Pennington, A. MacKinnon and R. A. Snavely. *Energetic proton generation in ultra-intense laser–solid interactions.* Physics of Plasmas, **8**(2), 542–549 (2001).

[68] M. Widner, I. Alexeff and W. D. Jones. *Plasma Expansion into a Vacuum.* Physics of Fluids, **14**(4), 795–796 (1971).

[69] J. E. Crow, P. L. Auer and J. E. Allen. *The expansion of a plasma into a vacuum.* Journal of Plasma Physics, **14**, 65–76 (1975).

[70] S. J. Gitomer, R. D. Jones, F. Begay, A. W. Ehler, J. F. Kephart and R. Kristal. *Fast ions and hot electrons in the laser–plasma interaction.* Physics of Fluids, **29**(8), 2679–2688 (1986).

[71] J. Denavit. *Collisionless plasma expansion into a vacuum.* Physics of Fluids, **22**(7), 1384–1392 (1979).

[72] Y. Kishimoto, K. Mima, T. Watanabe and K. Nishikawa. *Analysis of fast-ion velocity distributions in laser plasmas with a truncated Maxwellian velocity distribution of hot electrons.* Physics of Fluids, **26**(8), 2308–2315 (1983).

[73] P. Mora. *Plasma Expansion into a Vacuum.* Physical Review Letters, **90**(18), 185002 (2003).

[74] P. Mora. *Thin-foil expansion into a vacuum.* Physical Review E, **72**(5), 056401 (2005).

[75] J. Schreiber, F. Bell, F. Grüner, U. Schramm, M. Geissler, M. Schnürer, S. Ter-Avetisyan, B. M. Hegelich, J. Cobble, E. Brambrink, J. Fuchs, P. Audebert and D. Habs. *Analytical Model for Ion Acceleration by High-Intensity Laser Pulses.* Physical Review Letters, **97**(4), 045005 (2006).

[76] A. J. Mackinnon, Y. Sentoku, P. K. Patel, D. W. Price, S. Hatchett, M. H. Key, C. Andersen, R. Snavely and R. R. Freeman. *Enhancement of Proton Acceleration by Hot-Electron Recirculation in Thin Foils Irradiated by Ultraintense Laser Pulses.* Physical Review Letters, **88**(21), 215006 (2002).

[77] M. Roth, M. Allen, P. Audebert, A. Blazevic, E. Brambrink, T. E. Cowan, J. Fuchs, J.-C. Gauthier, M. Geissel, M. Hegelich, S. Karsch, J. Meyer-ter-Vehn, H. Ruhl, T. Schlegel and R. B. Stephens. *The generation of high-quality, intense ion beams by ultra-intense lasers.* Plasma Physics and Controlled Fusion, **44**(12B), B99–B108 (2002).

[78] S. Fritzler, V. Malka, G. Grillon, J. P. Rousseau, F. Burgy, E. Lefebvre, E. d'Humières, P. McKenna and K. W. D. Ledingham. *Proton beams generated with high-intensity lasers: Applications to medical isotope production.* Applied Physics Letters, **83**(15), 3039–3041 (2003).

[79] M. Kaluza, J. Schreiber, M. I. K. Santala, G. D. Tsakiris, K. Eidmann, J. Meyer-ter-Vehn and K. J. Witte. *Influence of the Laser Prepulse on Proton Acceleration in Thin-Foil Experiments.* Physical Review Letters, **93**(4), 045003 (2004).

[80] J. Schreiber, M. Kaluza, F. Grüner, U. Schramm, B. M. Hegelich, J. Cobble, M. Geissler, E. Brambrink, J. Fuchs, P. Audebert, D. Habs and K. Witte. *Source-size measurements and charge distributions of ions accelerated from thin foils irradiated by high-intensity laser pulses.* Applied Physics B: Lasers and Optics, **79**(8), 1041–1045 (2004).

[81] J. Fuchs, P. Antici, E. D'Humières, E. Lefebvre, M. Borghesi, E. Brambrink, C. A. Cecchetti, M. Kaluza, V. Malka, M. Manclossi, S. Meyroneinc, P. Mora, J. Schreiber, T. Toncian, H. Pépin and P. Audebert. *Laser-driven proton scaling laws and new paths towards energy increase.* Nature Physics, **2**, 48–54 (2006).

[82] L. Robson, P. T. Simpson, R. J. Clarke, K. W. D. Ledingham, F. Lindau, O. Lundh, T. McCanny, P. Mora, D. Neely, C. G. Wahlstrom, M. Zepf and P. McKenna. *Scaling of proton acceleration driven by petawatt-laser-plasma interactions.* Nature Physics, **3**(1), 58–62 (2007).

[83] S. M. Pfotenhauer, O. Jäckel, A. Sachtleben, J. Polz, W. Ziegler, H.-P. Schlenvoigt, K.-U. Amthor, M. C. Kaluza, K. W. D. Ledingham, R. Sauerbrey, P. Gibbon, A. P. L. Robinson and H. Schwoerer. *Spectral shaping of laser generated proton beams.* New Journal of Physics, **10**(3), 033034 (14pp) (2008).

[84] P. McKenna, K. W. D. Ledingham, J. M. Yang, L. Robson, T. McCanny, S. Shimizu, R. J. Clarke, D. Neely, K. Spohr, R. Chapman, R. P. Singhal, K. Krushelnick, M. S. Wei and P. A. Norreys. *Characterization of proton and heavier ion acceleration in ultrahigh-intensity laser interactions with heated target foils.* Physical Review E, **70**(3), 036405 (2004).

[85] D. W. Forslund and C. R. Shonk. *Formation and Structure of Electrostatic Collisionless Shocks.* Physical Review Letters, **25**(25), 1699–1702 (1970).

[86] D. W. Forslund and J. P. Freidberg. *Theory of Laminar Collisionless Shocks.* Physical Review Letters, **27**(18), 1189–1192 (1971).

[87] J. Denavit. *Absorption of high-intensity subpicosecond lasers on solid density targets.* Physical Review Letters, **69**(21), 3052–3055 (1992).

[88] G. Marx. *Interstellar Vehicle Propelled By Terrestrial Laser Beam.* Nature, **211**, 22–23 (1966).

[89] T. Esirkepov, M. Borghesi, S. V. Bulanov, G. Mourou and T. Tajima. *Highly Efficient Relativistic-Ion Generation in the Laser-Piston Regime.* Physical Review Letters, **92**(17), 175003 (2004).

[90] A. Macchi, F. Cattani, T. V. Liseykina and F. Cornolti. *Laser Acceleration of Ion Bunches at the Front Surface of Overdense Plasmas.* Physical Review Letters, **94**(16), 165003 (2005).

[91] T. V. Liseikina, D. Prellino, F. Cornolti and A. Macchi. *Ponderomotive Acceleration of Ions: Circular Versus Linear Polarization.* IEEE Transactions on Plasma Science, **36**, 1866–1871 (2008).

[92] T. V. Liseikina and A. Macchi. *Features of ion acceleration by circularly polarized laser pulses.* Applied Physics Letters, **91**(17), 171502 (2007).

[93] T. V. Liseykina, M. Borghesi, A. Macchi and S. Tuveri. *Radiation pressure acceleration by ultraintense laser pulses.* Plasma Physics and Controlled Fusion, **50**(12), 124033 (9pp) (2008).

[94] O. Klimo, J. Psikal, J. Limpouch and V. T. Tikhonchuk. *Monoenergetic ion beams from ultrathin foils irradiated by ultrahigh-contrast circularly polarized laser pulses.* Physical Review Special Topics - Accelerators and Beams, **11**(3), 031301 (2008).

[95] V. V. Kulagin, V. A. Cherepenin, M. S. Hur and H. Suk. *Theoretical Investigation of Controlled Generation of a Dense Attosecond Relativistic Electron Bunch from the Interaction of an Ultrashort Laser Pulse with a Nanofilm.* Physical Review Letters, **99**(12), 124801 (2007).

[96] D. Habs, M. Hegelich, J. Schreiber, M. Gross, A. Henig, D. Kiefer and D. Jung. *Dense laser-driven electron sheets as relativistic mirrors for coherent production of brilliant X-ray and γ-ray beams.* Applied Physics B: Lasers and Optics, **93**, 349–354 (2008).

[97] D. Kiefer, A. Henig, D. Jung, D. C. Gautier, K. A. Flippo, S. A. Gaillard, S. Letzring, R. P. Johnson, R. C. Shah, T. Shimada, J. C. Fernández, V. K. Liechtenstein, J. Schreiber, B. M. Hegelich and D. Habs. *First observation of quasi-monoenergetic electron bunches driven out of ultra-thin diamond-like carbon (DLC) foils.* European Physical Journal D, **55**(2), 427–432 (2009).

[98] X. Q. Yan, C. Lin, Z. M. Sheng, Z. Y. Guo, B. C. Liu, Y. R. Lu, J. X. Fan and J. E. Chen. *Generating High-Current Monoenergetic Proton Beams by a CircularlyPolarized Laser Pulse in the Phase-StableAcceleration Regime.* Physical Review Letters, **100**(13), 135003–4 (2008).

[99] X. Zhang, B. Shen, X. Li, Z. Jin and F. Wang. *Multistaged acceleration of ions by circularly polarized laser pulse: Monoenergetic ion beam generation.* Physics of Plasmas, **14**(7), 073101 (2007).

[100] X. Zhang, B. Shen, X. Li, Z. Jin, F. Wang and M. Wen. *Efficient GeV ion generation by ultraintense circularly polarized laser pulse.* Physics of Plasmas, **14**(12), 123108 (2007).

[101] A. P. L. Robinson, M. Zepf, S. Kar, R. G. Evans and C. Bellei. *Radiation pressure acceleration of thin foils with circularly polarized laser pulses.* New Journal of Physics, **10**(1), 013021 (13pp) (2008).

[102] S. G. Rykovanov, J. Schreiber, J. Meyer-ter-Vehn, C. Bellei, A. Henig, H. C. Wu and M. Geissler. *Ion acceleration with ultra-thin foils using elliptically polarized laser pulses.* New Journal of Physics, **10**(11), 113005 (10pp) (2008).

[103] A. P. L. Robinson, D.-H. Kwon and K. Lancaster. *Hole-boring radiation pressure acceleration with two ion species.* Plasma Physics and Controlled Fusion, **51**(9), 095006 (11pp) (2009).

[104] A. P. L. Robinson, P. Gibbon, M. Zepf, S. Kar, R. G. Evans and C. Bellei. *Relativistically correct hole-boring and ion acceleration by circularly polarized laser pulses.* Plasma Physics and Controlled Fusion, **51**(2), 024004 (14pp) (2009).

[105] M. Chen, A. Pukhov, Z. M. Sheng and X. Q. Yan. *Laser mode effects on the ion acceleration during circularly polarized laser pulse interaction with foil targets.* Physics of Plasmas, **15**(11), 113103 (2008).

[106] M. Chen, A. Pukhov, T. P. Yu and Z. M. Sheng. *Enhanced Collimated GeV Monoenergetic Ion Acceleration from a Shaped Foil Target Irradiated by a Circularly Polarized Laser Pulse.* Physical Review Letters, **103**(2), 024801 (2009).

[107] B. Qiao, M. Zepf, M. Borghesi and M. Geissler. *Stable GeV Ion-Beam Acceleration from Thin Foils by Circularly Polarized Laser Pulses.* Physical Review Letters, **102**(14), 145002 (2009).

[108] A. Macchi, S. Veghini and F. Pegoraro. *"Light Sail" Acceleration Reexamined.* Physical Review Letters, **103**(8), 085003 (2009).

[109] X. Q. Yan, H. C. Wu, Z. M. Sheng, J. E. Chen and J. Meyer-ter-Vehn. *Self-Organizing GeV, Nanocoulomb, Collimated Proton Beam from Laser Foil Interaction at* $7 \times 10^{21}\ W/cm^2$. Physical Review Letters, **103**(13), 135001 (2009).

[110] A. E. Siegmann. *Lasers*. University Science Books (1986).

[111] F. Krausz, L. Turi, C. Kuti and A. J. Schmidt. *Active mode locking of lasers by piezoelectrically induced diffraction modulation*. Applied Physics Letters, **56**(15), 1415–1417 (1990).

[112] L. Turi, C. Kuti and F. Krausz. *Piezoelectrically induced diffraction modulation of light*. IEEE Journal of Quantum Electronics, **26**, 1234–1240 (1990).

[113] W. T. Silfvast. *Laser Fundamentals*. Cambridge University Press (1996).

[114] G. M. Gale, M. Cavallari, T. J. Driscoll and F. Hache. *Sub-20-fs tunable pulses in the visible from an 82-MHz optical parametric oscillator*. Optics Letters, **20**(14), 1562–1564 (1995).

[115] T. Wilhelm, J. Piel and E. Riedle. *Sub-20-fs pulses tunable across the visible from a blue-pumped single-pass noncollinear parametric converter*. Optics Letters, **22**(19), 1494–1496 (1997).

[116] I. N. Ross, P. Matousek, M. Towrie, A. J. Langley and J. L. Collier. *The prospects for ultrashort pulse duration and ultrahigh intensity using optical parametric chirped pulse amplifiers*. Optics Communications, **144**(1-3), 125 – 133 (1997).

[117] G. Cerullo, M. Nisoli, S. Stagira and S. D. Silvestri. *Sub-8-fs pulses from an ultrabroadband optical parametric amplifier in the visible*. Optics Letters, **23**(16), 1283–1285 (1998).

[118] A. Shirakawa, I. Sakane, M. Takasaka and T. Kobayashi. *Sub-5-fs visible pulse generation by pulse-front-matched noncollinear optical parametric amplification*. Applied Physics Letters, **74**(16), 2268–2270 (1999).

[119] A. Baltuška and T. Kobayashi. *Parametric Amplification and Phase Control of Few-Cycle Light Pulses*. In F. X. Kärtner (editor), *Few-Cycle Laser Pulse Generation and Its Applications*, pp. 179–228. Berlin: Springer (2004).

[120] N. Ishii, L. Turi, V. S. Yakovlev, T. Fuji, F. Krausz, A. Baltuska, R. Butkus, G. Veitas, V. Smilgevicius, R. Danielius and A. Piskarskas. *Multimillijoule chirped parametric amplification offew-cycle pulses*. Optics Letters, **30**(5), 567–569 (2005).

[121] S. Witte, R. Zinkstok, W. Hogervorst and K. Eikema. *Generation of few-cycle terawatt light pulses using optical parametric chirped pulse amplification.* Optics Express, **13**(13), 4903–4908 (2005).

[122] S. Witte, R. T. Zinkstok, A. L. Wolf, W. Hogervorst, W. Ubachs and K. S. E. Eikema. *A source of 2 terawatt, 2.7 cycle laser pulses based on noncollinear optical parametric chirped pulse amplification.* Optics Express, **14**(18), 8168–8177 (2006).

[123] A. Dubietis, G. Jonusauskas and A. Piskarskas. *Powerful femtosecond pulse generation by chirped and stretched pulse parametric amplification in BBO crystal.* Optics Communications, **88**(4-6), 437 – 440 (1992).

[124] O. V. Chekhlov, J. L. Collier, I. N. Ross, P. K. Bates, M. Notley, C. Hernandez-Gomez, W. Shaikh, C. N. Danson, D. Neely, P. Matousek, S. Hancock and L. Cardoso. *35 J broadband femtosecond optical parametric chirped pulse amplification system.* Optics Letters, **31**(24), 3665–3667 (2006).

[125] D. Herrmann, L. Veisz, R. Tautz, F. Tavella, K. Schmid, V. Pervak and F. Krausz. *Generation of sub-three-cycle, 16 TW light pulses by using noncollinear optical parametric chirped-pulse amplification.* Optics Letters, **34**(16), 2459–2461 (2009).

[126] G. Cerullo and S. D. Silvestri. *Ultrafast optical parametric amplifiers.* Review of Scientific Instruments, **74**(1), 1–18 (2003).

[127] T. Kobayashi and A. Shirakawa. *Tunable visible and near-infrared pulse generator in a 5 fs regime.* Applied Physics B: Lasers and Optics, **70**(7), S239–S246 (2000).

[128] T. Wang, Zs. Major, I. Ahmad, S. Trushin, F. Krausz and S. Karsch. *Ultrabroadband near-infrared pulse generation by noncollinear OPA with angular dispersion compensation.* Applied Physics B: Lasers and Optics (2009).

[129] J. Osterhoff. *Stable, ultra-relativistic electron beams by laser-wakefield acceleration.* Ph.D. thesis, LMU Munich (2009).

[130] R. Hörlein. *Investigation of the XUV Emission from the Interaction of Intense Femtosecond Laser Pulses with Solid Targets.* Ph.D. thesis, LMU Munich (2009).

[131] H. Baumhacker, A. Böswald, H. Haas, M. Fischer, W. Fölsner, G. Keller, U. Andiel, X. Dong, M. Dreher, K. Eidmann, E. Fill, M. Hegelich, M. Kaluza, S. Karsch, G. Pretzler, G. D. Tsakiris and K. J. Witte. *Advanced Titanium Sapphire Laser ATLAS MPQ-Report 272.* Technical Report, Max-Planck-Institut für Quantenoptik (2001).

[132] O. E. Martínez. *Design of high-power ultrashort pulse amplifiers by expansion and recompression.* IEEE Journal of Quantum Electronics, **23**(8), 1385–1387 (1987).

[133] Spawr-Industries. *Segmented integrating mirrors.* US-PAT. No. 4,195,913 (1971).

[134] H. Baumhacker, G. Pretzler, K. J. Witte, M. Hegelich, M. Kaluza, S. Karsch, A. Kudryashov, V. Samarkin and A. Roukossouev. *Correction of strong phase and amplitude modulations by two deformable mirrors in a multistaged Ti:sapphire laser.* Optics Letters, **27**(17), 1570–1572 (2002).

[135] E. B. Treacy. *Optical pulse compression with diffraction gratings.* IEEE Journal of Quantum Electronics, **5**(9), 454–458 (1969).

[136] P. O'Shea, M. Kimmel, X. Gu and R. Trebino. *Highly simplified device for ultrashort-pulse measurement.* Optics Letters, **26**(12), 932–934 (2001).

[137] D. J. Kane and R. Trebino. *Single-shot measurement of the intensity and phase of an arbitrary ultrashort pulse by using frequency-resolved optical gating.* Optics Letters, **18**(10), 823–825 (1993).

[138] K. Schmid. *Characterization of ultrashort laser pulses by third order autocorrelation.* Master's thesis, TU Wien (2004).

[139] G. Pretzler, A. Kasper and K. J. Witte. *Angular chirp and tilted light pulses in CPA lasers.* Applied Physics B: Lasers and Optics, **70**(1), 1–9 (2000/01/01/).

[140] F. Verluise, V. Laude, Z. Cheng, C. Spielmann and P. Tournois. *Amplitude and phase control of ultrashort pulses by use of an acousto-optic programmable dispersive filter: pulse compression and shaping.* Optics Letters, **25**(8), 575–577 (2000).

[141] H. C. Kapteyn, M. M. Murnane, A. Szoke and R. W. Falcone. *Prepulse energy suppression for high-energy ultrashort pulses using self-induced plasma shuttering.* Optics Letters, **16**(7), 490–492 (1991).

[142] G. Doumy, F. Quéré, O. Gobert, M. Perdrix, P. Martin, P. Audebert, J. C. Gauthier, J.-P. Geindre and T. Wittmann. *Complete characterization of a plasma mirror for the production of high-contrast ultraintense laser pulses.* Physical Review E, **69**(2), 026402 (2004).

[143] S. Steinke. *Entwicklung eines Doppel-Plasmaspiegels zur Erzeugung hochenergetischer Ionen mit ultra-dünnen Targets.* Master's thesis, TU Berlin (2007).

[144] S. H. Batha, R. Aragonez, F. L. Archuleta, T. N. Archuleta, J. F. Benage, J. A. Cobble, J. S. Cowan, V. E. Fatherley, K. A. Flippo, D. C. Gautier, R. P. Gonzales, S. R. Greenfield, B. M. Hegelich, T. R. Hurry, R. P. Johnson, J. L. Kline, S. A. Letzring, E. N. Loomis, F. E. Lopez, S. N. Luo, D. S. Montgomery, J. A. Oertel, D. L. Paisley, S. M. Reid, P. G. Sanchez, A. Seifter, T. Shimada and J. B. Workman. *TRIDENT high-energy-density facility experimental capabilities and diagnostics.* Review of Scientific Instruments, **79**(10), 10F305 (2008).

[145] D. L. Paisley, S.-N. Luo, S. R. Greenfield and A. C. Koskelo. *Laser-launched flyer plate and confined laser ablation for shock wave loading: Validation and applications.* Review of Scientific Instruments, **79**(2), 023902 (2008).

[146] R. C. Shah, R. P. Johnson, T. Shimada, K. A. Flippo, J. C. Fernández and B. M. Hegelich. *High-temporal contrast using low-gain optical parametric amplification.* Optics Letters, **34**(15), 2273–2275 (2009).

[147] C. Danson, P. Brummitt, R. Clarke, J. Collier, B. Fell, A. Frackiewicz, S. Hancock, S. Hawkes, C. Hernandez-Gomez, P. Holligan, M. Hutchinson, A. Kidd, W. Lester, I. Musgrave, D. Neely, D. Neville, P. Norreys, D. Pepler, C. Reason, W. Shaikh, T. Winstone, R. Wyatt and B. Wyborn. *Vulcan Petawatt—an ultra-high-intensity interaction facility.* Nuclear Fusion, **44**(12), S239–S246 (2004).

[148] C. N. Danson, P. A. Brummitt, R. J. Clarke, J. L. Collier, B. Fell, A. J. Frackiewicz, S. Hawkes, C. Hernandez-Gomez, P. Holligan, M. H. R. Hutchinson, A. Kidd, W. J. Lester, I. O. Musgrave, D. Neely, D. R. Neville, P. A. Norreys, D. A. Pepler, C. J. Reason, W. Shaikh, T. B. Winstone, R. W. W. Wyatt and B. E. Wyborn. *Vulcan petawatt: Design, operation and interactions at* 5×10^{20} *W/cm*^{2}. Laser and Particle Beams, **23**, 87–93 (2005).

[149] J. Collier, C. Hooker, S. Hawkes, C. Edwards, C. Haefner and K. Braeur. *Adaptive Optics for the Petawatt upgrade.* CCLRC Rutherford Appleton Laboratory Central Laser Facility Annual Report, p. 181 (2001/2002).

[150] J. Collier, C. Danson, C. Johnson and C. Mistry. *Uniaxial single shot autocorrelator.* Review of Scientific Instruments, **70**(3), 1599–1602 (1999).

[151] I. Musgrave, C. Hernandez-Gomez, D. Canny, R. Heathcote, R. J. Clarke, J. L. Collier and S. Bandyopadhyay. *Nanosecond contrast measurements of the Vulcan Petawatt facility.* CCLRC Rutherford Appleton Laboratory Central Laser Facility Annual Report, pp. 197–199 (2004/2005).

[152] C. Hernandez-Gomez, I. O. Musgrave and J. L. Collier. *Picosecond contrast measurements of the Vulcan Petawatt facility.* CCLRC Rutherford Appleton Laboratory Central Laser Facility Annual Report, p. 200 (2004/2005).

[153] J. Schreiber, C. Palmer, S. R. Nagel, N. Dover, C. Bellei, F. N. Beg, S. Bott, R. J. Clarke, A. E. Dangor, S. M. Hassan, D. Habs, M. Hegelich, A. Henig, P. Hilz, D. Jung, S. Kneip, S. P. D. Mangles, K. L. Lancaster, A. Rehman, C. Spindloe, J. Szerypo, M. Tatarakis, M. Yeung, M. Zepf and Z. Najmudin. *Radiation-driven acceleration and instability of expanding ultra-thin diamond-like carbon foils.* submitted (2010).

[154] D. Neely, P. Foster, A. Robinson, F. Lindau, O. Lundh, A. Persson, C.-G. Wahlström and P. McKenna. *Enhanced proton beams from ultrathin targets driven by high contrast laser pulses.* Applied Physics Letters, **89**(2), 021502 (2006).

[155] P. Antici, J. Fuchs, E. d'Humières, E. Lefebvre, M. Borghesi, E. Brambrink, C. A. Cecchetti, S. Gaillard, L. Romagnani, Y. Sentoku, T. Toncian, O. Willi, P. Audebert and H. Pépin. *Energetic protons generated by ultrahigh contrast laser pulses interacting with ultrathin targets.* Physics of Plasmas, **14**(3), 030701 (2007).

[156] T. Ceccotti, A. Lévy, H. Popescu, F. Réau, P. D'Oliveira, P. Monot, J. P. Geindre, E. Lefebvre and P. Martin. *Proton Acceleration with High-Intensity Ultrahigh-Contrast Laser Pulses.* Physical Review Letters, **99**(18), 185002 (2007).

[157] T. M. Ivkova, V. K. Liechtenstein and E. D. Olshanski. *Preparation and application of ultra-thin superstrong diamond-like carbon targets for laboratory*

and space experiments. Nuclear Instruments and Methods in Physics Research A, **362**, 77–80 (1995).

[158] V. K. Liechtenstein, T. M. Ivkova, E. D. Olshanski, I. Feigenbaum, R. DiNardo and M. Döbeli. *Preparation and evaluation of thin diamond-like carbon foils for heavy-ion tandem accelerators and time-of-flight spectrometers.* Nuclear Instruments and Methods in Physics Research A, **397**, 140–145 (1997).

[159] V. K. Liechtenstein, T. M. Ivkova, E. D. Olshanski, A. M. Baranov, R. Repnow, R. Hellborg, R. A. Weller and H. L. Wirth. *Preparation and comparative testing of advanced diamond-like carbon foils for tandem accelerators and time-of-flight spectrometers.* Nuclear Instruments and Methods in Physics Research A, **438**, 79–85 (1999).

[160] V. K. Liechtenstein, T. M. Ivkova, E. D. Olshanski, R. Repnow, J. Levin, R. Hellborg, P. Persson and T. Schenkel. *Advances in targetry with thin diamond-like carbon foils.* Nuclear Instruments and Methods in Physics Research A, **480**, 185–190 (2002).

[161] V. K. Liechtenstein, T. M. Ivkova, E. D. Olshanski, R. Golser, W. Kutschera, P. Steier, C. Vockenhuber, R. Repnow, R. von Hahn, M. Friedrich and U. Kreissig. *Recent investigations and applications of thin diamond-like carbon (DLC) foils.* Nuclear Instruments and Methods in Physics Research A, **521**, 197–202 (2004).

[162] V. K. Liechtenstein, T. M. Ivkova, E. D. Olshanski, R. Repnow, P. Steier, W. Kutschera, A. Wallner and R. von Hahn. *Preparation and investigation of ultra-thin diamond-like carbon (DLC) foils reinforced with collodion.* Nuclear Instruments and Methods in Physics Research A, **561**, 120–123 (2006).

[163] I. G. Brown. *Cathodic Arc Deposition of Films.* Annual Review of Materials Science, **28**(1), 243–269 (1998).

[164] I. I. Aksenov, S. I. Vakula, V. G. Padalka, V. E. Strelnitskii and V. M. Khoroshikh. Soviet Physics - Technical Physics, **25**, 1164–1166 (1980).

[165] I. I. Aksenov, V. G. Bren, V. G. Padalka and V. M. Khoroshikh. Soviet Physics - Technical Physics, **23**, 651–653 (1979).

[166] W. M. A. Bik and F. H. P. M. Habraken. *Elastic recoil detection.* Reports on Progress in Physics, **56**(7), 859–902 (1993).

[167] G. Dollinger, T. Faestermann and P. Maier-Komor. *High resolution depth profiling of light elements.* Nuclear Instruments and Methods in Physics Research B, **64**, 422–427 (1992).

[168] G. Dollinger, A. Bergmaier, T. Faestermann and C. M. Frey. *High resolution depth profile analysis by elastic recoil detection with heavy ions.* Fresenius' Journal of Analytical Chemistry, **353**(3), 311–315 (1995).

[169] G. Dollinger, C. M. Frey, A. Bergmaier and T. Faestermann. *Depth profile analysis with monolayer resolution using elastic recoil detection (ERD).* Europhysics Letters, **42**(1), 25–30 (1998).

[170] M. Löffler, H.-J. Scheerer and H. Vonach. *The ion optical properties of the Munich Q3D-spectrograph investigated by means of a special experimental ray tracing method.* Nuclear Instruments and Methods, **111**, 1–12 (1973).

[171] H. A. Bethe and J. Ashkin. *Experimental Nuclear Physics.* John Wiley and Sons, Inc., New York (1953).

[172] R. L. Fleischer, P. B. Price and R. M. Walker. *Ion Explosion Spike Mechanism for Formation of Charged-Particle Tracks in Solids.* Journal of Applied Physics, **36**(11), 3645–3652 (1965).

[173] S. Gaillard, J. Fuchs, N. R.-L. Galloudec and T. E. Cowan. *Study of saturation of CR39 nuclear track detectors at high ion fluence and of associated artifact patterns.* Review of Scientific Instruments, **78**(1), 013304 (2007).

[174] G. Rusch, E. Winkel, A. Noll and W. Heinrich. *The Siegen automatic measuring system for track detectors: New developments.* International Journal of Radiation Applications and Instrumentation. Part D. Nuclear Tracks and Radiation Measurements, **19**(1-4), 261 – 266 (1991).

[175] S. Kar, M. Borghesi, L. Romagnani, S. Takahashi, A. Zayats, V. Malka, S. Fritzler and A. Schiavi. *Analysis of latent tracks for MeV protons in CR-39.* Journal of Applied Physics, **101**(4), 044510 (2007).

[176] D. S. Hey, M. H. Key, A. J. Mackinnon, A. G. MacPhee, P. K. Patel, R. R. Freeman, L. D. V. Woerkom and C. M. Castaneda. *Use of GafChromic film to diagnose laser generated proton beams.* Review of Scientific Instruments, **79**(5), 053501 (2008).

[177] J. Miyahara, K. Takahashi, Y. Amemiya, N. Kamiya and Y. Satow. *A new type of X-ray area detector utilizing laser stimulated luminescence.* Nuclear Instruments and Methods in Physics Research A, **246**, 572–578 (1986).

[178] K. A. Tanaka, T. Yabuuchi, T. Sato, R. Kodama, Y. Kitagawa, T. Takahashi, T. Ikeda, Y. Honda and S. Okuda. *Calibration of imaging plate for high energy electron spectrometer.* Review of Scientific Instruments, **76**(1), 013507 (2005).

[179] B. Hidding, G. Pretzler, M. Clever, F. Brandl, F. Zamponi, A. Lübcke, T. Kämpfer, I. Uschmann, E. Förster, U. Schramm, R. Sauerbrey, E. Kroupp, L. Veisz, K. Schmid, S. Benavides and S. Karsch. *Novel method for characterizing relativistic electron beams in a harsh laser-plasma environment.* Review of Scientific Instruments, **78**(8), 083301 (2007).

[180] A. Mančić, J. Fuchs, P. Antici, S. A. Gaillard and P. Audebert. *Absolute calibration of photostimulable image plate detectors used as (0.5–20 MeV) high-energy proton detectors.* Review of Scientific Instruments, **79**(7), 073301 (2008).

[181] S. Ter-Avetisyan, M. Schnürer and P. V. Nickles. *Time resolved corpuscular diagnostics of plasmas produced with high-intensity femtosecond laser pulses.* Journal of Physics D: Applied Physics, **38**(6), 863–867 (2005).

[182] J. J. Thomson. *Bakerian Lecture: Rays of Positive Electricity.* Royal Society of London Proceedings Series A, **89**, 1–20 (1913).

[183] J. Schreiber and D. Jung. Private communications.

[184] J. Schreiber. *Ion Acceleration driven by High-Intensity Laser Pulses.* Ph.D. thesis, LMU Munich (2006).

[185] URL http://www.srim.org.

[186] P. McKenna, D. C. Carroll, R. J. Clarke, R. G. Evans, K. W. D. Ledingham, F. Lindau, O. Lundh, T. McCanny, D. Neely, A. P. L. Robinson, L. Robson, P. T. Simpson, C.-G. Wahlström and M. Zepf. *Lateral Electron Transport in High-Intensity Laser-Irradiated Foils Diagnosed by Ion Emission.* Physical Review Letters, **98**(14), 145001 (2007).

[187] J. Limpouch, J. Psikal, A. A. Andreev, K. Y. Platonov and S. Kawata. *Enhanced laser ion acceleration from mass-limited targets.* Laser and Particle Beams, **26**, 225–234 (2008).

[188] A. J. Kemp and H. Ruhl. *Multispecies ion acceleration off laser-irradiated water droplets.* Physics of Plasmas, **12**(3), 033105 (2005).

[189] J. Psikal, V. T. Tikhonchuk, J. Limpouch, A. A. Andreev and A. V. Brantov. *Ion acceleration by femtosecond laser pulses in small multispecies targets.* Physics of Plasmas, **15**(5), 053102 (2008).

[190] S. Karsch, S. Düsterer, H. Schwoerer, F. Ewald, D. Habs, M. Hegelich, G. Pretzler, A. Pukhov, K. Witte and R. Sauerbrey. *High-Intensity Laser Induced Ion Acceleration from Heavy-Water Droplets.* Physical Review Letters, **91**(1), 015001 (2003).

[191] S. Busch, M. Schnürer, M. Kalashnikov, H. Schönnagel, H. Stiel, P. V. Nickles, W. Sandner, S. Ter-Avetisyan, V. Karpov and U. Vogt. *Ion acceleration with ultrafast lasers.* Applied Physics Letters, **82**(19), 3354–3356 (2003).

[192] R. Ramis, R. Schmalz and J. Meyer-ter-Vehn. *MULTI – A computer code for one-dimensional multigroup radiation hydrodynamics.* Computer Physics Communications, **49**(3), 475 – 505 (1988).

[193] M. Geissler, J. Schreiber and J. Meyer-ter-Vehn. *Bubble acceleration of electrons with few-cycle laser pulses.* New Journal of Physics, **8**(9), 186 (2006).

[194] J. Psikal, J. Limpouch, S. Kawata and A. Andreev. *Pic simulations of femtosecond interactions with mass-limited targets.* Czechoslovak Journal of Physics, **56**, B515–B521(1) (2006).

[195] Q. L. Dong, Z.-M. Sheng, M. Y. Yu and J. Zhang. *Optimization of ion acceleration in the interaction of intense femtosecond laser pulses with ultrathin foils.* Physical Review E, **68**(2), 026408 (2003).

[196] E. d'Humières, E. Lefebvre, L. Gremillet and V. Malka. *Proton acceleration mechanisms in high-intensity laser interaction with thin foils.* Physics of Plasmas, **12**(6), 062704 (2005).

[197] T. Esirkepov, M. Yamagiwa and T. Tajima. *Laser Ion-Acceleration Scaling Laws Seen in Multiparametric Particle-in-Cell Simulations.* Physical Review Letters, **96**(10), 105001 (2006).

[198] L. Yin, B. J. Albright, B. M. Hegelich and J. C. Fernández. *GeV laser ion acceleration from ultrathin targets: The laser break-out afterburner.* Laser and Particle Beams, **24**, 291–298 (2006).

[199] L. Yin, B. J. Albright, B. M. Hegelich, K. J. Bowers, K. A. Flippo, T. J. T. Kwan and J. C. Fernández. *Monoenergetic and GeV ion acceleration from the laser breakout afterburner using ultrathin targets.* Physics of Plasmas, **14**(5), 056706 (2007).

[200] K. J. Bowers, B. J. Albright, L. Yin, B. Bergen and T. J. T. Kwan. *Ultrahigh performance three-dimensional electromagnetic relativistic kinetic plasma simulation.* Physics of Plasmas, **15**(5), 055703 (2008).

[201] A. Andreev, A. Lévy, T. Ceccotti, C. Thaury, K. Platonov, R. A. Loch and P. Martin. *Fast-Ion Energy-Flux Enhancement from Ultrathin Foils Irradiated by Intense and High-Contrast Short Laser Pulses.* Physical Review Letters, **101**(15), 155002 (2008).

[202] B. J. Albright, L. Yin, B. M. Hegelich, K. J. Bowers, C. Huang, A. Henig, J. C. Fernández, K. A. Flippo, S. A. Gaillard, T. J. T. Kwan, X. Q. Yan, T. Tajima and D. Habs. *Ultraintense laser interaction with nanoscale targets: a simple model for layer expansion and ion acceleration.* Journal of Physics: Conference Series, Proceedings of the Sixth International Conference on Inertial Fusion Sciences and Applications (IFSA) 2009, accepted (2010).

[203] X. Q. Yan, T. Tajima, M. Hegelich, L. Yin and D. Habs. *Theory of laser ion acceleration from a foil target of nanometer thickness.* Applied Physics B: Lasers and Optics (2009).

[204] F. Mako and T. Tajima. *Collective ion acceleration by a reflexing electron beam: Model and scaling.* Physics of Fluids, **27**(7), 1815–1820 (1984).

[205] D. C. Gautier, K. A. Flippo, S. A. Letzring, J. W. T. Shimada, R. P. Johnson, T. R. Hurry, S. A. Gaillard and B. M. Hegelich. *A novel backscatter focus diagnostic for the TRIDENT 200 TW laser.* Review of Scientific Instruments, **79**(10), 10F547 (2008).

[206] A. Fukumi, M. Nishiuchi, H. Daido, Z. Li, A. Sagisaka, K. Ogura, S. Orimo, M. Kado, Y. Hayashi, M. Mori, S. V. Bulanov, T. Esirkepov, K. Nemoto, Y. Oishi, T. Nayuki, T. Fujii, A. Noda and S. Nakamura. *Laser polarization dependence of proton emission from a thin foil target irradiated by a 70 fs, intense laser pulse.* Physics of Plasmas, **12**(10), 100701 (2005).

[207] M. Kado. *Observation of strongly collimated proton beam from Tantalum targets irradiated with circular polarized laser pulses.* Laser and Particle Beams, **24**(01), 117–123 (2006).

[208] A. A. Andreev, S. Steinke, T. Sokollik, M. Schnürer, S. T. Avetsiyan, K. Y. Platonov and P. V. Nickles. *Optimal ion acceleration from ultrathin foils irradiated by a profiled laser pulse of relativistic intensity.* Physics of Plasmas, **16**(1), 013103 (2009).

[209] F. Tavella, A. Marcinkevicius and F. Krausz. *90 mJ parametric chirped pulse amplification of 10 fs pulses.* Optics Express, **14**(26), 12822–12827 (2006).

[210] A. Shirakawa, I. Sakane and T. Kobayashi. *Pulse-front-matched optical parametric amplification for sub-10-fs pulse generation tunable in the visible and near infrared.* Optics Letters, **23**(16), 1292–1294 (1998).

[211] G. Cerullo, M. Nisoli, S. Stagira, S. D. Silvestri, G. Tempea, F. Krausz and K. Ferencz. *Mirror-dispersion-controlled sub-10-fs optical parametric amplifier in the visible.* Optics Letters, **24**(21), 1529–1531 (1999).

[212] P. Tzankov, J. Zheng, M. Mero, D. Polli, C. Manzoni and G. Cerullo. *300 μJ noncollinear optical parametric amplifier in the visible at 1 kHz repetition rate.* Optics Letters, **31**(24), 3629–3631 (2006).

[213] C. P. Hauri, A. Trisorio, M. Merano, G. Rey, R. B. Lopez-Martens and G. Mourou. *Generation of high-fidelity, down-chirped sub-10 fs mJ pulses through filamentation for driving relativistic laser-matter interactions at 1 kHz.* Applied Physics Letters, **89**(15), 151125 (2006).

[214] C. Iaconis and I. Walmsley. *Spectral phase interferometry for direct electric-field reconstruction of ultrashort optical pulses.* Optics Letters, **23**(10), 792–794 (1998).

[215] I. N. Ross, P. Matousek, G. H. C. New and K. Osvay. *Analysis and optimization of optical parametric chirped pulse amplification.* Journal of the Optical Society of America B Optical Physics, **19**, 2945–2956 (2002).

[216] J. A. Fülöp, Zs. Major, B. Horváth, F. Tavella, A. Baltuška and F. Krausz. *Shaping of picosecond pulses for pumping optical parametric amplification.* Applied Physics B: Lasers and Optics, **87**(1), 79–84 (2007).

[217] A. Marcinkevičius, R. Tommasini, G. D. Tsakiris, K. J. Witte, E. Gaižauskas and U. Teubner. *Frequency doubling of multi-terawatt femtosecond pulses.* Applied Physics B: Lasers and Optics, **79**(5), 547–554 (2004).

[218] P. M. Celliers, K. G. Estabrook, R. J. Wallace, J. E. Murray, L. B. D. Silva, B. J. MacGowan, B. M. V. Wonterghem and K. R. Manes. *Spatial Filter Pinhole for High-Energy Pulsed Lasers.* Applied Optics, **37**(12), 2371–2378 (1998).

[219] T. Clausnitzer, J. Limpert, K. Zöllner, H. Zellmer, H.-J. Fuchs, E.-B. Kley, A. Tünnermann, M. Jupé and D. Ristau. *Highly Efficient Transmission Gratings in Fused Silica for Chirped-Pulse Amplification Systems.* Applied Optics, **42**(34), 6934–6938 (2003).

[220] M. Nisoli, S. Stagira, S. De Silvestri, O. Svelto, S. Sartania, Z. Cheng, M. Lenzner, C. Spielmann and F. Krausz. *A novel-high energy pulse compression system: generation of multigigawatt sub-5-fs pulses.* Applied Physics B: Lasers and Optics, **65**(2), 189–196 (1997).

[221] H. Mashiko, C. M. Nakamura, C. Li, E. Moon, H. Wang, J. Tackett and Z. Chang. *Carrier-envelope phase stabilized 5.6 fs, 1.2 mJ pulses.* Applied Physics Letters, **90**(16), 161114 (2007).

[222] L. L. Ji, B. F. Shen, X. M. Zhang, F. C. Wang, Z. Y. Jin, C. Q. Xia, M. Wen, W. P. Wang, J. C. Xu and M. Y. Yu. *Generating Quasi-Single-Cycle Relativistic Laser Pulses by Laser-Foil Interaction.* Physical Review Letters, **103**(21), 215005 (2009).

[223] URL http://www.munich-photonics.de/.

[224] S. Schell and J. J. Wilkens. *Modifying proton fluence spectra to generate spread-out Bragg peaks with laser accelerated proton beams.* Physics in Medicine and Biology, **54**(19), N459–N466 (2009).

[225] T. E. Schmid, G. Dollinger, A. Hauptner, V. Hable, C. Greubel, S. Auer, A. A. Friedl, M. Molls and B. Röper. *No Evidence for a Different RBE between Pulsed and Continuous 20 MeV Protons.* Radiation Research, **172**(5), 567–574 (2009).

[226] K.-L. Kratz, K. Farouqi and B. Pfeiffer. *Nuclear physics far from stability and r-process nucleosynthesis.* Progress in Particle and Nuclear Physics, **59**(1), 147 – 155 (2007).

[227] M. Arnould, S. Goriely and K. Takahashi. *The r-process of stellar nucleosynthesis: Astrophysics and nuclear physics achievements and mysteries*. Physics Reports, **450**(4-6), 97 – 213 (2007).

[228] I. V. Panov and H.-T. Janka. *On the dynamics of proto-neutron star winds and r-process nucleosynthesis*. Astronomy & Astrophysics, **494**(3), 829–844 (2009).

[229] URL http://www.extreme-light-infrastructure.eu/.

[230] D. Habs and P. G. Thirolf. *A laser-accelerated Th beam to produce neutron-rich nuclei around the N=126 waiting point of the r-Process via the fission-fusion reaction mechanism*. Proposal for ELI Photonuclear (2010).

Publications

Peer-Reviewed Publications

2009

- **A. Henig**, S. Steinke, M. Schnürer, T. Sokollik, R. Hörlein, D. Kiefer, D. Jung, J. Schreiber, B. M. Hegelich, X. Q. Yan, T. Tajima, P. V. Nickles, W. Sandner, and D. Habs. *Radiation pressure acceleration of ion beams driven by circularly polarized laser pulses.* Physical Review Letters **103**, 245003 (2009).

- **A. Henig**, D. Kiefer, K. Markey, D. C. Gautier, K. A. Flippo, S. Letzring, R. P. Johnson, T. Shimada, L. Yin, B. J. Albright, K. J. Bowers, J. C. Fernández, S. G. Rykovanov, H.-C. Wu, M. Zepf, D. Jung, V. Kh. Liechtenstein, J. Schreiber, D. Habs, and B. M. Hegelich. *Enhanced laser-driven ion acceleration in the relativistic transparency regime.* Physical Review Letters **103**, 045002 (2009).

- **A. Henig**, D. Kiefer, M. Geissler, S. G. Rykovanov, R. Ramis, R. Hörlein, J. Osterhoff, Zs. Major, L. Veisz, S. Karsch, F. Krausz, D. Habs, and J. Schreiber. *Laser-driven shock acceleration of ion beams from spherical mass-limited targets.* Physical Review Letters **102**, 095002 (2009).

- D. Kiefer, **A. Henig**, D. Jung, D. C. Gautier, K. A. Flippo, S. A. Gaillard, S. Letzring, R. P. Johnson, R. C. Shah, T. Shimada, J. C. Fernández, V. Kh. Liechtenstein, J. Schreiber, B. M. Hegelich, and D. Habs. *First observation of quasi-monoenergetic electron bunches driven out of ultra-thin diamond-like carbon (DLC) foils.* European Physical Journal D **55**, 427 (2009).

- P. G. Thirolf, D. Habs, **A. Henig**, D. Jung, D. Kiefer, C. Lang, J. Schreiber, C. Maia, G. Schaller, R. Schützhold, and T. Tajima. *Signatures of the Unruh effect via high-power, short-pulse lasers.* European Physical Journal D **55**, 379 (2009).

- Zs. Major, S. A. Trushin, I. Ahmad, M. Siebold, C. Wandt, S. Klingebiel, T.-J. Wang, J. A. Fülöp, **A. Henig**, S. Kruber, R. Weingartner, A. Popp, J. Osterhoff, R. Hörlein, J. Hein, V. Pervak, A. Apolonski, F. Krausz, and S. Karsch. *Basic concepts and current status of the petawatt field synthesizer - a new approach to ultrahigh field generation.* Laser Review 37, 6 (2009).

2008

- S. G. Rykovanov, J. Schreiber, J. Meyer-ter-Vehn, C. Bellei, **A. Henig**, H.-C. Wu and M. Geissler. *Ion acceleration with ultra-thin foils using elliptically polarized laser pulses.* New Journal of Physics **10**, 113005 (2008).

- D. Habs, B. M. Hegelich, J. Schreiber, M. Gross, **A. Henig**, D. Kiefer and D. Jung. *Dense laser-driven electron sheets as relativistic mirrors for coherent production of brilliant X-ray and γ-ray beams.* Applied Physics B **93**, 349 (2008).

- S. Kneip, B. I. Cho, D. R. Symes, H. A. Sumeruk, G. Dyer, I. V. Churina, A. V. Belolipetski, **A. Henig**, O. Wehrhan, E. Förster, T. D. Donnelly and T. Ditmire. *K-shell spectroscopy of plasmas created by intense laser irradiation of micron-scale pyramid and sphere targets.* High Energy Density Physics **4**, 41 (2008).

2007

- J. A. Fülöp, Zs. Major, **A. Henig**, S. Kruber, R. Weingartner, T. Clausnitzer, E.-B. Kley, A. Tünnermann, V. Pervak, A. Apolonski, J. Osterhoff, R. Hörlein, F. Krausz and S. Karsch. *Short-pulse optical parametric chirped-pulse amplification for the generation of high-power few-cycle pulses.* New Journal of Physics **9**, 438 (2007).

- D. Symes, M. Hohenberger, **A. Henig** and T. Ditmire. *Anisotropic explosions of hydrogen clusters under intense femtosecond laser irradiation.* Physical Review Letters **98**, 123401 (2007).

Accepted Manuscripts

- S. Steinke, **A. Henig**, M. Schnürer, T. Sokollik, P. V. Nickles, D. Jung, D. Kiefer, J. Schreiber, T. Tajima, X. Q. Yan, J. Meyer-ter-Vehn, M. Hegelich, W. Sandner, and D. Habs. *Efficient ion acceleration by collective laser-driven electron dynamics with ultra-thin foil targets.* Laser and Particle Beams, accepted (2010).

- B. J. Albright, L. Yin, B. M. Hegelich, K. J. Bowers, C. Huang, **A. Henig**, J. C. Fernández, K. A. Flippo, S. A. Gaillard, T. J. T. Kwan, X. Q. Yan, T. Tajima, and D. Habs. *Ultraintense laser interaction with nanoscale targets: a simple model for layer expansion and ion acceleration.* Journal of Physics: Conference Series, Proceedings of the Sixth International Conference on Inertial Fusion Sciences and Applications (IFSA) 2009, accepted (2010).

Submitted Manuscripts

- J. Schreiber, C. Palmer, S. R. Nagel, N. Dover, C. Bellei, F. N. Beg, S. Bott, R. J. Clarke, A. E. Dangor, S. M. Hassan, D. Habs, B. M. Hegelich, **A. Henig**, P. Hilz, D. Jung, S. Kneip, S. P. D. Mangles, K. L. Lancaster, A. Rehman, C. Spindloe, J. Szerypo, M. Tatarakis, M. Yeung, M. Zepf, and Z. Najmudin. *Radiation-driven acceleration and instability of expanding ultra-thin diamond-like carbon foils.* Submitted (2010).

- C. Bellei, S. Nagel, S. Kar, **A. Henig**, S. Kneip, C. Palmer, A. Saevert, L. Willingale, D. Carroll, B. Dromey, J. Green, K. Markey, P. Simpson, R. J. Clarke, D. Neely, M. Kaluza, S. P. D. Mangles, P. McKenna, P. A. Norreys, J. Schreiber, M. Zepf, K. Krushelnick, and Z. Najmudin. *Characterisation of fast electron recirculation and filamentation from rear side optical emission in high intensity laser-solid interactions.* Submitted (2010).

Papers in Preparation

- R. Hörlein, **A. Henig**, S. G. Rykovanov, S. Steinke, M. Schnürer, T. Sokollik, D. Kiefer, D. Jung, X. Q. Yan, T. Tajima, B M. Hegelich, P. V. Nickles, J. Schreiber, M. Zepf, G. D. Tsakiris, W. Sandner, and D. Habs. *Dynamics of nanometer-scale foil targets irradiated with relativistically intense laser pulses.* In preparation (2010).

- D. Jung, B M. Hegelich, **A. Henig**, D. Kiefer, R. Hörlein, D. C. Gautier, X. Q. Yan, L. Yin, B. J. Albright, R. Shah, J. C. Fernández, D. Habs, and T. Tajima. *Monoenergetic ion beam generation from nano-targets with circularly polarized laser light.* In preparation (2010).

- B. M. Hegelich, L. Yin, B. J. Albright, K. J. Bowers, K. A. Flippo, D. C. Gautier, **A. Henig**, R. Hörlein, R. P. Johnson, D. Jung, D. Kiefer, S. Letzring, S. Palaniyappan, R. Shah, T. Shimada, T. Tajima, X. Q. Yan, D. Habs, and J. C. Fernández. *Towards GeV laser-driven ions: first demonstration of breakout afterburner acceleration.* In preparation (2010).

- D. Kiefer, **A. Henig**, D. Jung, R. Hörlein, P. Hilz, S. Steinke, M. Schnürer, T. Sokollik, X. Q. Yan, T. Tajima, B M. Hegelich, P. V. Nickles, J. Schreiber, W. Sandner, and D. Habs. *Radiation pressure-driven electron blowout from ultrathin foils.* In preparation (2010).

Acknowledgements

With the finish line of my PhD work in sight, I would like to take the chance to thank my collaborators, colleagues and friends for their outstanding contributions and extraordinary support over the last years, helping me to bring this thesis to fruition.

First of all, I would like to thank my supervisor Prof. Dietrich Habs for giving me the opportunity be part of his group and carry out research on the exciting field of high intensity laser-driven ion acceleration. His persistent enthusiasm and visionary thoughts have been a great inspiration from start to finish. Without any doubt, he managed to provide a perfect environment for our team, always being informed about what is happening in the lab and supporting my work in every possible way.

I am grateful to Prof. Toshiki Tajima for agreeing to be the second referee of my PhD thesis and for sharing his wisdom as the founder of laser-driven particle acceleration with a young, enquiring student.

I owe gratitude to Prof. Ferenc Krausz for giving me the opportunity to join his team at MPQ, work on the forefront of ultrashort pulse high intensity laser development and revive the experimental ion acceleration program together with Jörg Schreiber.

I am greatly indebted to Jörg Schreiber for being the mentor and companion whose outstanding expertise guided me through the intricacies of my research work. At the same time, he left a lot of freedom to me to develop own ideas and projects and was not shy of challenging them in numerous discussions.

Daniel Kiefer and Daniel Jung have not only been excellent collaborators spending countless hours of unflagging effort in the lab, but also great fellows sharing many of the best moments with me.

I would like to thank the ATLAS laser team, especially Prof. Stefan Karsch, Zsuzsanna Major, Jens Osterhoff and Rainer Hörlein for their input in the construction and maintenance of ATLAS and many useful advices. Thanks also to the whole experimental High Field Science group at MPQ, in particular George Tsakiris, Las-

zlo Veisz, Antonia Popp, Raphael Weingärtner, Matthias Fuchs, Patrick Heißler, Klaus Allinger, Jianhui Bin and Peter Hilz for the fun time and their assistance.

I am grateful to Jerzy Szerypo, Hans-Jörg Maier, Dagmar Frischke, Walter Fölsner and Olivia Padovan-Merhar for their support in target preparation. Thanks to the technical staff at MPQ and LMU, especially Alois Böswald, Manfred Fischer, Harald Haas, Hans-Peter Schönauer, Johannes Wulz and the mechanical workshops at MPQ and LMU for their help in the preparation of experimental setups.

I hold Xueqing Yan, Lin Yin, Brian Albright, Michael Geissler, Sergey Rykovanov and Prof. Jürgen Meyer-ter-Vehn in high regard for their input in terms of PIC simulations and analytical theory as well as many interesting and helpful discussions.

Thanks to Zulfikar Najmudin, Stuart Mangles, Prof. Matt Zepf and their groups from Imperial College London and Queens University Belfast for the chance to participate in several experiments at the VULCAN laser at Rutherford Appleton Laboratory. Special thanks to Stefan Kneip, Claudio Bellei, Sabrina Nagel and Charlotte Palmer for good times in the lab and on weekends in London.

I owe gratitude to Prof. Manuel Hegelich and Juan Fernández for the opportunity to carry out the two leadoff experimental campaigns on ion acceleration from ultrathin DLC foil targets at the TRIDENT laser facility in Los Alamos. Thanks to the TRIDENT crew, especially Kirk Flippo, Cort Gautier, Sam Letzring, Rahul Shah, Randy Johnson and Tom Shimada for providing such a highly reliable laser system and for their outstanding assistance during the measurements. Thanks also to Keith Markey from Queens University in Belfast for sharing good times and bad with Daniel Kiefer and me during the first LANL run, and for an epic road trip.

I am grateful to Prof. Wolfgang Sandner, Peter Nickles, Matthias Schnürer, Thomas Sokollik and Sven Steinke for the extraordinary collaboration and the chance to conduct a series of very successful experiments at Max Born Institute in Berlin. Thanks to Lutz Ehrentraut for his effort to keep the laser at peak performance and the rest of the MBI staff for their continued support.

I acknowledge the International Max-Planck Research School on Advanced Photon Science for financial and intellectual sponsorship throughout my PhD studies.

I want to express the highest gratitude to my family that supported me throughout my whole life in every imaginable way, especially my parents Monika and Walter to whom I dedicate this thesis. I owe you more than I could possibly put into words.

Last but not least, my very special tanks goes to my wife Marion who was always there for me, no matter if I was spending 24h shifts in the lab at MPQ or five months a year doing research somewhere abroad.